

FINAL REPORT

Metal Perhydrides for Hydrogen Storage

Award Number: DE-FC36-05GO15003

Project Period: April 1, 2005 to August 31, 2011

Jiann-Yang Hwang, Shangzhao Shi, Steve Hackney, Douglas Swenson, Yunhang Hu

Department of Materials Science and Engineering

Michigan Technological University

1400 Townsend Drive

Houghton, MI 49931

(906)-487-2600 (Tel); (906)-487-2934 (Fax); Email: jhwang@mtu.edu

Submitted to:

US Department of Energy

DOE Technology Development Manager: Grace Ordaz

(202)-586-8350 (Tel); (202)-586-9811 (Fax); grace.ordaz@ee.doe.gov

DOE Project Officer: Katie Randolph

(303)-275-4901 (Tel), katie.randolph@go.doe.gov

Date of Report: July 26, 2011

ABSTRACT

Hydrogen is a promising energy source for the future economy due to its environmental friendliness. One of the important obstacles for the utilization of hydrogen as a fuel source for applications such as fuel cells is the storage of hydrogen. In the infrastructure of the expected hydrogen economy, hydrogen storage is one of the key enabling technologies. Although hydrogen possesses the highest gravimetric energy content (142 KJ/g) of all fuels, its volumetric energy density (8 MJ/L) is very low. It is desired to increase the volumetric energy density of hydrogen in a system to satisfy various applications.

Research on hydrogen storage has been pursued for many years. Various storage technologies, including liquefaction, compression, metal hydride, chemical hydride, and adsorption, have been examined. Liquefaction and high pressure compression are not desired due to concerns related to complicated devices, high energy cost and safety. Metal hydrides and chemical hydrides have high gravimetric and volumetric energy densities but encounter issues because high temperature is required for the release of hydrogen, due to the strong bonding of hydrogen in the compounds. Reversibility of hydrogen loading and unloading is another concern. Adsorption of hydrogen on high surface area sorbents such as activated carbon and organic metal frameworks does not have the reversibility problem. But on the other hand, the weak force (primarily the van der Waals force) between hydrogen and the sorbent yields a very small amount of adsorption capacity at ambient temperature. Significant storage capacity can only be achieved at low temperatures such as 77K. The use of liquid nitrogen in a hydrogen storage system is not practical.

Perhydrides are proposed as novel hydrogen storage materials that may overcome barriers slowing advances to a hydrogen fuel economy. In conventional hydrides, e.g. metal hydrides, the number of hydrogen atoms equals the total valence of the metal ions. One LiH molecule contains one hydrogen atom because the valence of a Li ion is +1. One MgH₂ molecule contains two hydrogen atoms because the valence of a Mg ion is +2. In metal perhydrides, a molecule could contain more hydrogen atoms than expected based on the metal valance, i.e. LiH_{1+n} and MgH_{2+n} (n is equal to or greater than 1). When n is sufficiently high, there will be plenty of hydrogen storage capacity to meet future requirements. The existence of hydrogen clusters, H_n⁺ (n = 5, 7, 9, 11, 13, 15) and transition metal ion-hydrogen clusters, M⁺(H₂)_n (n = 1-6), such as Sc(H₂)ⁿ⁺, Co(H₂)ⁿ⁺, etc., have assisted the development of this concept.

Clusters are not stable species. However, their existence stimulates our approach on using electric charges to enhance the hydrogen adsorption in a hydrogen storage system in this study. The experimental and modeling work to verify it are reported here.

Experimental work included the generation of cold hydrogen plasma through a microwave approach, synthesis of sorbent materials, design and construction of lab devices, and the determination of hydrogen adsorption capacities on various sorbent materials under various electric field potentials and various temperatures.

The results consistently show that electric potential enhances the adsorption of hydrogen on sorbents. NiO, MgO, activated carbon, MOF, and MOF and platinum coated activated carbon are some of the materials studied. Enhancements up to a few hundred percents have been found. In general, the enhancement increases with the electrical potential, the pressure applied, and the temperature lowered.

Theoretical modeling of the hydrogen adsorption on the sorbents under the electric potential has been investigated with the density functional theory (DFT) approach. It was found that the interaction energy between hydrogen and sorbent is increased remarkably when an electric field is applied. This increase of binding energy offers a potential solution for DOE when looking for a compromise between chemisorption and physisorption for hydrogen storage. Bonding of chemisorption is too strong and requires high temperature for the release of hydrogen. Bonding for the physisorption is too weak for sufficient uptake of hydrogen. Electric field potentials can enhance the physisorption and can be adjusted to yield reversibility required in a system at room temperature.

Table of Contents

ABSTRACT	i
Section 1. INTRODUCTION AND CONCEPT DEVELOPMENT	1
1.1 Background	1
1.2 Perhydride Concept	1
1.3 Conceptual Fundamentals	2
1.3.1 Bond-forming versatility of hydrogen atoms	2
1.3.2 Proposed new chemical bonds formed by hydrogen atoms	2
1.3.2.1 Electron-sharing poly-hydrogen molecular orbit	3
1.3.2.2 Hole-sharing poly-hydrogen molecular orbit	3
1.4 Observed Hydrogen Clusters	4
1.4.1 Hydrogen ion clusters.....	4
1.4.2 Metal hydrogen clusters	5
1.4.3 Non-metallic hydrogen clusters.....	6
1.5 Potential Molecular Composition of Perhydrides	7
1.6 Objectives.....	8
1.7 Approaches.....	8
1.8 Section 1 References	9
Section 2. DENSITY FUNCTIONAL COMPUTATION OF HYDROGEN CLUSTERS ...	11
2.1 Introduction	11
2.2 Computational Method.....	11
2.3 Results and Discussion.....	12
2.3.1 Hydrogen clusters on alkaline earth metal ions.....	12
2.3.2 Negative charged ion clusters.....	16
2.3.3 Clusters with metal oxides.....	18
2.3.4 Clusters with gas molecules	22
2.4 Conclusion.....	25
2.2 Section 2 References	25
Section 3. HYDROGEN PLASMA GENERATED WITH MICROWAVE	27
3.1 Background	27
3.2 Experimental	28
3.3 Results and Discussion.....	29
3.4 Conclusion.....	34
3.2 Section 3 References	34
Section 4. SALT IMPREGNATED ACTIVATED CARBON FOR HYDROGEN STORAGE	36
4.1 Introduction	36
4.2 Experimental	37
4.2.1 Preparation of samples	37
4.2.2 Characterization.....	37
4.2.3 Hydrogen adsorption measurements	38
4.2.4 Computational method	39
4.3 Results and Discussion.....	40
4.3.1 Raw activated carbon	40
4.3.2 Salt impregnated carbon.....	41

4.3.3 Computational results	44
4.3.3.1 Cluster optimization	44
4.3.3.2 Hydrogen adsorption on first group halides	46
4.3.4 Comparison of experimental and computational results	49
4.4 Section 4 References	49
Section 5. HYDROGEN ADSORPTION ON METAL ELECTRODES	51
5.1 Introduction	51
5.2 Experimental	51
5.2.1 High electric field testing device	51
5.2.2 Electrode formation	54
5.3 Results and Discussion	55
5.3.1 Nitrogen gas adsorption	55
5.3.2 Hydrogen gas adsorption	60
Section 6. ELECTRIC FIELD ASSISTED HYDROGEN ADSORPTION ON POROUS METAL OXIDES	65
6.1 Introduction	65
6.2 Experimental	66
6.2.1 Synthesis of porous oxides	66
6.2.2 Platinum deposition	66
6.2.3 Characterization of the synthesized oxides	66
6.2.4 Hydrogen storage measurements	67
6.2.5 Computational method	68
6.3 Results and Discussion	68
6.3.1 Porous nickel oxides	68
6.3.1.1 Characterization of as synthesized oxides	68
6.3.1.2 Hydrogen storage of nickel oxides	72
6.3.1.2.1 Hydrogen storage of electric field assisted porous nickel oxide	72
6.3.1.2.2 Hydrogen storage of electric field assisted spillover on nickel oxide	73
6.3.2 Porous magnesium oxides	80
6.3.2.1 Characterization of as synthesized oxides	80
6.3.2.2 Hydrogen storage of electric field assisted porous magnesium oxide	84
6.4 Summary	90
6.5 Section 6 References	91
Section 7. CHARGE ENHANCED HYDROGEN ADSORPTION ON ACTIVATED CARBON	93
7.1 Introduction	93
7.2 Adsorption Enhancement using Piezoelectric Materials	93
7.2.1 Background	93
7.2.2 Experimental	93
7.2.2.1 Materials	93
7.2.2.2 Hydrogen adsorption	94
7.2.3 Results and Discussion	94
7.3 Activated Carbon and Platinum Coated Activated Carbon under External Electric Potential	97
7.3.1 Background	97
7.3.2 Experimental	98

7.3.2.1 Materials	98
7.3.2.2 Hydrogen adsorption	98
7.3.3 Results and Discussion	99
7.3.3.1 Hydrogen adsorption on Activated Carbon with applied electric potential	99
7.3.3.2 Hydrogen adsorption on Pt Coated AC with applied electric potential	101
7.4 Hydrogen Desorption	104
7.5 Conclusions	105
7.6 Section 7 References	106
Section 8. PERCOLATIVE MOF-CARBON COMPOSITES FOR HYDROGEN STORAGE	108
8.1 Introduction	108
8.2 Experimental	109
8.2.1 Preparation of MOF-carbon composites	109
8.2.2 Characterization.....	109
8.2.3 Hydrogen storage measurement	110
8.2.4 Computational modeling	111
8.3 Results and Discussion.....	111
8.3.1 Experimental results	111
8.3.2 Computational Results.....	117
8.4 Conclusions	118
8.5 Section 8 References	118
Section 9. OVERALL CONCLUSIONS AND ACCOMPLISHMENTS.....	121
9.1 Overall Conclusions	121
9.2 Patents	121
9.3 Publications	121

List of Tables

Table 1.1. Ionic Radius of Hydrogen and Atomic Radii of Some Metal Elements in Different Periodic Positions	3
Table 3.1. Observed plasmas of using different concentrators	30
Table 4.1. BET analysis of raw carbon and salt impregnated carbon.....	40
Table 4.2. Concentration of the impregnated salts	42
Table 4.3. Adjusted surface area based on the salt concentration	42
Table 4.4. Optimized cluster parameters	45
Table 4.5. The optimized hydrogen bond length, Mulliken charge, adsorption energy, and dipole moment of hydrogen adsorption on cluster surface	48
Table 6.1. Surface properties of calcined nickel oxides	72
Table 8.1. DC conductivity and capacitance of IRMOF-8 and MOFAC composites	113
Table 8.2. BET surface area of IRMOF-8, carbon, and MOFAC	115
Table 8.3. Optimized geometry and binding energy of hydrogen adsorption on MOF Zn ₄ O unit and carbon under the external electric field	118

List of Figures

Figure 1.1. Intra-molecular hydrogen bond in phenethyl alcohol	3
Figure 1.2. The structure of a metal perhydride molecule	7
Figure 1.3. The structure of a non-metal perhydride molecule.....	8
Figure 1.4. The structure of a perhydride molecule containing both positive and negative hydrogen clusters.....	8
Figure 2.1. Simulated structures of hydrogen-alkaline metal ion clusters $M^{++}(H_2)_n$	13
Figure 2.2. Calculated distance between M^{++} and H_2 as a function of number of H_2	14
Figure 2.3. Calculated bond length of H-H in the clusters	15
Figure 2.4. Stabilization energies of $M^{++}nH_2$ clusters	16
Figure 2.5. Optimized structure of $[O(H_2)_8]^{2-}$	17
Figure 2.6. Optimized structure of $[Cl(H_2)_8]^{2-}$	18
Figure 2.7. Geometry of $VO(H_2)_8$ cluster calculated from DFT	19
Figure 2.8. Geometry of $CrO(H_2)_8$ cluster calculated from DFT	20
Figure 2.9. Geometry of $MnO(H_2)_8$ cluster calculated from DFT	20
Figure 2.10. Geometry of $FeO(H_2)_8$ cluster calculated from DFT	21
Figure 2.11. Geometry of $CoO(H_2)_8$ cluster calculated from DFT	21
Figure 2.12. Geometry of $NiO(H_2)_8$ cluster calculated from DFT	22
Figure 2.13. Geometry of $CO(H_2)_8$ cluster calculated from DFT	23
Figure 2.14. Geometry of $CO_2(H_2)_8$ cluster calculated from DFT	24
Figure 2.15. Geometry of $HCl(H_2)_8$ cluster calculated from DFT	25
Figure 3.1. Schematic picture of experimental system	28
Figure 3.2. Selected field concentrators	29
Figure 3.3. Typical plasma images	30
Figure 3.4. Gas temperature profiles at $Ar/N_2=1$, concentrator: (a) Cu powder, (b) Fe powder ...	31
Figure 3.5. Gas temperature at 2kW, H_2 300 ml/min, concentrator: Cu powder.....	32
Figure 3.6. Plasma images and gas temperature at H_2 300 ml/min, concentrator: Cu powder, 2kW to initiate and 1.5 kW to maintain	33
Figure 3.7. Failed concentrators.....	33
Figure 4.1. View of the PCT-Pro 2000 instrument.....	38
Figure 4.2. Operating screen of the PCT-Pro 2000 software.....	39
Figure 4.3. Point charge array for cluster simulation.....	40
Figure 4.4. Hydrogen adsorption of activated carbon at 298 K and 77K	41
Figure 4.5. Hydrogen adsorption of salt impregnated carbon at 298 K.....	43
Figure 4.6. Hydrogen capacity per surface area of salt impregnated carbon.....	44
Figure 4.7. Optimized clusters in point charge	45
Figure 4.8. Optimized geometry of H_2 adsorbed on LiCl Li site (a) and Cl site (b), NaCl Na site (c) and Cl site (d), KCl K site (e) and Cl (f) site, KBr K site (g) and Br site (h)	47
Figure 5.1. High electrical field testing system	52
Figure 5.2. Electric circuit of the high electrical field system	53
Figure 5.3. Adsorption mechanism of the electrodes	54

Figure 5.4. Charging signals at resistor 1 at 50 psi nitrogen pressure, applied voltage 200 V to 2000 V	55
Figure 5.5. Leakage signals at charging at 50 psi nitrogen pressure, applied voltage 200 V to 2000 V	56
Figure 5.6. Discharge signals at 50 psi nitrogen pressure, applied voltage 200 V to 2000 V	57
Figure 5.7. Charging signals at 150 psi nitrogen pressure, applied voltage 200 V to 2000 V	58
Figure 5.8. Leakage signals 150 psi nitrogen pressure, applied voltage 200 V to 2000 V	59
Figure 5.9. Discharge signals 150 psi nitrogen pressure, applied voltage 200 V to 2000 V	59
Figure 5.10. Charging signals at 40 psi hydrogen pressure, applied voltage 200 V to 2000 V	60
Figure 5.11. Leakage signals at 40 psi hydrogen pressure, applied voltage 200 V to 2000 V	61
Figure 5.12. Discharge signals at 40 psi hydrogen pressure, applied voltage 200 V to 2000 V	61
Figure 5.13. Charging signals at hydrogen pressure (a) 200 psi, (b) 400 psi, (c) 600 psi, (d) 1000 psi, applied voltage 200 V to 2000 V	62
Figure 5.14. Discharge signals at hydrogen pressure (a) 200 psi, (b) 400 psi, (c) 600 psi, (d) 1000 psi, applied voltage 200 V to 2000 V	63
Figure 5.15. Discharge signals at applied voltage (a) 200 V, (b) 1000 V, (c) 1500 V, (d) 2000 psi, hydrogen pressure from 200 psi to 1000 psi.....	64
Figure 6.1. Schematic of sample holder arrangement.....	67
Figure 6.2. XRD pattern of as-synthesized nickel oxide	69
Figure 6.3. FE-SEM images of as-synthesized nickel oxide	69
Figure 6.4. DTA curve of as-synthesized nickel oxide.....	70
Figure 6.5. Adsorption isotherms of the mesoporous nickel oxides calcined at 300°C and 360°C for different time	71
Figure 6.6. FE-SEM images of NiO calcined at 300°C for 3 hrs	72
Figure 6.7. Hydrogen adsorption isotherms at 298 K for NiO samples	73
Figure 6.8. Nitrogen adsorption/desorption isotherms of Pt deposited porous NiO, insert: BJH pore size distribution obtained by desorption isotherms	74
Figure 6.9. FE-SEM images of platinum deposited porous nickel oxide (a)(b), and EDS spectrum (c).....	75
Figure 6.10. Hydrogen storage of Pt deposited porous NiO and enhancement from the PMN-PT76	
Figure 6.11. Optimized Ni ₅ O ₅ clusters in 13x13x13 point charges.....	77
Figure 6.12. Optimized geometry of hydrogen adsorbed on nickel site under the influence of electric field.....	77
Figure 6.13. DOSs of orbital of hydrogen molecules which adsorbed on nickel site of the nickel oxide under the applied electric field	78
Figure 6.14. Optimized geometry of hydrogen adsorbed on oxygen site under the influence of electric field.....	79
Figure 6.15. DOSs of orbital of hydrogen molecules which adsorbed on oxygen site of the nickel oxide under the applied electric field	79
Figure 6.16. XRD pattern of as-synthesized hydromagnesite	80
Figure 6.17. DTA curve of as-synthesized hydromagnesite.....	81
Figure 6.18. XRD pattern of calcined magnesium oxide.....	82
Figure 6.19. FE-SEM images of MgO calcined at 400°C for 3 hours.....	83

Figure 6.20. Nitrogen adsorption/desorption isotherms of the MgO product calcined at 400°C for 3 hours, insert: BJH pore size distribution obtained from desorption isotherms	84
Figure 6.21. Hydrogen adsorption at 298 K for the porous MgO sample and MgO+PMN-PT sample.....	85
Figure 6.22. Optimized Mg ₅ O ₅ clusters in 13x13x13 point charges	86
Figure 6.23. Optimized geometry of hydrogen adsorbed on magnesium site under the influence of electric field.....	86
Figure 6.24. DOSs of orbital of hydrogen molecules which adsorbed on magnesium site of the magnesium oxide under the applied electric field.....	87
Figure 6.25. Schematic of the shape of the electron cloud under external electric field	88
Figure 6.26. Optimized geometry of hydrogen adsorbed on oxygen site under the influence of electric field.....	89
Figure 6.27. DOSs of orbital of hydrogen molecules which adsorbed on oxygen site of the magnesium oxide under the applied electric field.....	90
Figure 7.1. PMN-PT effect on H ₂ adsorption of NAC and HAC at 293K	95
Figure 7.2. H ₂ adsorption increased amount of NAC and HAC at 293K	96
Figure 7.3. PMN-PT effect on H ₂ adsorption of NAC and HAC at 77K	97
Figure 7.4. Cross-section of Sample Holder.....	99
Figure 7.5. Hydrogen adsorption on activated carbon under various pressures and voltages	100
Figure 7.6. Adsorption enhancement of activated carbon at various voltages	101
Figure 7.7. H adsorption on Pt/NAC under various pressures and voltages.....	102
Figure 7.8. Adsorption enhancement of Pt/NAC at various voltages.....	103
Figure 7.9. Hydrogen adsorption normalized by BET surface area	104
Figure 7.10. Hydrogen desorption of Pt/NAC under various pressures and voltages	105
Figure 8.1. Schematic of holder used for measurement of dielectric constant.....	110
Figure 8.2. Computational modeling of hydrogen adsorption on [Zn ₄ O] ⁶⁺ cluster and graphite surface	111
Figure 8.3. XRD of pure IRMOF-8 and carbon-IRMOF-8 composites	112
Figure 8.4. TGA curve of pure IRMOF-8 and carbon-IRMOF-8 composites.....	113
Figure 8.5. Dielectric constant of the MOFAC composites at room temperature as a function of frequency	113
Figure 8.6. FE-SEM images of IRMOF-8 and activated carbon composites	114
Figure 8.7. Hydrogen storage analysis of IRMOF-8 and MOFAC at 298K with and without the PMN-PT	116
Figure 8.8. Schematic of charge distribution in pure IRMOF-8 and MOFAC.....	117

1. INTRODUCTION AND CONCEPT DEVELOPMENT

1.1 Background

To reduce the world's dependence on fossil fuels and to alleviate global warming threats, hydrogen is viewed as the most promising energy source for the future economy. In the infrastructure of the expected hydrogen economy, hydrogen storage is one of the key enabling technologies. It is essential to develop practical and viable hydrogen storage systems before this new kind of energy can be commercially delivered and utilized. Transportation applications are an important case. A sufficient amount of hydrogen must be stored on board so that the hydrogen-fueled vehicles can run a distance of not less than 300 miles before refueling, comparable to a vehicle powered by fossil fuel. According to the technical target set by the Department of Energy, the hydrogen stored in an on-board hydrogen storage system should be no less than 6 % of the system weight by 2010 and no less than 9 % of the system weight by 2015. The corresponding cost should be no more than \$4/kWh and \$2/kWh, respectively.

Existing hydrogen storage technologies are insufficient to meet the DOE targets. Performance and failure data for safe operation of high-pressure tanks still needs to be obtained. Cryogenic liquid cylinders have problems with low liquefaction efficiency and hydrogen boil-off. Chemical hydrides have the capability to store hydrogen under normal pressure and temperature conditions, but the reactions for hydrogen liberation are irreversible, which causes problems for regeneration of the hydrides. Metal hydrides, on the other hand, can incorporate and liberate hydrogen reversibly, but suffer from low gravimetric energy densities. Carbon nanotubes were expected to be the most promising candidate, since surprisingly high storage capabilities had been reported. However, the excitement on this prospect later cooled due to the highly scattered experimental data. Furthermore, all of these approaches incur an unacceptable cost.

To meet DOE targets for hydrogen storage capacity from existing technologies almost an order of magnitude level of improvements are required. These improvements are difficult to accomplish with conventional theory. Therefore, new concepts in hydrogen storage technology have to be investigated.

In 2003, Michigan Technological University proposed to the Department of Energy to study perhydrides in response to DOE's "Grand Challenge" on hydrogen storage materials. This proposal was selected and the project was initiated in 2005 (DE-FG36-05GO15003). This final report documents the results of this study.

1.2 Perhydride Concept

Perhydride is a novel material proposed to meet the DOE hydrogen storage requirements. In conventional hydrides, e.g. metal hydrides, the number of hydrogen atoms equals the total valence of the metal ions. One LiH molecule contains one hydrogen atom because the valence of a Li ion is +1. One MgH₂ molecule contains two hydrogen atoms because the valence of a Mg ion is +2. In metal perhydrides, a molecule could contain more hydrogen atoms than expected based on the metal valence, i.e. LiH_{1+n} and MgH_{2+n} (n is equal to or greater than 1). When n is sufficiently high, there will be plenty of hydrogen storage capacity to meet future requirements.

1.3 Conceptual Fundamentals

1.3.1 Bond-forming versatility of hydrogen atoms

Hydrogen is the lightest and most abundant element. Its atom is unique, comprised of just one electron distributed around a proton nucleus. There is numerous evidence that demonstrate the versatility of hydrogen atoms to form chemical bonds [1,2,3,4]. A hydrogen atom has only one electron in its 1S orbit. The atom can either lose this electron to form a positive ion (e.g. in HCl), or gain an electron to form a saturated electronic structure (e.g. in NaH). It can also contribute its only electron to form a covalent bond with another atom (in H₂ and CH₄, e.g.). In these cases, hydrogen atoms behave as metallic, semi-metallic and non-metallic elements, respectively. In addition, it is important to note that a pair of electrons is shared by a hydrogen atom in each of these cases. Conventional hydrides basically follow this principle.

There is another distinction that sets hydrogen apart from other elements. Hydrogen has the capability to form hydrogen bonds. Different from normal chemical bonds, hydrogen bonds are formed between atoms that have already reached their valent balance. In the example of water, hydrogen forms an inter-molecular hydrogen bond with the oxygen of a neighboring water molecule and shares a total of four electrons. In another example, hydrogen in phenethyl alcohol forms an intra-molecular hydrogen bond with the pi-bond of the benzene ring of the same molecule (Figure 1.1). In this case, hydrogen shares eight electrons. The formation of hydrogen bonds is attributed to the poor shielding of protons in bonded hydrogen atoms.

Further evidence that demonstrates the bonding versatility of hydrogen atoms is the formation of hydrogen bridge bonds. Contrary to normal chemical bonds, a hydrogen bridge bond allows more than two atoms to share one electron pair (electron deficient or hole sharing). Hydrogen bridge bonds are prevailing in borane molecules.

1.3.2 Proposed new chemical bonds formed by hydrogen atoms

MTU researchers believe that the bond-forming capability of hydrogen atoms could be far beyond our established hydrogen chemistry. Since hydrogen can form additional bonds in a chemically saturated molecule and one electron pair can be shared by more than two atoms, it can be reasonably assumed that a number of hydrogen atoms and/or molecules could form delocalized bonds if an attractive charge or an equivalent field exists.

The researchers suppose that the bonding characteristics of perhydrides may bear a similarity to the bonds in metals. A comparison was made with the ionic radius of hydrogen to the atomic radii of some typical metal elements (as listed in Table 1-1). It is worthwhile to note that the ionic radius of hydrogen is similar to the atomic radii of these metal elements. This similarity indicates that the to-center distance of the 2s orbit in a hydrogen atom is similar to the to-center distances of the outmost orbits in these metal atoms.

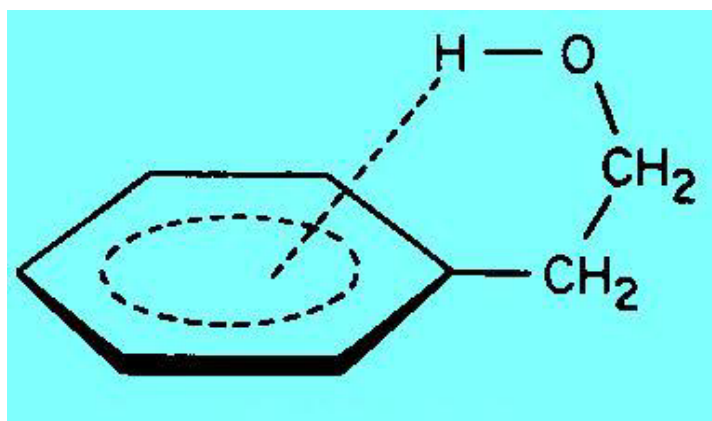


Figure 1.1. Intra-molecular hydrogen bond in phenethyl alcohol

It is well known that in each of these metallic elements, the outmost atomic orbits overlap and a metallic bond is formed by electrons traveling in this overlapping atomic orbit (metallic molecular orbit). An assumption can be made that the 2s orbits of hydrogen atoms in a cluster may also be able to overlap in a similar manner to form metal-like molecular orbits. Electrons in the individual hydrogen atoms could fill into the orbits to form bonds and/or anti-bonds. The stability of the hydrogen cluster would depend on the number of bonds and anti-bonds formed.

Table 1.1. Ionic Radius of Hydrogen and Atomic Radii of Some Metal Elements in Different Periodic Positions [4]

Element	H	Li	Mg	Ti
Radius (pm)	154(H ⁻)	152	160	144.8

Based on these considerations, two kinds of poly-hydrogen molecular orbits are proposed as listed below:

1.3.2.1 Electron-sharing poly-hydrogen molecular orbit

If there is a negatively charged hydrogen ion, H⁻, or molecule, H₂⁻, poorly shielded protons in other hydrogen atoms and/or molecules may have a tendency to share this negative charge, i.e. electron. The 2s orbits of the involved hydrogen atoms may overlap each other and form a poly-hydrogen bridge bond, which holds these hydrogen atoms together in a cluster. The number of hydrogen atoms in a cluster can be 1,2,3,..., n. The cluster assumes a formula of H(H₂)_n⁻, or H₂(H₂)_n⁻.

1.3.2.2 Hole-sharing poly-hydrogen molecular orbit

If there is a positively charged hydrogen atom, H⁺, or molecule, H₂⁺, it may also form a poly-atomic bridge bond with other hydrogen atoms and/or molecules. In this bridge bond, the 1s orbits of the involved hydrogen atoms overlap each other and hold the atoms in a cluster by sharing this positive charge (electron hole). The number of hydrogen molecules in a cluster may be 1,2,3,..., n. The cluster assumes a formula of H(H₂)_n⁺, or H₂(H₂)_n⁺.

1.4 Observed Hydrogen Clusters

A cluster is a group of bound atoms at a size between a molecules and a solid. Such substances normally have weak bonding and are stable only at cryogenic conditions or under substantial externally applied fields. Neutral clusters are very weakly bonded by van der Waals force. Whaley [5] observed hydrogen clusters by expanding pure hydrogen gas at cryogenic conditions. More recently, Tejada and co-workers [6] produced Para-H₂ clusters by using the same method for pressures from 1 bar to 0.006 mbar and for temperatures from 24 to 60 K. They observed clusters (pH₂)_N with N from 2 to 8 by using Raman Spectroscopy. Later computer simulation work predicted the (pH₂)_N clusters with N from 3 to 50 and showed that the clusters exhibit a clear geometrical order [7]. However, hydrogen ion clusters have attracted more attention because ionization makes hydrogen easier to handle. Because of the long range ion-molecules interactions, such clusters grow and exist in a more simple way. Due to the different interaction mechanisms, hydrogen ion clusters may have quite different structures and properties from their neutral species.

1.4.1 Hydrogen ion clusters

Observations of hydrogen ion clusters have been reported by several researchers. Hiraoka and Kebarle [8] studied the stabilities of H_n⁺ for n=3, 5, 7, 9. They produced hydrogen ion clusters by using a short pulse of electrons reacting with pure hydrogen gas at pressures 2-6 torr, and investigated the clusters by using a high ion source pressure mass spectrometer. Their Van't Hoff plots of equilibria H_n⁺+H₂=H_{n+2}⁺ showed that the dissociation enthalpies were 9.6, 4.1, 3.8, and 2.4 kcal/mole for n=3, 5, 7, 9, respectively. Beuhler et al [9] also studied the H₃⁺+H₂=H₅⁺ and H₅⁺+H₂=H₇⁺ equilibria in a corona discharge ion source at a temperature of 15 K and pressure of 1atm, and detected the clusters in a mass spectrometer. Their calculations of dissociation enthalpy for H₅⁺ and H₇⁺ clusters were 6.6 and 3.1 kcal/mole. Okumura and coworkers [10] produced more hydrogen clusters by using both corona discharge (~200 Torr, 0°C) and electron impact ionization (10⁻⁵ torr). They identified hydrogen clusters H₅⁺, H₇⁺, H₉⁺, H₁₁⁺, H₁₃⁺, and H₁₅⁺ by infrared spectroscopy. Negative hydrogen ion clusters H₁₆⁻ have been reported by Mills [11]. He identified the ion clusters by various characterization techniques such as ToF-SIMS (Time of Flight Secondary Ion Mass Spectroscopy), XPS (X-ray photoelectron spectroscopy), etc, in K₂CO₃ electrolytes that were concentrated in a rotary evaporator at 50 °C.

Theoretical and modeling works have also been conducted in various levels of calculations. The basic methods belong to either the *ab initio* models [12-14] or density functional theory (DFT) [15-17]. Both methods concluded that hydrogen clusters consist of H₂ units surrounding a H₃⁺ core structure. For the hydrogen clusters H₂₇⁺, the center three hydrogen atoms share one positive electron hole, and other H₂ ligands about the H₃⁺ core. In H₉⁺, three H₂ molecules are arranged symmetrically around the H₃⁺ core with the direction perpendicular to the core triangle. As the

clusters get bigger, more and more external hydrogen molecules are lying above and below the H_3^+ plane, and also are making a spherical shell.

As the cluster size n increases, the distance between the core triangle and external molecules increases, and the dissociation energies decreases. As the clusters grow, the interaction between the electron-hole delocalization and ion-molecules polarization becomes significantly reduced, resulting in lower bonding energies. Moreover, when the external molecules surround the H_3^+ core symmetrically; the dissociation energies from the calculations differ significantly, for example, 18.0 kJ/mole for H_7^+ and 15.8 kJ/mole for H_9^+ [18]. This is because the charge migrates smoothly from the internal cluster (H_3^+ core) to the external hydrogen molecules. From the calculations [13], when the cluster size increased from H_{13}^+ to H_{17}^+ , the charge localized at the H_3^+ center decreased from 66.4% to 64.2%.

1.4.2 Metal hydrogen clusters

Hydrogen could form clusters with other substances besides hydrogen ions. A big category includes the metal hydrogen complex. Metal hydrides are of considerable interest as potential hydrogen storage materials. However, metal hydrides maintain their crystal structures so that hydrogen capacity is limited by covalence electrons. When the metals were in their liquid or gases states, more hydrogen could be bonded. Several researchers have reported on hydrogen interaction with metals or metal ions at the molecules level.

Gagliardi and coworkers [19] conducted DFT computation on metal hydrogen complex at molecules level. They claimed that the MH_{12} such as WH_{12} , MoH_{12} , VH_{12}^- , and TiH_{12}^{2-} are stable substances. Bauschlicher et al. [20] also reported DFT computational study on $Co(H_2)^{n+}$ clusters from $n=1$ to 6. Their calculated bonding energies are consistent with experimental results from Kemper et al [21], who reported that binding energy for six H_2 molecules in $Co(H_2)^{n+}$ were 18.2, 17.0, 9.6, 9.6, 4.3 and 4.0 kcal/mol. A similar experiment was conducted on Sc^+ and H_2 clusters [22]. The Sc^+ ions were produced via surface ionization of $ScCl_3$ on a hot filament (about 2500 K). The ions were injected into a reaction chamber containing H_2 at pressure 3 Torr and temperature 300 K. The ion clusters were detected by a quadrupole mass analyzer. The measured dissociation energies of $Sc(H_2)^{n+}$ were 6.4, 5.4, 5.0, and 4.5 kcal/mole, for $n=2$ to 5. The same experimental system was used to generate and identify $Ti^+(H_2)_{1-6}$ clusters [23], except the ion source material was $TiCl_4$. The associated binding energies were 7.5, 9.7, 9.3, 8.5, 8.2, 8.7 kcal/mole for $n=1-6$, respectively. Their corresponding DFT calculation predicted the geometry of the clusters. The $Ti^+(H_2)_5$ has C_{2v} symmetry, and $Ti^+(H_2)_6$ has D_{2d} symmetry. The H_2 molecules arrangement around the Ti^+ core depends on the calculation of the lowest energy.

The same research group also studied bonding interaction of Cu_2^+ ions with H_2 molecules [24]. The Cu_2^+ ions were generated from a copper anode in a glow discharge using an Ar bath and then mass selected and injected into a chamber with hydrogen gas at 2-4 Torr. The clusters

formed and were withdrawn by a small electric field and then detected by a mass analyzer. The bond dissociation energies of H₂ ligands are 12.4, 10.1, 4.9, 3.8, 2.1 and 1.7 kcal/mol for n=1-6, respectively. The same experimental and computational work has been done for alkali metal ions. Bushnell and coworkers [25] studied Na⁺(H₂)_{1,2} and K⁺(H₂)_{1,2} clusters by using the same methods as described above. The dissociation enthalpies were found to be 2.45 and 2.25 kcal/mol for Na⁺H₂ and Na⁺(H₂)₂, and 1.45 and 1.26 kcal/mol for K⁺H₂ and K⁺(H₂)₂, respectively. Their *ab initio* calculations confirmed that the bonding is dominated by electrostatic interaction with very weak covalent interaction. Emmeluth et al [26] reported the observation of Li⁺(H₂)_n with n=1-3 cation clusters and their corresponding infrared spectra. They produced cation clusters by passing supersonic expanded H₂ (8 bars) gas over a metal rod irradiated by a pulsed laser, where the Li ions were generated. Infrared spectra of the clusters were later detected by a tunable IR source. The spectra of a different stretch band and redshifts predicted the Li⁺(H₂)₂ clusters have a H₂-Li⁺-H₂ equilibrium structure with the H₂ molecules on opposite sides of the Li⁺ ion and the Li⁺(H₂)₃ cluster has a trigonal D₃ symmetry.

Fundamental theoretical work has been proposed to explain the bonding behavior of interactions between metal ion and hydrogen molecules. Alkali metal ions such as Na⁺, K⁺, and Li⁺, have closed electron shells, so the charge quadrupole and charge induced dipole electrostatic interactions are the major contributors to the bonding with hydrogen. Such interactions have relative low energy in comparison with the covalent bond and result in lower dissociation energies as described above that only 2.45 kcal/mol for Na⁺H₂. However, for first row transition metals, e.g. Sc⁺, Ti⁺, and Co⁺, the bonding is more complex. One example is that if only the ion induced dipole interaction were considered for Co⁺, the calculated bond energy would be only 4.6 kcal/mol, as the experimentally measured bond energy was 18.2 kcal/mol [23]. There must be other bonding or electron correlations associated with such larger bonding energy. Three electronic interactions have been proposed [22, 24]. First, the electrons from H₂ σ orbital could be donated to the metal 3d orbital or 4s orbital. Metal ions with unfilled 3d or 4s orbital would have this kind of mechanism. Second, for transition metals with filled 3d orbital, back donation from metal dπ orbital to hydrogen σ* antibonding orbital can break up the hydrogen molecules to form atomic hydrogen. Third, the metal ions may form 3d-4s hybrid orbital in order to minimize Pauli repulsion. By comparing these three bonding, the charge induced dipole interaction was found to contribute minimally to the overall bonding energy. From the above experimental examples and computational calculations, the bonding energy of H₂-M⁺ varies among all the hydrogen molecules and it depends on the valence configuration of the metal ions. Also for different metals, the bonding energies varied depending on the electrons of 3d or 4s orbital.

1.4.3 Non-metallic hydrogen clusters

Hydrogen molecules can also interact with water ions. Bae and coworkers [27] first reported the observation of the H₃O⁺(H₂)_n clusters concurrently with the formation of H₃⁺(H₂)_n by electron impact ionization of hydrogen gas. Several species of H₃O⁺(H₂)_n, with n=1-4 have been detected.

Mills [82] also observed hydrogen ion clusters on water molecules as large as $\text{H}_3\text{O}^+(\text{H}_2)_{10}$ concurrently with negative cluster H_{16}^- .

Besides water, Moroni et al [28] reported both experimental observations and Quantum Monte Carlo simulations on *para*-hydrogen clusters with carbon monoxide. They produced $\text{CO}-(\textit{para}\text{H}_2)_N$ clusters by passing mixture gas of 0.01% CO, 3% *para* H_2 , and ultrahigh helium through a pulsed supersonic jet. The clusters were recorded using a cooled ($-80\text{ }^\circ\text{C}$) pinhole jet nozzle and infrared spectra. They have identified $\text{CO}-(\textit{para}\text{H}_2)_N$ clusters from $N=1$ up to 14. The simulation work showed that the first six H_2 molecules were arranged around the oxygen end of the CO with the buildup of hydrogen toward the carbon end as more hydrogen molecules were attached. The first salvation shell was completed at $N=12$ and the cluster had nearly spherical structure with N greater than 12. Such bonding is mostly due to the polarized dipole electrostatic interaction.

1.5 Potential Molecular Composition of Perhydrides

A perhydride molecule could contain one or more hydrogen ion clusters bonded by poly-hydrogen molecular orbits. The molecule should also contain functional atom or atoms that stabilize (charge compensate) the hydrogen ion clusters. Expected perhydrides would include metal perhydrides and non-metal perhydrides. When a perhydride is stabilized with metal atom or atoms, the perhydride is a metal perhydride. Figure 1.2 illustrates a molecular structure proposed for metal perhydrides. When a perhydride is stabilized with non-metal atom or atoms, the perhydride is a non-metal perhydride. Figure 1.3 illustrates a molecular structure proposed for non-metal perhydrides. Another possibility is that a positive hydrogen ion cluster is stabilized with a negative hydrogen ion cluster. This is illustrated in Figure 1.4.

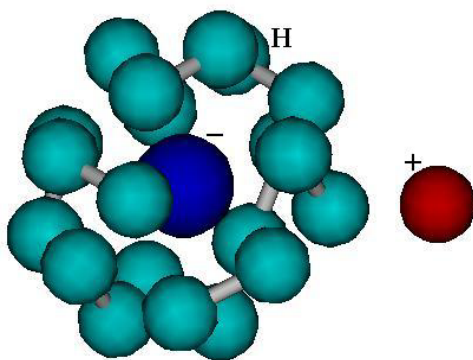


Figure 1.2. The structure of a metal perhydride molecule

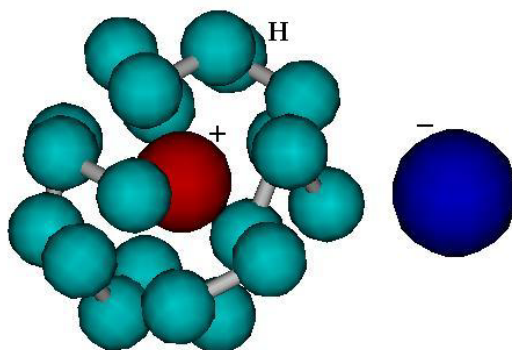


Figure 1.3. The structure of a non-metal perhydride molecule

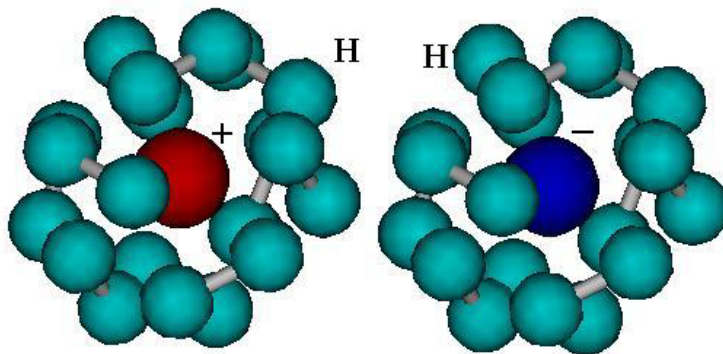


Figure 1.4. The structure of a perhydride molecule containing both positive and negative hydrogen clusters

1.6 Objectives

The objectives of this study are to determine the promising perhydride compounds through various modeling and to explore approaches that can lead to the formation of perhydride molecules.

1.7. Approaches

Based on the discussion above, it is clear that ions or electric charges are involved for the formation of various hydrogen clusters. Therefore, we investigated the systems that have the mechanisms to create ions or electric charges for hydrogen storage. In this study, we investigated

the generation of hydrogen ions (plasma) at low temperatures with a microwave approach. It is difficult to obtain free, suspended charges in a space. To overcome this, we applied electric field on various sorbents to introduce the charges. This report documents the findings of these approaches.

1.8 Section 1 References

- [1] F. Albert Cotton, and Geoffrey Wilkinson, F.R.S., *Advanced Inorganic Chemistry* (New York, NY: Interscience Publishers, 1972), 156.
- [2] Gary L. Miessler, and Donald A. Tarr, *Inorganic Chemistry* (Englewood Cliffs, NJ: Prentice Hall, 1991), 80.
- [3] F. Albert Cotton, and Geoffrey Wilkinson, F.R.S., *Advanced Inorganic Chemistry* (New York, NY: A Wiley-Interscience Publishers, 1988), 188-189.
- [4] John A. Dean, *Lange's Handbook of Chemistry* (New York, NY: McGraw-Hill, Inc., 1992), 4.13
- [5] R. N. Barnett and K. B. Whaley, *Zeitschrift für Physik D Atoms, Molecules and Clusters*, 31 (1994) 75-84, "Molecules impurities in helium clusters".
- [6] G. Tejeda, J.M. Fernández, S. Montero, D. Blume, and J. P. Toennies, *Physical Review Letters*, 92 (2004) 223401-223404, "Raman Spectroscopy of Small Para-H₂ Clusters Formed in Cryogenic Free Jets".
- [7] Jesús Navarro and Rafael Guardiola, *Journal of Low Temperature Physics*, 148 (2007) 857-861, "Energetics and Structure of Small Para-Hydrogen Clusters".
- [8] K. Hiraoka and P. Kebarle, *Journal of Chemical Physics*, 62 (1975) 2267-2270, "A Determination of the Stabilities of H₅⁺, H₇⁺, H₉⁺ and H₁₁⁺ from Measurement of the Gas Phase Ion Equilibria H_n⁺ + H₂ = H_{n+2}⁺ (n = 3,5,7,9)".
- [9] R. J. Beuhler, S. Ehrenson, and L. Friedman, *Journal of Chemical Physics*, 79 (1983) 5982-5990, "Hydrogen cluster ion equilibria".
- [10] M. Okumura, L. I. Yeh, and Y. T. Lee, *Journal of Chemical Physics*, 88 (1988) 79-91, "Infrared Spectroscopy of the Cluster Ions H₃⁺(H₂)_n".
- [11] R. Mills, *Fusion Technology*, 37 (2000) 157-182, "Novel hydrogen compounds from a potassium carbonate electrolytic cell".
- [12] M. Farizon, H. Chermette, and B. Farizon-Mazuy, *Journal of Chemical Physics*, 96 (1992) 1325-1332, "Structure and energetic of hydrogen clusters. Structures of H₁₁⁺ and H₁₃⁺. Vibrational frequencies and infrared intensities of the H_{2n+1}⁺ clusters (n=2-6)".
- [13] M. Barbatti, G. Jalbert, M. A. C. Nascimento, *Journal of Chemical Physics*, 113 (2000) 4230-4237, "Isomeric structures and energies of H_n⁺ clusters (n=13, 15, and 17)".
- [14] Y. Ohta, K. Ohta, and K. Kinugawa, *Journal of Chemical Physics*, 121 (2004) 10991-10999, "Quantum effect on the internal proton transfer and structural fluctuation in the H₅⁺ cluster".

- [15] I. Štich, D. Marx, M. Parrinello, and K. Terakura, *Journal of Chemical Physics*, 107 (1997) 9482-9492, "Protonated hydrogen clusters".
- [16] B. Farizon, M. Farizon, H. Razafinjanahary, and H. Chermette, *Physical Review B*, 60 (1999) 3821-3828, "Structure and energetic of H_{15}^+ hydrogen clusters".
- [17] H. Chermette, and I. V. Ymmud, *Physical Review B*, 63 (2001) 1654271-16542710, "Structure and stability of hydrogen clusters up to H_{21}^+ ".
- [18] H. Chermette, H. Razafinjanahary, and L. Carrion, *Journal of Chemical Physics*, 107 (1997) 10643-10651, "A density functional especially designed for hydrogen-only systems".
- [19] L. Gagliardi, and Pekka Pyykkö, *Journal of American Chemical Society*, 126 (2004) 15014-15015, "How many hydrogen atoms can be bound to a metal? Predicted MH_{12} species".
- [20] C. W. Bauschlicher, Jr., and P. Maitre, *Journal of Physical Chemistry*, 99 (1995) 3444-3447, "Structure of $Co(H_2)_n^+$ clusters, for $n=1-6$ ".
- [21] P. R. Kemper, J. Bushnell, G. V. Helden, and M. T. Bowers, *Journal of Physical Chemistry*, 97 (1993) 52-58, "Cobalt-hydrogen ($Co^+ \cdot (H_2)_n$) clusters: binding energies and molecules parameters".
- [22] J. E. Bushnell, P. R. Kemper, P. Maitre, and M. T. Bowers, *Journal of American Chemical Society*, 116 (1994) 9710-9718, "Insertion of Sc^+ into H_2 : The first example of cluster-mediated σ -bond activation by a transition metal center".
- [23] J. E. Bushnell, P. Maitre, P. R. Kemper and M. T. Bowers, *Journal of Chemical Physics*, 106 (1997) 10153-10167, "Binding energies of $Ti^+(H_2)_{1-6}$ clusters: theory and experiment".
- [24] M. J. Manard, J. E. Bushnell, S. L. Bernstein, and M. T. Bowers, *Journal of Physical Chemistry*, 106 (2002) 10027-10032, "Origin of bonding interactions in $Cu_2^+(H_2)_n$ clusters: an experimental and theoretical investigation".
- [25] J. E. Bushnell, P. R. Kemper, and M. T. Bowers, *Journal of Physical Chemistry*, 98 (1994) 2044-2049, " $Na^+/K^+(H_2)_{1,2}$ clusters: binding energies from theory and experiment".
- [26] C. Emmeluth, B. L. J. Poad, C. D. Thompson, G. H. Weddle, and E. J. Bieske, *Journal of Chemical Physics*, 126 (2007) 204309, "Infrared spectra of the $Li^+(H_2)_n$ ($n=1-3$) cation complexes".
- [27] Y. K. Bae, P. C. Cosby and D. C. Lorents, *Chemical Physics Letters*, 159 (1989) 214-220, "Observation of shell structures in the growth of microcluster ions".
- [28] S. Moroni, M. Botti, S. De Palo, and A. R. W. McKellar, *Journal of Chemical Physics*, 122 (2005) 094314, "Small *para*-hydrogen clusters doped with carbon monoxide: Quantum Monte Carlo simulations and observed infrared spectra".

2. DENSITY FUNCTIONAL COMPUTATION OF HYDROGEN CLUSTERS

2.1 Introduction

From previous experimental and theoretical work, hydrogen clusters displayed geometrical arrangements and properties that are quite different from their bulk properties. Also the properties could be changed by combining different ions or atoms with hydrogen. Binding energy, number of hydrogen molecules, geometrical configurations of these clusters all varied depending on the strength and direction of the ligand bond. Such diversity of hydrogen clusters has led to their possible applications in hydrogen storage materials. In hydrogen clusters, the number of bonded hydrogen molecules is not limited by the covalent electrons. The total weight percentage of hydrogen in clusters could be highly enhanced. In order to reduce the large amount of experimental work on finding suitable substances to form stable hydrogen clusters, computer simulations could be an easy approach. Also computational work could predict the molecules structure, identify correlations between structures and properties, direct and understand experimental data, and explore the bonding mechanism.

There are two major calculation models in computing hydrogen clusters: *ab initio* and density functional theory (DFT). *ab initio* calculation is from first principles and that no empirical data is used. It is based on the complicated many-electron wavefunction and can be made to lead to the exact solution, when all approximations are sufficiently small in magnitude. However, extremely large computational time and effort have to be applied. In DFT methods, the many-body electronic wavefunction is replaced with the electronic density as the basic quantity. In *ab initio* calculation, the many-body wavefunction is dependent on $3N$ variables, three spatial variables for each of the N electrons. In DFT, the density is only a function of three variables and the computational quantity is simpler and practical. So it can be very accurate for little computational cost. The drawback is that it is not possible to estimate the error of the calculations without comparing them to other methods or experiments. DFT has been the major computational method within recent years especially after the development of hybrid functional.

2.2 Computational Method

Extensive simulation study has been performed to calculate the interaction of hydrogen molecules with different ions, atoms, and compounds in order to lead our late laboratory synthesis. All calculations have been performed based on density functional theory and at 0 K. The basis set used for calculation was 6-311G++G(d,p). B3LYP hybrid functional was proved to be a good approximation for hydrogen complex system [1-4]. In such hybrid functional, the exchange energy from Becke's exchange functional [5] is combined with the exact energy from Hartree-Fock theory to increase the accuracy of the simulation. All computations were conducted by using the GAUSSIAN 03 program [6].

2.3 Results and Discussion

Here, only lower lying electronic states which yield the most stable structures have been simulated. Other higher energy states and isomers are not presented.

2.3.1 Hydrogen clusters on alkaline earth metal ions

As summarized in the last chapter, both experimental and simulation work of group 1 alkaline metal ions have been done. The results showed that the dipole electrostatic interaction dominates the bonding with H_2 . Infer to the group 2 alkaline metal ions, they have stronger dipole interactions which may yield better bonding strength and properties.

The simulated cluster structures of hydrogen bonded to group 2 alkaline metal ions Ba^{++} , Sr^{++} , Ca^{++} , Mg^{++} , and Be^{++} are shown in Figure 2.1. The geometric configurations of hydrogen attaching to the different alkaline ions are calculated to be identical since all these ions have similar electron configuration and a closed electron shell. The distances of each hydrogen molecule to the center of the ions are equal. In $M^{++}-2H_2$, two hydrogen molecules are placed on the opposite sides of the center ion, and the angle between them is 90° . The geometry exhibited D_{2d} symmetry. Adding one more hydrogen molecule, in $M^{++}-3H_2$, the steric arrangement changed to C_3 symmetry. The three hydrogen molecules are in the same plane and the metal ion locates at the center. $M^{++}-4H_2$ has T_d symmetry. The metal ion is at the center of a tetrahedral structure, and the hydrogen molecules locate at the four corners of the tetrahedron. The opposite hydrogen molecules are perpendicular to each other. As one more hydrogen was added on in $M^{++}-5H_2$, the cluster changed to high symmetrical O_h arrangement. The center of each hydrogen molecule sits at the six corners of an octahedral structure, where the metal ion stands at the center. The hydrogen at each opposite corner is parallel to each other. The $M^{++}-6H_2$ exhibits the same highest symmetry O_h , where hydrogen molecules locate at the eight points of a cubic structure and the metal ion sits at the center. The molecules at the opposite corner in the front are parallel to each other and also parallel to the back side of the cube, but perpendicular to the other four molecules.

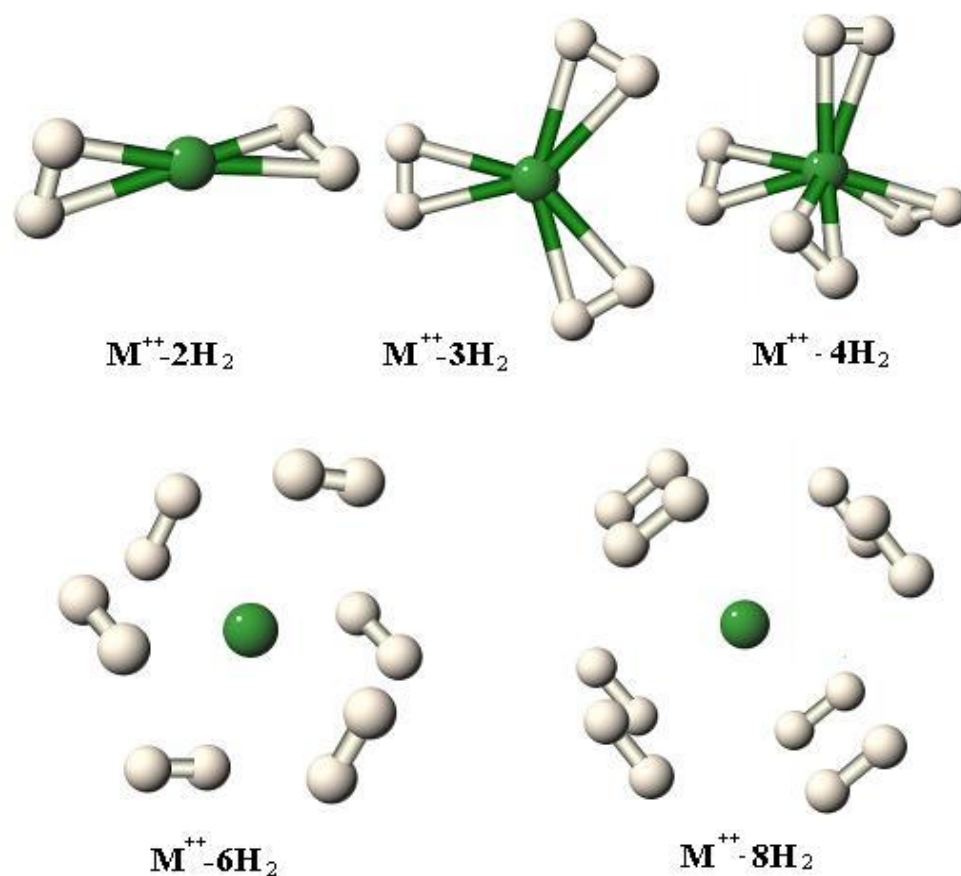


Figure 2.1. Simulated structures of hydrogen-alkaline metal ion clusters $M^{++}(H_2)_n$

In order to compare the distance which represents the interaction of the center ion and hydrogen molecules, the distances between the outer H_2 subunit and the center of M^{++} are reported in Figure 2.2. These lengths were calculated as the distance between the center of the hydrogen molecules and the center of metal ions. Comparing the five ion clusters $M^{++}nH_2$, $Be^{++}nH_2$ has the shortest distance between ion and hydrogen, and $Ba^{++}nH_2$ has the longest distance with Mg^{++} , Ca^{++} , and Sr^{++} in between and in the order of $Mg^{++} < Ca^{++} < Sr^{++}$. This is consistent with the increase of the ionic radii of the metal ions, as Be^{2+} 59 pm, Mg^{2+} 86 pm, Ca^{2+} 114 pm, Sr^{2+} 132 pm, and Ba^{2+} 149 pm. When n in the clusters increases (more hydrogen molecules are bonded to the metal), the distance between ion and hydrogen remains almost constant in Ba^{++} , and Sr^{++} , with slight increase in Ca^{++} when $n=6$, and large increase in Mg^{++} and Be^{++} . This can also be understood from the radii of the ions. When the metal ion is small such as Be^{++} and Mg^{++} , the outer shell space for hydrogen to be occupied is limited. As more hydrogen molecules are introduced, the clusters have to expand in order to contain all the hydrogen molecules. On the other hand, large ions such as Ba^{++} , and Sr^{++} , the outside orbital are big enough to contain all the hydrogen so that the bond length is not affected by the number of hydrogen molecules.

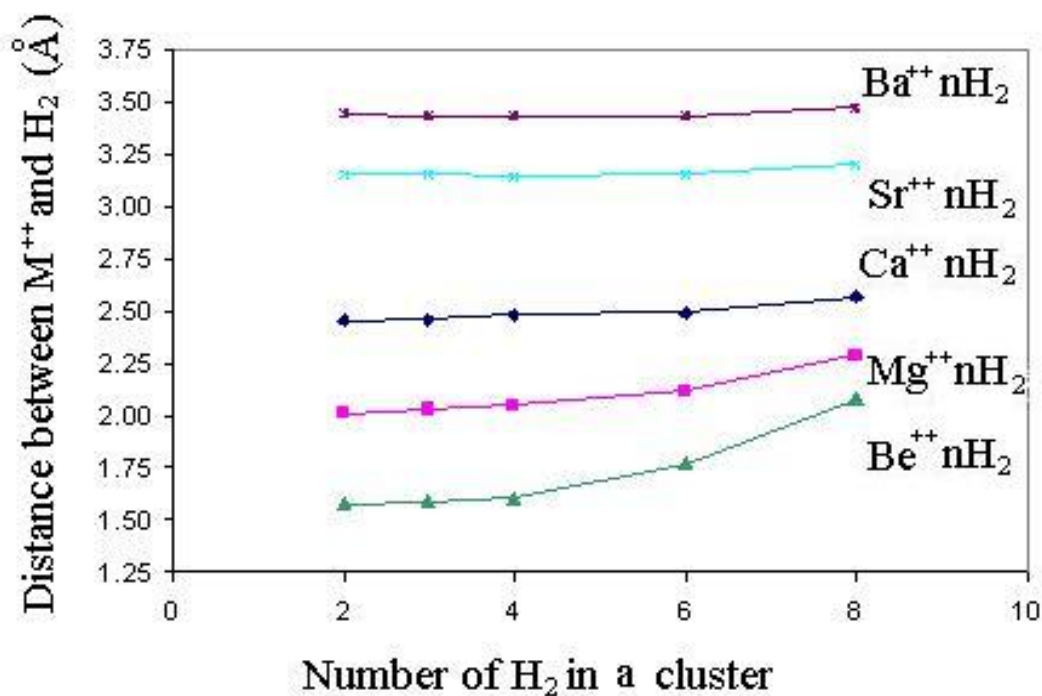


Figure 2.2. Calculated distance between M⁺⁺ and H₂ as a function of number of H₂

The H-H distances in the H₂ molecules are shown in Figure 2.3. The bond length H-H of Ba⁺⁺nH₂ was found to be around 0.742 Å, which is almost equal to the bond length of hydrogen gas (0.74 Å). This indicates that the hydrogen H₂ is not perturbed by the interaction of these molecules and the nucleus of the cluster so that the bond strength of hydrogen and ion is weak. And the number of hydrogen molecules in the cluster doesn't affect the H-H bond distance because the distance between hydrogen and center ion doesn't show any obvious change. The H-H bond in Sr⁺⁺nH₂ exhibits the same behavior, except that the bond length is larger corresponding to a slightly stronger bond to the nucleus. Ca⁺⁺nH₂ has the same properties with only the bond length increased to 0.76 Å. In Mg⁺⁺2H₂, the H-H distance is about 0.778 Å, and it decreases slightly as more hydrogen is added to the clusters. When n equals 2, the H-H bond was more stretched indicating a stronger bond to the nucleus. However, when the cluster grows, the distance between H₂ and nucleus enlarges (as in Figure 2.3), which results in a looser cluster bond so that less perturbation results in H-H bond. Be⁺⁺nH₂ has the highest H-H bond length (largest H-H stretch) which indicates the strongest bond between hydrogen and center ion among all the five ion clusters. The decreasing trend of H-H distance as the increasing number of H₂ in the cluster is the most significant. This is also consistent with the change of distance between hydrogen and nucleus as the cluster grows.

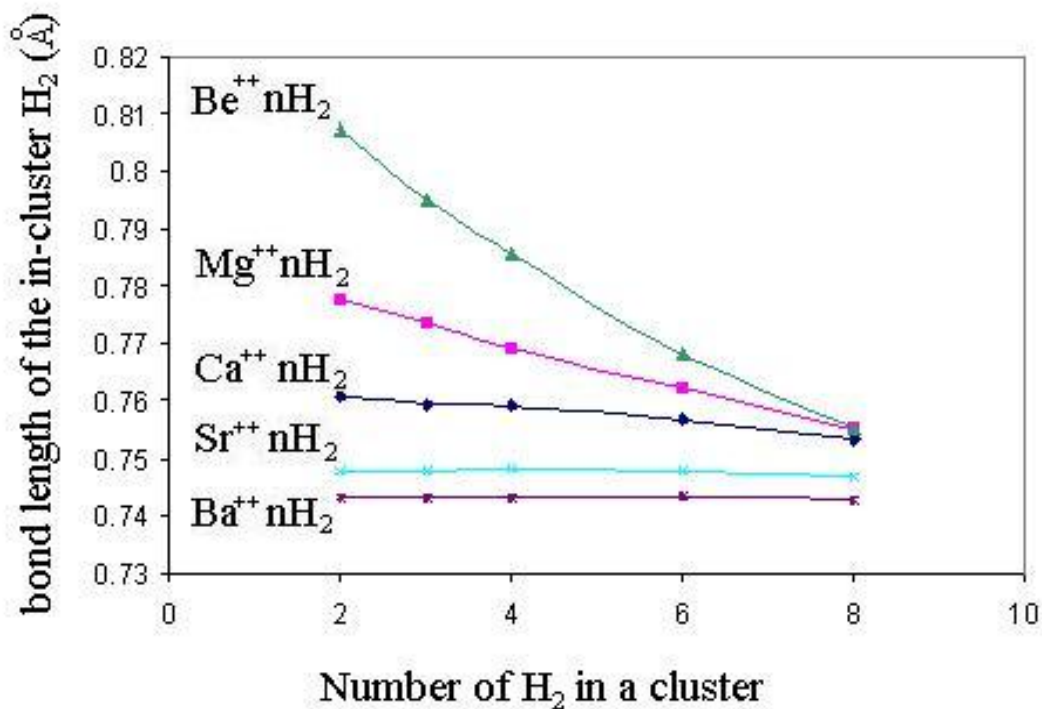


Figure 2.3. Calculated bond length of H-H in the clusters

The stability of the clusters can be investigated through the dissociation energies of the clusters. As in Figure 2.4, Be⁺⁺nH₂ is the most stable clusters with the highest total binding energy and Ba⁺⁺nH₂ is the least stable. As the number of H₂ in clusters Ba⁺⁺nH₂, Sr⁺⁺nH₂, and Ca⁺⁺nH₂ increases, the total gain of energy also increases. However, each hydrogen-nucleus bonding is weakened as the cluster grows, which is consistent with the hydrogen-nucleus distance and hydrogen bond distance. Mg⁺⁺nH₂ and Be⁺⁺nH₂ clusters exhibited decreased gain of energy as the clusters grow from n=6 to n=8 although the energy trend of n<6 is the same as other clusters. So n=6 clusters for Mg⁺⁺nH₂, and Be⁺⁺nH₂ are more stable than n=8.

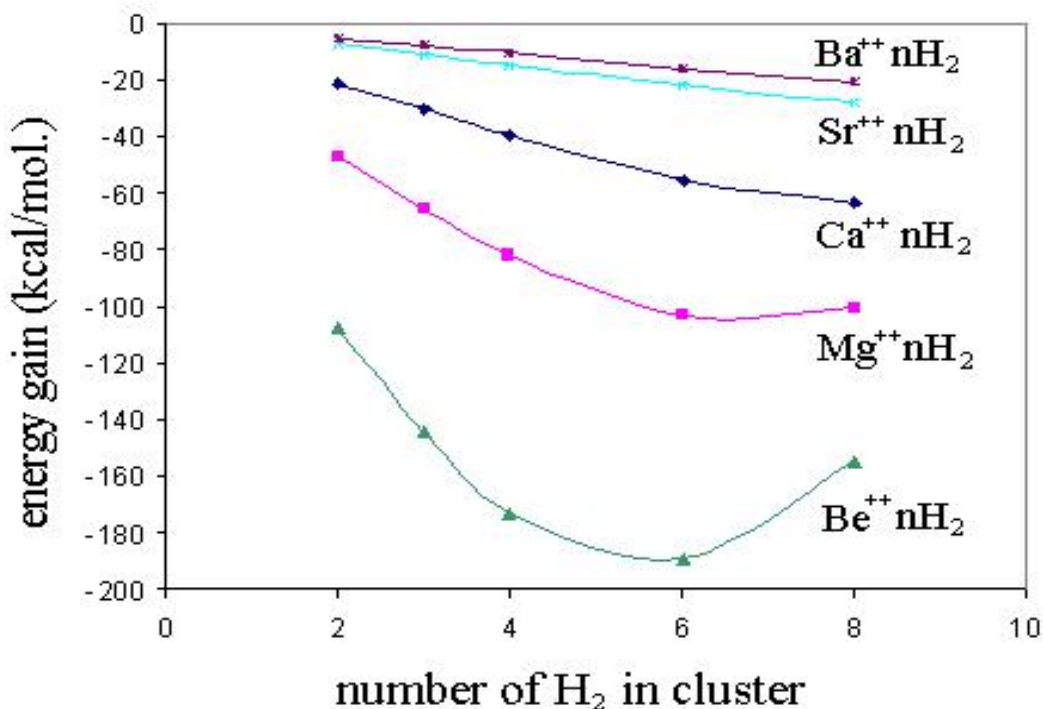


Figure 2.4. Stabilization energies of $M^{++}nH_2$ clusters

For alkali earth metals, smaller metals appear to have more stable hydrogen clusters with number of H_2 up to 8. The bonding energy of $Ba^{++}nH_2$ and $Sr^{++}nH_2$ are too small and these clusters are very easy to decompose when the temperature is increased. The most stable cluster is $Be^{++}nH_2$, however, Be is a very toxic element which could not be considered as a useful materials in application. Therefore, only $Ca^{++}nH_2$ and $Mg^{++}nH_2$ may have potential to be used as hydrogen storage clusters.

2.3.2. Negative charged ion clusters

Based on the principle of ion-induced electrostatic bond or the theory of ligand bond, negative charged ions also have the potential to form hydrogen clusters. Two negative ions O_2^- and Cl^- have been calculated.

Figure 2.5 shows the fully optimized geometry of $[O(H_2)_8]^{2-}$ with D_{4h} symmetry, predicted from the DFT calculation. The optimized structure parameters such as bond length, angles, and predicted energy are also complied in Figure 2.6. In this cluster, eight H_2 are arranged symmetrically around the anion O^{2-} core. Two pairs of the eight hydrogen molecules are lying above and two pairs are below the horizontal plane. And four other hydrogen molecules are lying inside the central plane. The nearest distance between the hydrogen and the oxygen ion for all

eight H₂ molecules is the same 1.916 Å, which indicates the same bonding energy for all eight H₂ molecules. The O-H-H bond angle is 180° which presents that the bond direction of hydrogen molecules is extended from the O-H bond. The H-H bond is largely perturbed by the interaction between the oxygen ion and the hydrogen molecules and the bond energy should be significantly large. The total binding energy is 118.926 kcal/mol, which lies between Mg⁺⁺8H₂ and Be⁺⁺8H₂.

The calculated [Cl(H₂)₈]⁻ cluster is shown in Figure 25. The structure follows *D4h* symmetry and the geometry is identical to that of [O(H₂)₈]²⁻ cluster, except that the bond angle of H₂-Cl-H₃ in [Cl(H₂)₈]⁻ is 0.1 degree smaller. Here, hydrogen molecules stay far away from the central nucleus with a distance of 2.819 Å, which may be due to the large ion size of Cl⁻ (167 pm) compared to O²⁻ (126 pm) and a weak electrostatic interaction. This is also concluded from the small perturbation of H-H bond. The cluster binding energy is small, only 14.605 kcal/mol. Such low energy may cause the cluster to easily decompose at elevated temperatures.

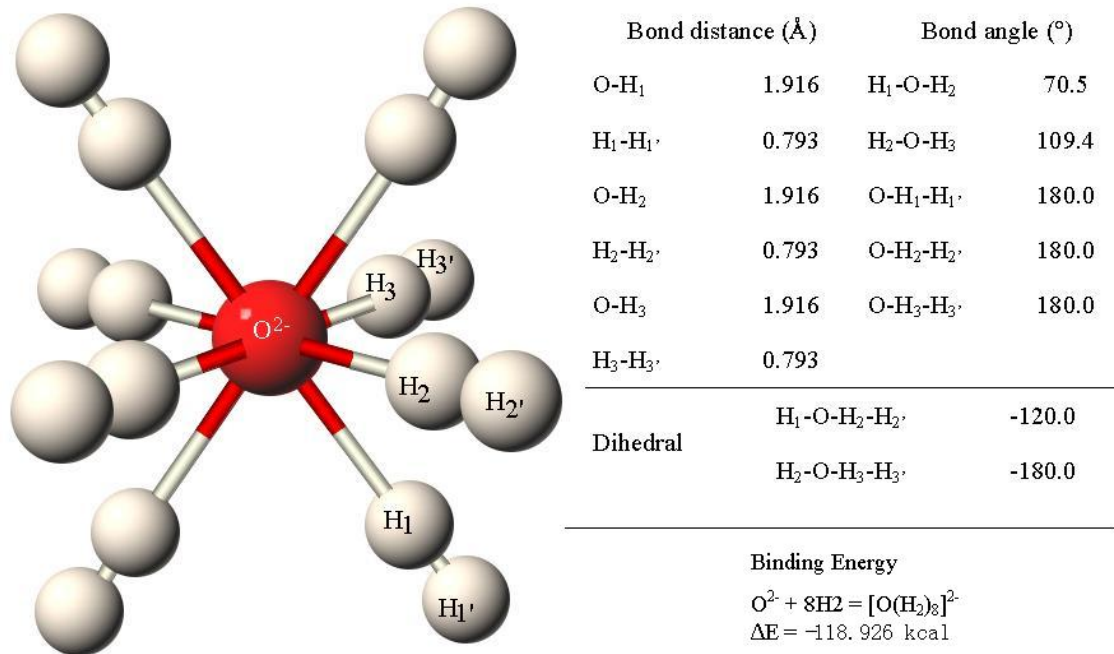


Figure 2.5. Optimized structure of [O(H₂)₈]²⁻

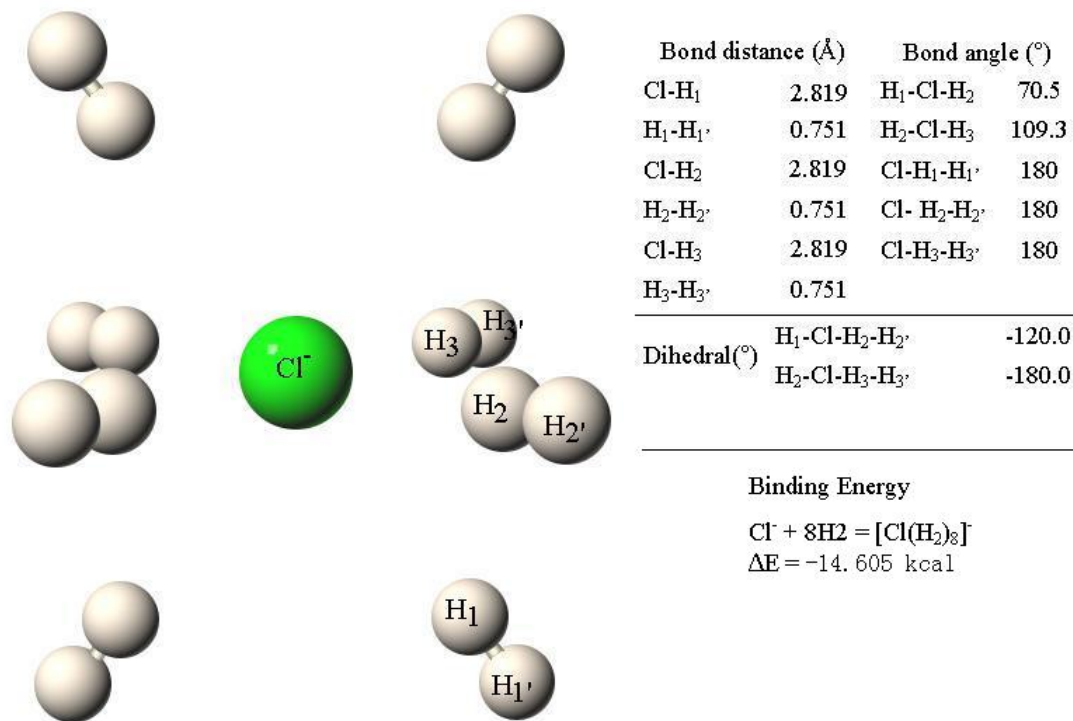


Figure 2.6. Optimized structure of $[\text{Cl}(\text{H}_2)_8]^{2-}$

2.3.3. Clusters with metal oxides

From previous calculations and published results, both the positive ion and negative ion has the potential to bind up to 8 H_2 molecules, which may yield the highest hydrogen capacity of 64 wt% for $\text{Be}^{++}8\text{H}_2$ cluster. However, all these cations or anions are not stable in nature. The applicable substances of these ions would be their oxides, chlorides, or any other compounds. Here, oxides of transition metals were modeled to identify their potential as applicable hydrogen storage materials.

The structure of $\text{VO}(\text{H}_2)_8$ cluster is shown in Figure 2.7. Four of the eight H_2 molecules are bonded near vanadium and the other four near oxygen. The nearest hydrogen ligands (as indicated $\text{H}_2\text{-H}_2'$ in the figure) are at a distance of 1.922 Å to vanadium and a bond angle of 122.5° to the horizontal plane. Two pairs of H_2 are above the V-O plane and two are below. The H-H bond is largely perturbed indicating a large interaction of H_2 to the vanadium. The second largest bonding is between oxygen and hydrogen molecules, as $\text{H}_3\text{-H}_3'$ in the figure. There are four of these types of hydrogen molecules, two of which are lying above and two pairs are below the V-O plane. Each hydrogen molecule bond is at an angle of 173.3° to the O- H_3 bond direction. Here, H-H is not perturbed, only 0.746 Å compared to the bond distance 0.74 Å for free hydrogen gas molecules. The largest bond distance 6.004 Å is observed between vanadium and

H₁-H₁' molecules. The H₁-H₁' bond is even less perturbed and at an angle of 124.8° to the V-H₁ bond. The whole cluster exhibits a C_{2v} symmetry. The total bonding energy of the cluster is 4.13 kcal/mol with probably a large contribution from the V-H₂-H₂' bond and a small amount from the V-H₃-H₃' and the V-H₁-H₁'. Although from previous calculations, bonding of O²⁻ and eight hydrogen can have 118.9 kcal/mol energy, and the hydrogen adsorption energy in oxides was highly weakened.

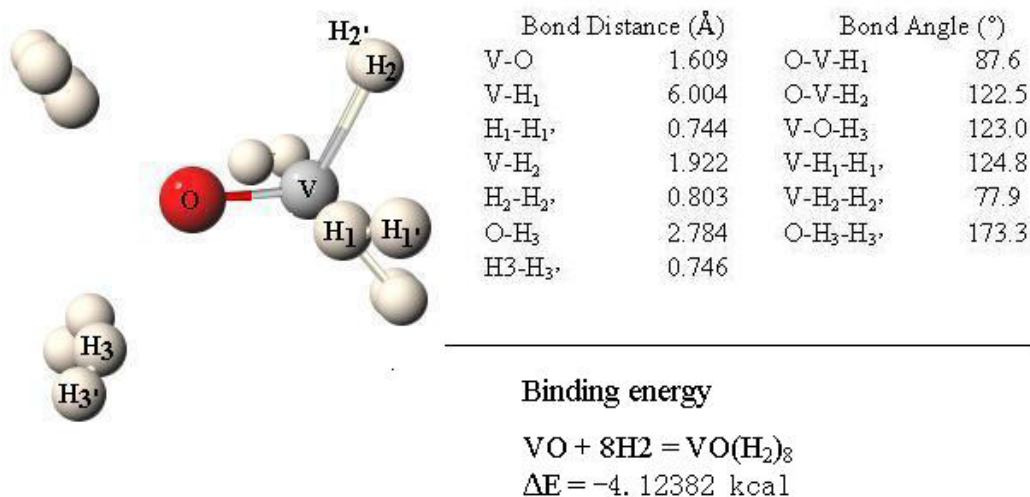


Figure 2.7. Geometry of VO(H₂)₈ cluster calculated from DFT

The CrO(H₂)₈ cluster shows a much larger binding energy, as from Figure 2.8. Here, two types of hydrogen molecules are strongly bonded to the Cr center with the hydrogen molecule center facing the Cr atom. The H₁-H₁' and H₂-H₂' bond distances are largely perturbed to 0.804 Å and 0.889 Å, respectively. H₂ type molecules are arranged in the same plane of the CrO, and H₁ type molecules are straighten along the vertical direction. Such closed accommodation yielding a significant interaction is the results of strong electrostatics. On the oxygen end, the H₃ type hydrogen follows end on adsorption. The distance of O-H₃ is 2.738 Å, shorter than that of VO(H₂)₈ cluster. However, the H₃-H₃' bond length is only 0.745 Å, indicating a weak interaction on the oxygen end.

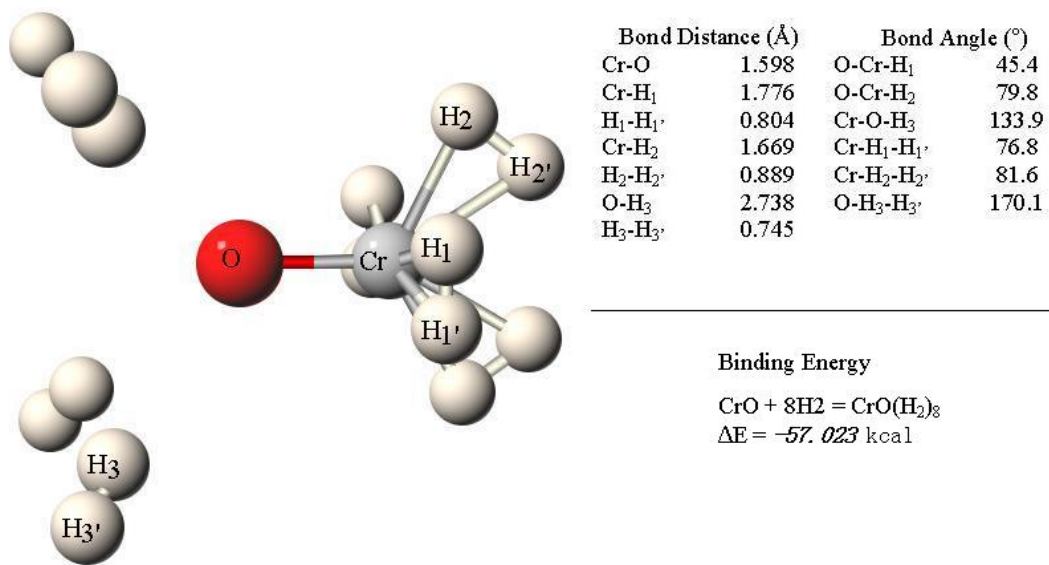


Figure 2.8. Geometry of $\text{CrO}(\text{H}_2)_8$ cluster calculated from DFT

The three types of hydrogen molecules in the $\text{MnO}(\text{H}_2)_8$ cluster (Figure 2.9.) are all weakly bonded to manganese and oxygen. The arrangement of hydrogen molecules is identical to that in $\text{CrO}(\text{H}_2)_8$. The only difference is the larger ion-hydrogen distance in the $\text{MnO}(\text{H}_2)_8$ cluster. Among the three types of molecules, $\text{H}_2\text{-H}_2'$ is the most affected molecule, which has a bond length 0.750 Å. All these indicate a weak electrostatic interaction between MnO and the surrounding hydrogen molecules. Therefore, the binding energy is only 3.552 kcal, even smaller than the $\text{VO}(\text{H}_2)_8$ cluster.

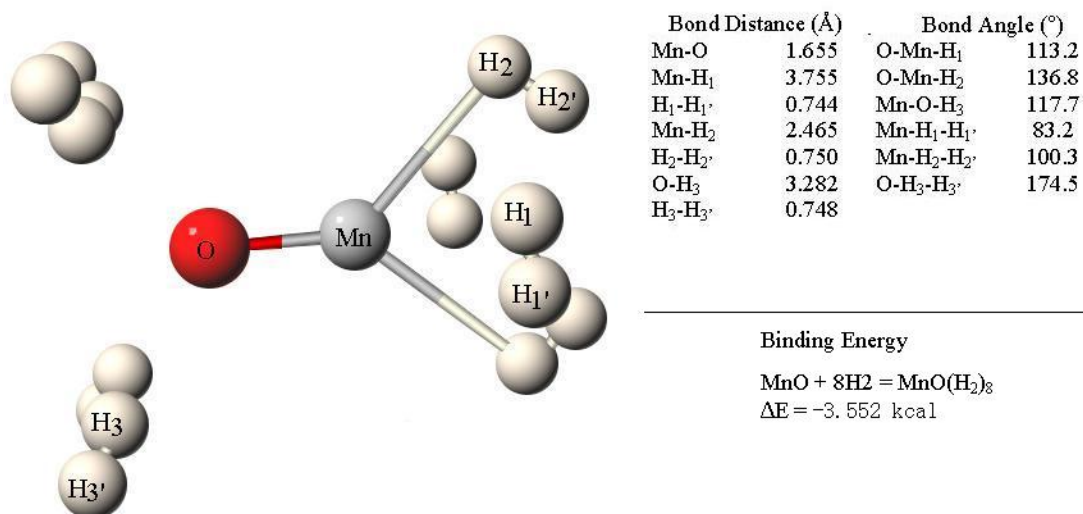


Figure 2.9. Geometry of $\text{MnO}(\text{H}_2)_8$ cluster calculated from DFT

The $\text{FeO}(\text{H}_2)_8$ and $\text{CoO}(\text{H}_2)_8$ clusters have the same symmetry and geometrical configuration as $\text{CoO}(\text{H}_2)_8$ and $\text{MnO}(\text{H}_2)_8$ clusters, as in Figure 2.10 and 2.11. However, the binding energies are much larger, 20.701 kcal for $\text{FeO}(\text{H}_2)_8$ and 20.840 kcal for $\text{CoO}(\text{H}_2)_8$ clusters. The hydrogen molecules at the cation end are largely perturbed and the molecules on the oxygen end follow the weak physisorption. The H_1 and H_2 type molecules are much closer to the cation in the $\text{CoO}(\text{H}_2)_8$ due to the stronger electrostatic force and the smaller ion size of cobalt cation.

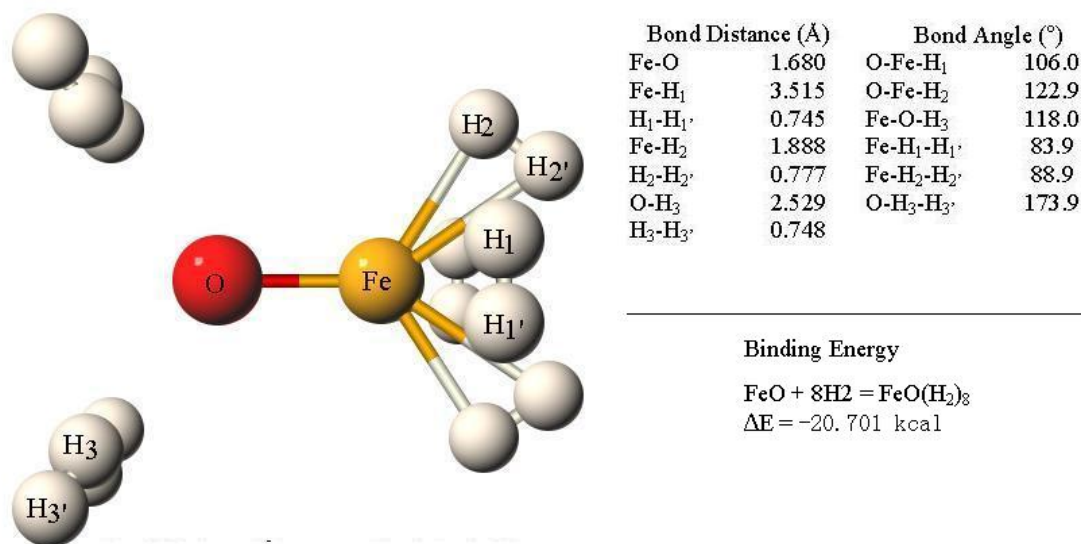


Figure 2.10. Geometry of $\text{FeO}(\text{H}_2)_8$ cluster calculated from DFT

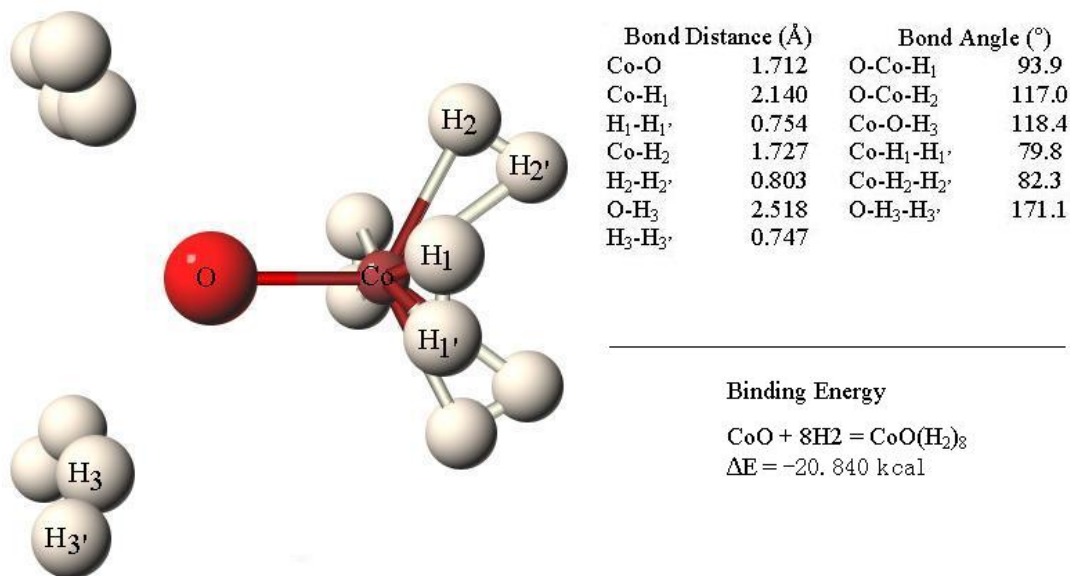


Figure 2.11. Geometry of $\text{CoO}(\text{H}_2)_8$ cluster calculated from DFT

The same calculation was carried out for the $\text{NiO}(\text{H}_2)_8$ cluster and the result is shown in Figure 2.12. The cluster also has a C_{2v} symmetry and presents the same apparent geometry as $\text{VO}(\text{H}_2)_8$ except that the bond distance and angle are quite different. Only $\text{H}_2\text{-H}_2'$ type molecules are largely affected by the nickel ion, and the bond distance is elongated to 0.804 Å. The H_1 type and H_3 type molecules are weakly adsorbed onto the nickel ion and oxygen ion. The overall binding energy of the cluster is remarkably higher at 34.623 kcal.

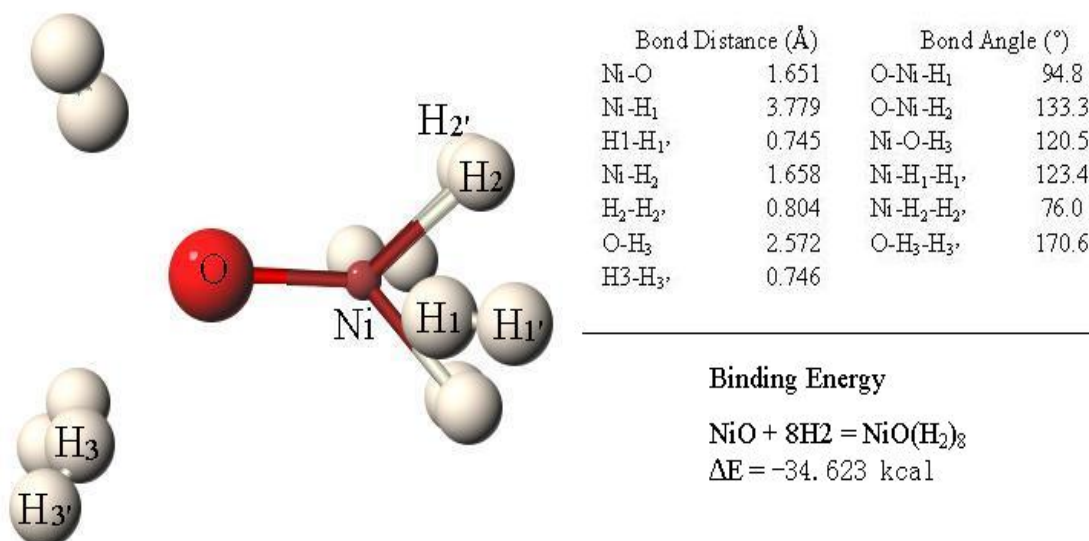


Figure 2.12. Geometry of $\text{NiO}(\text{H}_2)_8$ cluster calculated from DFT

In a short summary, transition metal oxides are capable of binding eight hydrogen molecules with four on the metal cation sites and four on the oxygen sites. The $\text{VO}(\text{H}_2)_8$ and $\text{NiO}(\text{H}_2)_8$ cluster have the same molecule arrangement. And a slightly different type of configuration is observed for other clusters. The total binding energy is ordered as $\text{CrO}(\text{H}_2)_8 > \text{NiO}(\text{H}_2)_8 > \text{CoO}(\text{H}_2)_8 > \text{FeO}(\text{H}_2)_8 > \text{VO}(\text{H}_2)_8 > \text{MnO}(\text{H}_2)_8$. Here, the total energy is not only the sum from the electrostatic or dipole interaction. Since transition metals have the partial filled d orbital, there are other associated mechanisms such as donation of electrons from the hydrogen sigma bond to the d orbital, or the backdonation of d electrons to the hydrogen anti-bonding orbital. Moreover, the different ion size especially on the cation site also influences the molecules arrangement and the total binding energy.

2.3.4. Clusters with gas molecules

In general, the single diatomic molecules barely exist in solid materials. However, the gas molecules usually are interconnected by a weak Vander War force. Each single molecule could be considered as a free substance for hydrogen adsorption. The electrostatic interaction also

exists in the common gas molecules, in which an intrinsic dipole can significantly attract hydrogen molecules. Figure 2.13 shows the optimized geometry of the $\text{CO}(\text{H}_2)_8$ cluster, where a total of eight hydrogen molecules could be bonded with four on each side. Carbon monoxide exhibits a polar structure where the carbon atom is positive charged and the oxygen is negative. However, due to the small atomic number of carbon, the electrostatic force is so weak that the smallest hydrogen-carbon bond is $\text{C}-\text{H}_1$ at 3.536 \AA . And the H_1-H_1 sigma bond is only slightly increased to 0.744 \AA . The total binding energy is positive 0.336 kcal , which means that such a structure is not stable and may easily decompose.

Carbon dioxide is a nearly linear molecule with $\text{O}-\text{C}-\text{O}$ bond angle at 179.8° . The molecule itself is not polarized because the oxygen atoms on each side have the same charge. However, it has two intrinsic dipoles with CO in the opposite direction. Compared to carbon monoxide, the carbon atom in CO_2 is more positively charged and oxygen is more negatively charged. Therefore, the hydrogen interaction should be stronger than that of carbon monoxide. As from Figure 2.14, eight hydrogen molecules are bonded to a carbon dioxide molecule with four hydrogen molecules on each oxygen atom. The $\text{O}-\text{H}$ bond distance is 3.071 \AA for H_1 type molecules and 3.003 \AA for H_2 type molecules. Such a short distance contributes to a strong interaction and good binding energy at negative 0.09844 kcal , therefore the $\text{CO}_2(\text{H}_2)_8$ structure is more stable than the $\text{CO}(\text{H}_2)_8$ cluster.

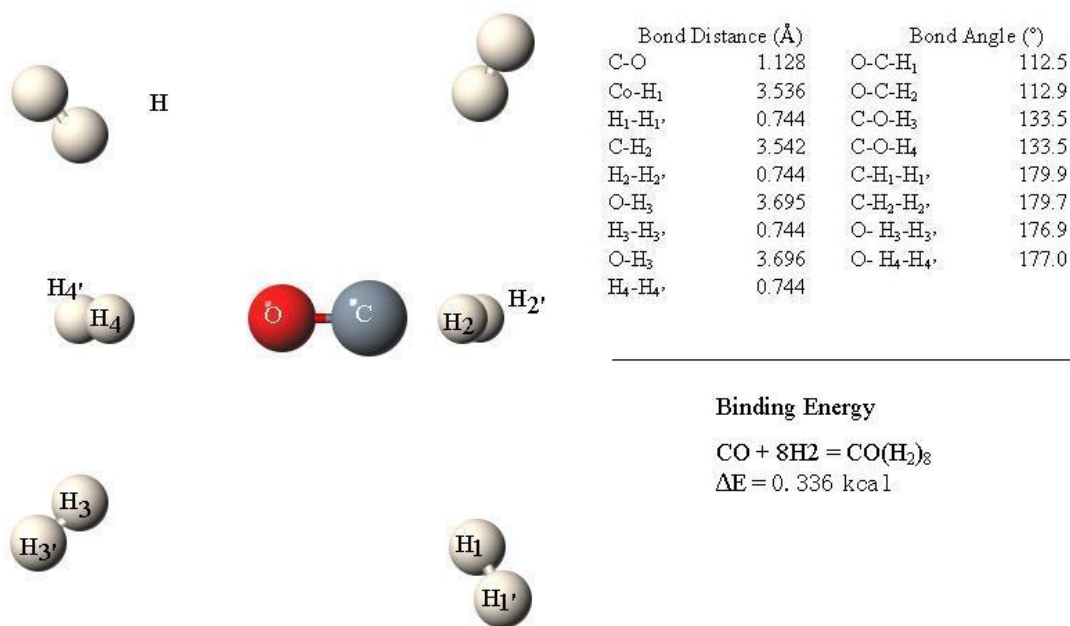


Figure 2.13. Geometry of $\text{CO}(\text{H}_2)_8$ cluster calculated from DFT

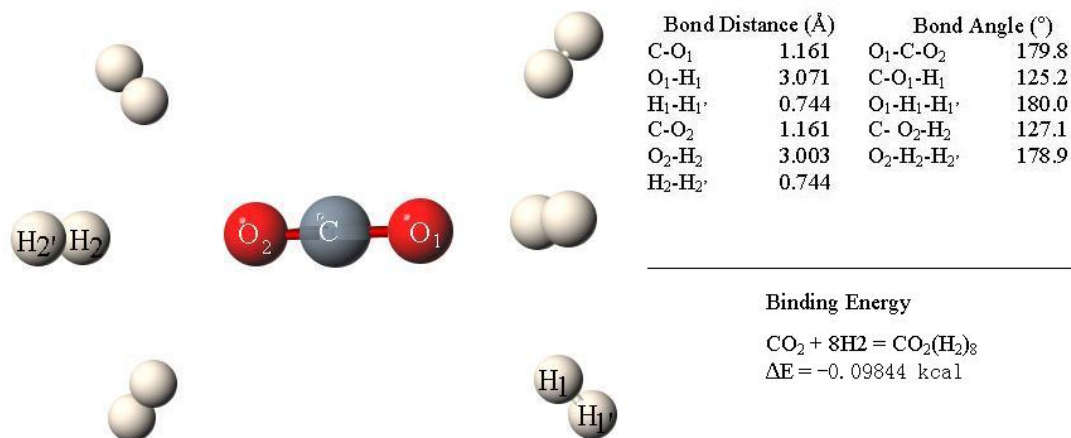


Figure 2.14. Geometry of $\text{CO}_2(\text{H}_2)_8$ cluster calculated from DFT

The hydrogen chloride molecule is an ionic compound which has an intrinsic dipole moment where hydrogen donates an electron that becomes slightly positively charged and chloride accepts an electron that becomes a slightly negative charged. The dipole moment for HCl in the gas phase is 1.08 D [6]. The optimized geometry of $\text{HCl}(\text{H}_2)_8$ cluster is shown in Figure 2.15. At the chloride end, four hydrogen molecules have the characteristic of end on adsorption and the Cl-H distance is quite large at 5.324 Å. The negative charge effect of chloride is negligible. On the other end, two H_3 type hydrogen molecules bonded side on to the positive charged hydrogen atom at a distance of 3.860 Å. The other two $\text{H}_2\text{-H}_2'$ molecules stand above and below the HCl horizontal plane at a distance of 4.093 Å to the hydrogen atom. The shorter distance on the hydrogen end is because the hydrogen atom has a smaller size than the chloride atom and it also could be because the positive charge is more effective in bonding hydrogen molecules. The overall binding energy is negative 0.285 kcal, which is stronger than carbon monoxide and carbon dioxide.

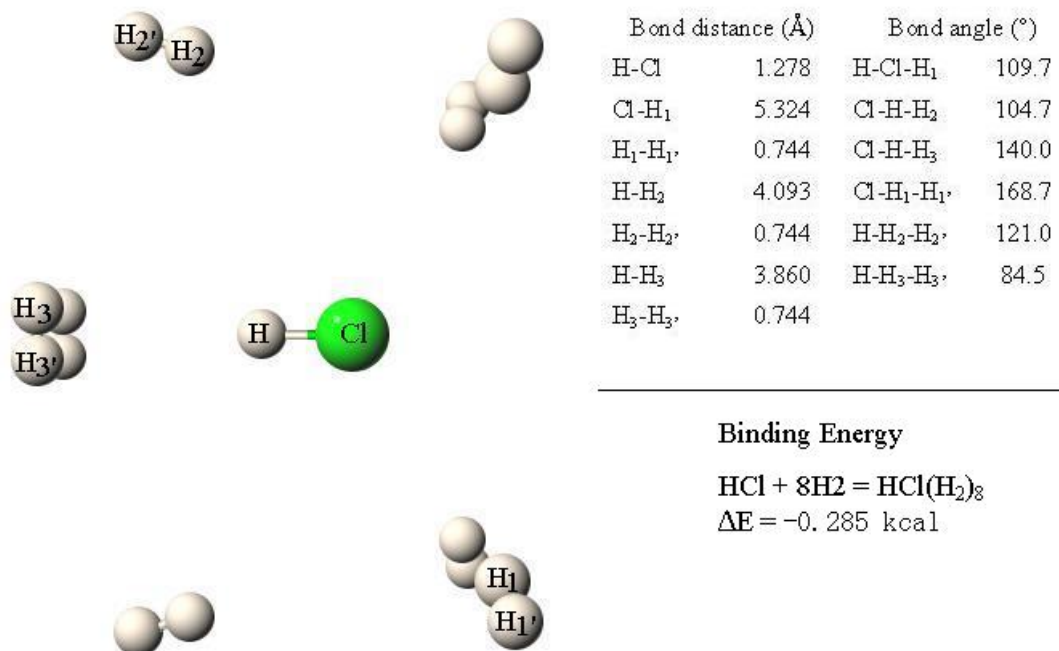


Figure 2.15. Geometry of HCl(H₂)₈ cluster calculated from DFT

2.4 Conclusion

Hydrogen clusters with alkaline metal ions, first row transition metal oxides, and also inorganic gas compounds have been calculated to study the geometry, stability, binding energy and examine the effects of electrostatic interaction on the hydrogen-molecule substances. The alkaline cations can form clusters with up to eight hydrogen molecules. The total binding energy increases with the decreasing of cation size. When the metal cations form oxides with oxygen, the electrostatic force is weakened so that the total binding energy is lowered to some extent. However, the metal oxides can bind up to eight hydrogen molecules and the stability does not follow the pure electrostatic force since some molecules with higher dipole moment result in lower binding energy. Accordingly, there might be other mechanisms such as sigma bond donation and d orbital back-donations due to the partially filled d orbital. Although inorganic gas molecules have free space to accommodate hydrogen, weak dipole moments have made the clusters to have small binding energy and unstable structures. From all these results, hydrogen clusters could be formed based on the electrostatic interaction.

2.5 Section 2 References

- [1] P. J. Stephens, F. J. Devlin, C. F. Chabalowski, and M. J. Frisch, *Journal of Physical Chemistry*, 98 (1994) 11623-11627, "Ab Initio Calculation of Vibrational Absorption and Circular Dichroism Spectra Using Density Functional Force Fields".

- [2] C. Lee, W. Yang, and R. G. Parr, *Physical Review B*, 37 (1988) 785-789, “Development of the Colle-Salvetti correlation-energy formula into a functional of the electron density”.
- [3] A. D. Becke, *Physical Review A*, 38 (1988) 3098-3100, “Density-functional exchange-energy approximation with correct asymptotic behavior”.
- [4] A. D. Becke, *Journal of Chemical Physics*, 98 (1993) 5648-5652, “Density-functional thermochemistry. III. The role of exact exchange”.
- [5] M. J. Frisch, et al., GAUSSIAN 03, Revision C.02, Gaussian Inc., Wallingford, CT, 2004.
- [6] R. C. Weast, et al., CRC Handbook of Chemistry and Physics, 66th edition, 1985, Chemical Rubber Company.

3. HYDROGEN PLASMA GENERATED WITH MICROWAVE

3.1 Background

Microwave has been applied as an alternative method for plasma generation due to the advantages which may not be realized by other methods. Microwaves are directly introduced into the plasma volume, and the system does not have any vulnerable parts and requires any maintenance [1]. The contamination of plasma by the evaporated materials can be prevented due to the electrodeless arrangement. Plasmas are generally generated under low gas pressure in order to have high plasma density, low gas temperature, and good uniformity. However, atmospheric pressure plasmas have recently attracted a lot of attentions because they eliminate expensive vacuum systems, which make a high processing capacity possible [2].

Atmospheric microwave plasma has been developed in several processing areas especially in surface modification [3] and thermal processing [4]. The unique characteristics such as high gas temperature and low plasma density limit its further usages in materials application. In order to generate plasma under such high pressure, huge microwave power has to be supplied which causes very low energy efficiency.

There are some experimental investigations on the effects of field concentrators on the plasma generation. Golubovskii and coworkers [5] have found that by putting BaTiO₃ pellets with sharp edges inside the discharge tube, the plasma under atmospheric pressure can be ignited. Another experiment was conducted by Al-Shamma'a et al [6]. They used a copper nozzle with conical tip for feeding nitrogen gas to concentrate the electromagnetic field under an atmospheric pressure. Both experiment and computer simulation results clearly demonstrated that the microwave field around the conical tip was intensively concentrated. Plasmas can be easier ignited at the tip of the concentrator.

In order to generate atmospheric plasma at low microwave power and gas temperature, concentrators could be a good approach. The general idea is that by inserting a concentrator which has a sharp edge or thin tip or tiny particles, the gases could be easily broke down around the concentrated sites. However, the concentrated sites usually are at extremely high temperatures, which cause local melting of the material and in turn failure of the concentrator. Materials with high melting temperature or delicate fabrication techniques have to be utilized to generate a better reliable concentrator which has a longer processing lifetime. High cost of such a concentrator would limit its further applications in plasma industry. Replaceable field concentrators could be a better solution. These kinds of concentrators have a relative shorter lifetime but could be replaced at a very low cost, which can reduce the operation cost and could be employed in big industry processing. The idea of this part is to test several replaceable concentrators in generation of plasma under microwave radiation, and study their effects.

3.2 Experimental

A schematic diagram of the experimental system is shown in Figure 3.1. The microwave chamber is a multimode resonant oven with up to 4 kW microwave power. A microwave transparent quartz tube was inserted at the middle of the chamber and extended outward. The out parts were wrapped with metallic tubes with flanges for microwave shielding. Tested gases including argon, nitrogen, hydrogen or the mixture were fed into the tub at one atmosphere pressure and different flow rates. Concentrators were put into a clay crucible, at the edge of which a K type shielded thermocouple was fixed and utilized to record the gas temperature. There is a hole at the top of the furnace, through which plasma images were recorded by the video camera. Each experiment was conducted by starting with the feeding gases for 15 minutes to purge all the air out and the whole tube was filled with testing gases.

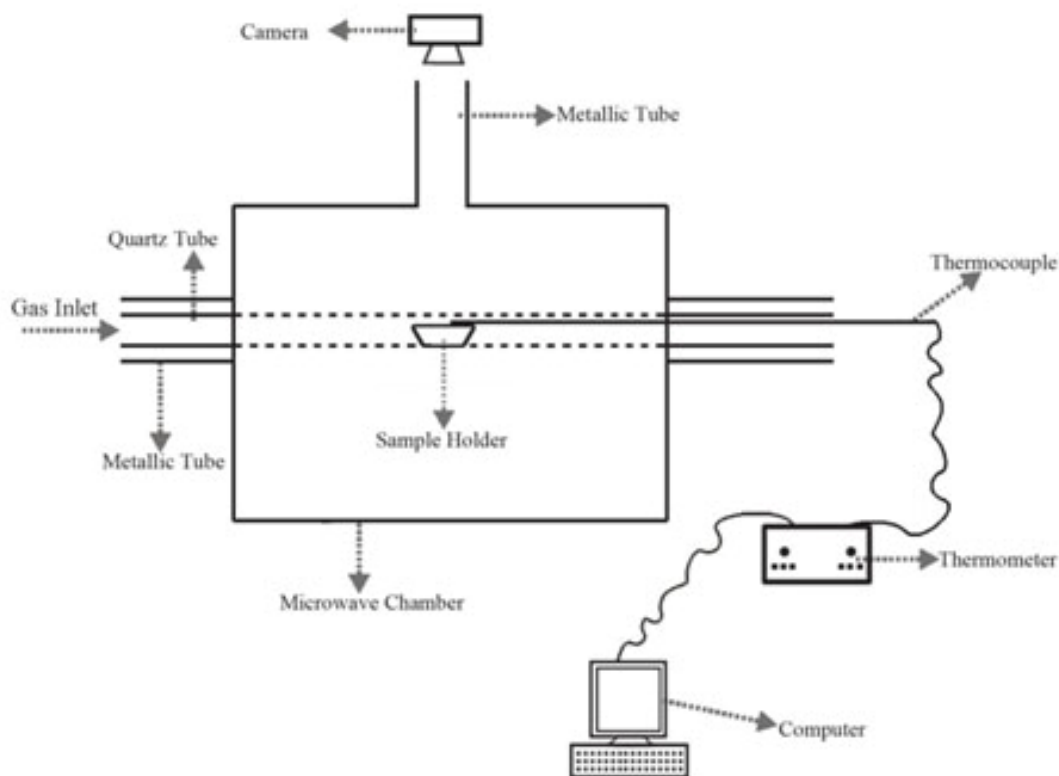


Figure 3.1. Schematic picture of experimental system

Tested field concentrators are summarized below:

- Iron pin $D=0.0645$ inch with tip $D=0.02$ inch (Figure 14 left)
- Cu wire $D=0.5$ mm (Figure 14 right)
- Cu powder <10 micron

- Fe powder <10 micron
- Al powder <35 micron
- Fe wire D=0.5 mm
- Graphite powder <35 micron

All these selected field concentrators are very cheap and could be easily fabricated in commercial scale.

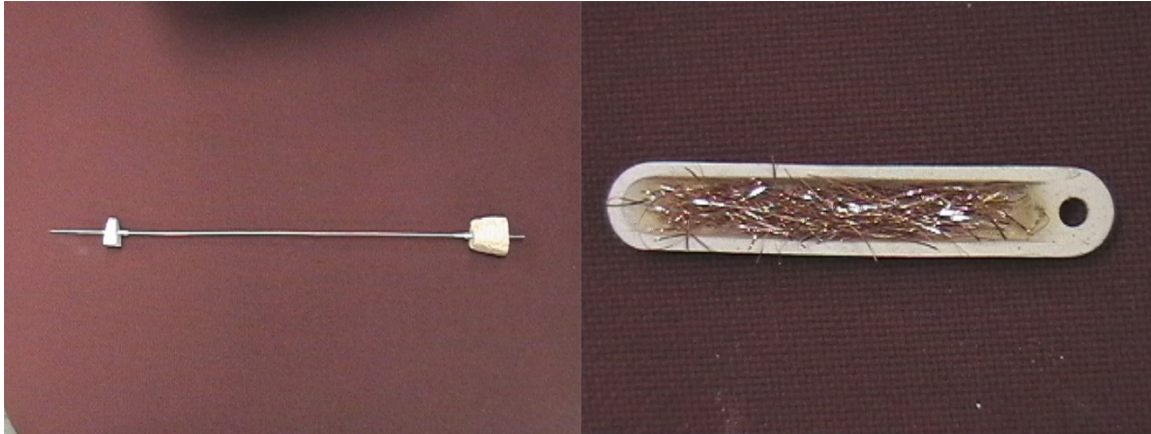


Figure 3.2. Selected field concentrators, iron pin (left) and copper wires (right)

3.3. Results and Discussion

Plasma observations were determined by the colorful scenes from the video camera. The results are shown in Table 3.1. Under such high flow 7000 ml/min, argon gas is very easy to be ionized, even with or without the concentrators, and the required energy could be as low as 1 kW power. As nitrogen and argon mixture was fed into the system, no plasma was produced without the presence of concentrators. Several concentrators could assist the plasma generation of 50% Ar and N₂ mixture. Powders showed better results. When nitrogen was increased into 75% of the total gases, more microwave power has to be supplied to initialize the plasma. Pure nitrogen gases could also be ionized with the assistance from the concentrators, with which powders worked better and required less energy. Hydrogen gases and mixtures were tested at low flow rate only 300 ml/min due to the extremely high temperature and exploration considerations. With no concentrators inside, even though there was 50% argon gas, no plasma was produced. However, with the presence of concentrators, such as graphite powder, plasma could be easily generated at 1 kW power. Pure hydrogen plasma could also be generated under minimum power when concentrators were used. Some typical plasma images are shown in Figure 3.3.

Table 3.1. Observed plasmas of using different concentrators (O-plasma, X-no plasma)

Concentrators	Ar (7000 ml/min)				Ar:N ₂ =1(total flow 7000 ml/min)				Ar:N ₂ =1:3(total flow 7000 ml/min)				N ₂ (7000 ml/min)				Ar:H ₂ =1(total flow 300 ml/min)				H ₂ (300 ml/min)							
	1k W	2k W	3k W	4k W	1k W	2k W	3k W	4k W	1k W	2k W	3k W	4k W	1k W	2k W	3k W	4k W	1k W	2k W	3k W	4k W	1k W	2k W	3k W	4k W	1k W	2k W	3k W	4k W
No	O	O	O	O	X	X	X	X											X	X								
Iron Pin	O	O	O	O	X	X	O	O	X	X	X	O																
Cu Wire					X	X	O	O	X	X	O	O			X	O	X	O	O	O	X	X	O	O				
Cu Powder						O	O	O								O			O	O		O	O	O				
Fe Powder						X	O	O						X	O	O												
Al Powder					X	O	O	O								O												
Fe Wire																		O	O	O								
Graphite Powder																	O	O	O	O	O	O	O	O				

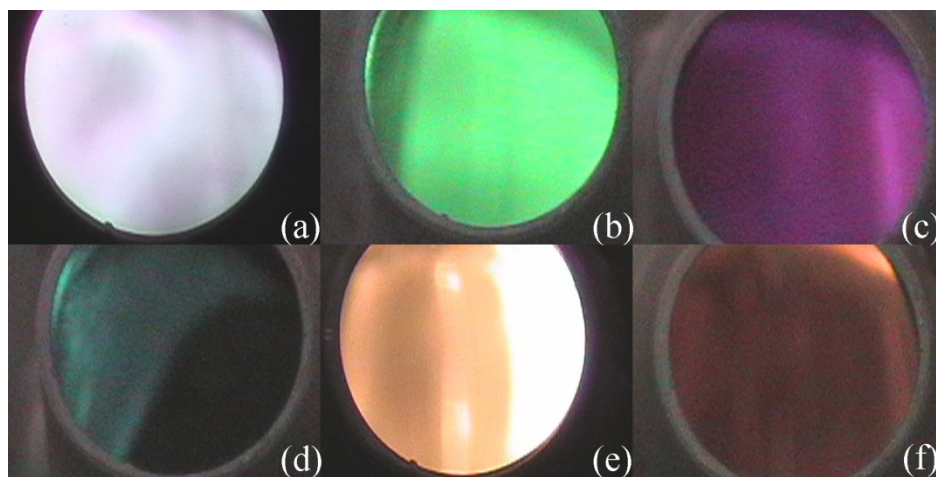


Figure 3.3. Typical plasma images, (a)Concentrator: Fe pin, 4 kW, Ar, 7000ml/min, (b)Concentrator: Cu powder, 4 kW, Ar:N₂=1, 7000 ml/min, (c) Concentrator: Cu wire, 4 kW, Ar:N₂=1:3, 7000 ml/min, (d) Concentrator: Cu powder, 4 kW, N₂, 7000 ml/min, (e)Concentrator: Fe wire, 4 kW, Ar:H₂=1, 300 ml/min, (f) Concentrator: Cu wire, 3 kW, H₂, 300 ml/min

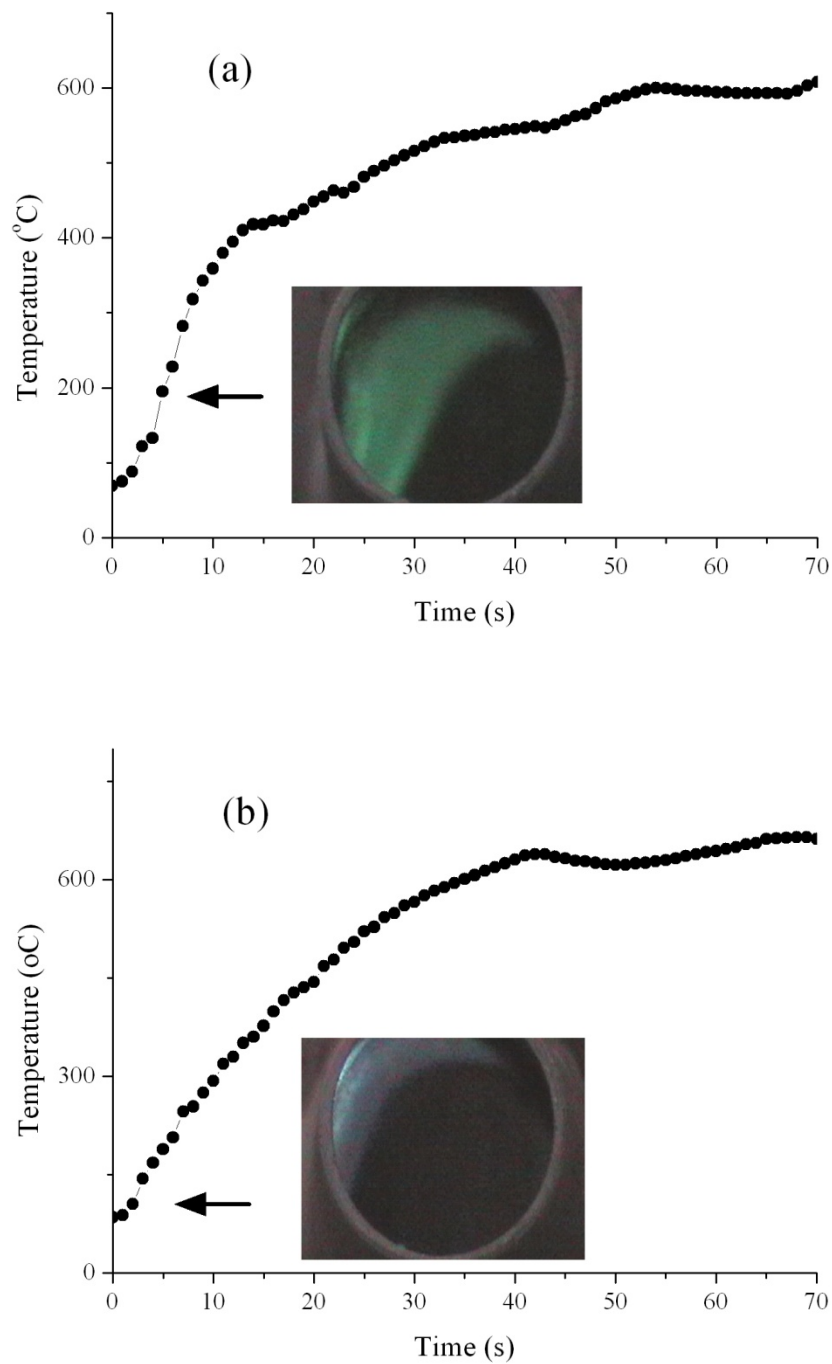


Figure 3.4. Gas temperature profiles at Ar/N₂=1, 3kW, concentrator: (a) Cu powder, (b) Fe powder

Plasma gas temperature is usually extremely high at atmospheric pressure. The reported gas temperature at a multimode microwave cavity was as high as 4000 K [7]. However, from our experimental observations, plasma could be initialized at every low gas temperature when

concentrators were utilized. As shown in Figure 3.4, temperature profiles presented that plasma began to occur at only 200 °C and 100 °C when copper and iron powders were used as concentrators, respectively. The gas temperature continued to rise until it became relatively stable. The final temperature was several folds less than the reported value. It indicates that with the help of concentrators, the gas temperature could be lowered tremendously. The high temperature associated problems such as local melting, and overheating could be prevented.

However, in generation of hydrogen plasma, when the plasma was initiated, the gas temperature quickly jumped to the upper detection limit of thermocouple (>1200 °C). As shown in Figure 3.5, there was a latent period before the plasma began to appear, where the gas temperature rose slowly. As soon as the plasma came out, the temperature soared to 1200 °C in 6 seconds, and it didn't seem to become stable. No concentrator was found to be able to stabilize the hydrogen plasma. However, we have found out that this can be improved by controlling the microwave power. Sustainable hydrogen plasma could be generated by using higher microwave power to initiate and lower power to maintain. Figure 3.6 shows an example of sustainable hydrogen plasma generated at changing power. Plasma was initially ignited at higher power level 2 kW, and the gas temperature immediately jumped to nearly 1000 °C. As soon as the power switched to 1.5 kW, the gas temperature was sustained below 1000 °C for a long period of time. Also from the plasma images, the intensity and shape of the plasma did not change, indicating the sustainable plasmas.

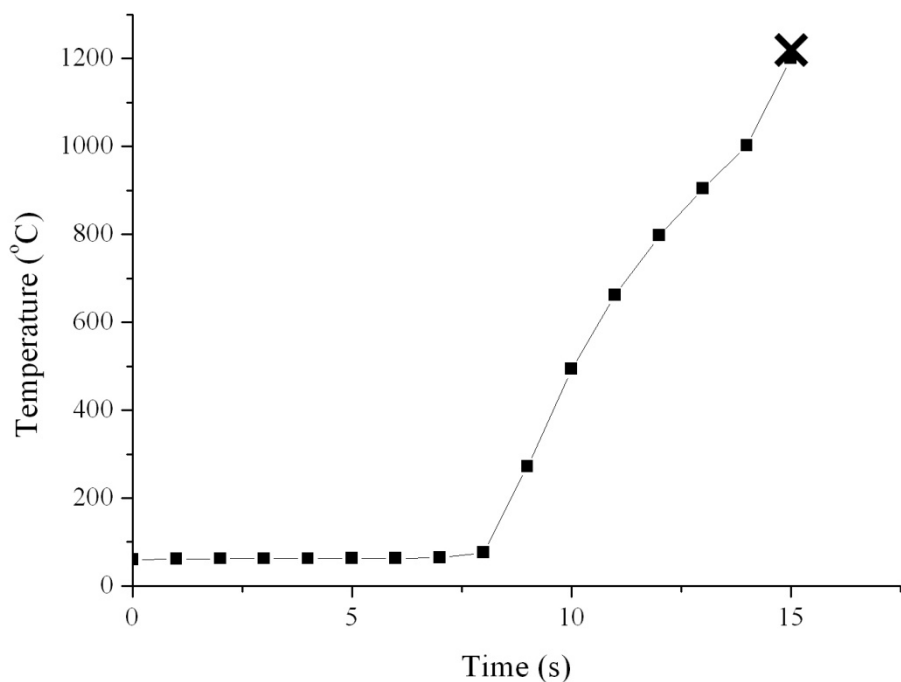


Figure 3.5. Gas temperature at 2kW, H₂ 300 ml/min, concentrator: Cu powder

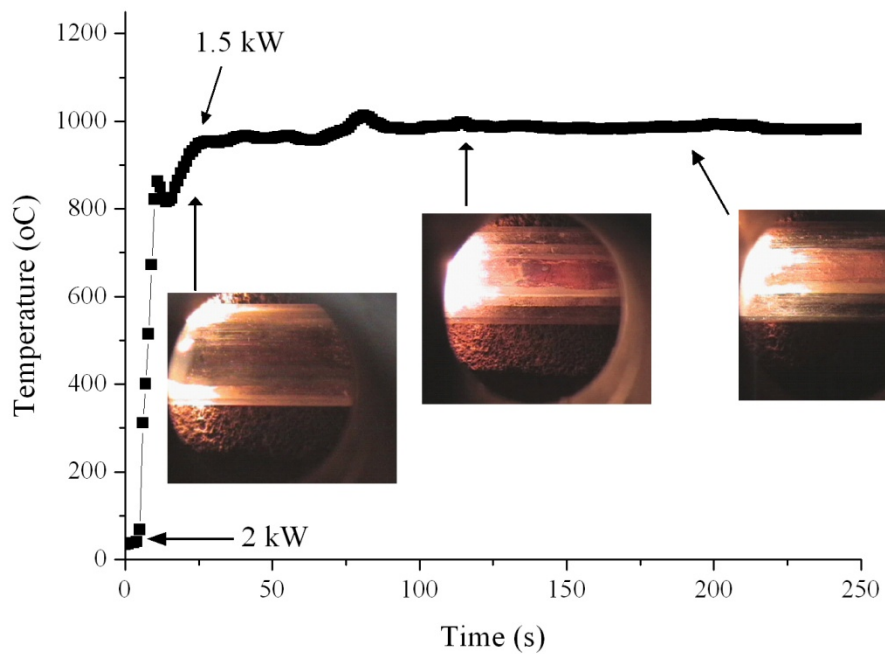


Figure 3.6. Plasma images and gas temperature at H_2 300ml/min, concentrator: Cu powder, 2kW to initiate and 1.5 kW to maintain

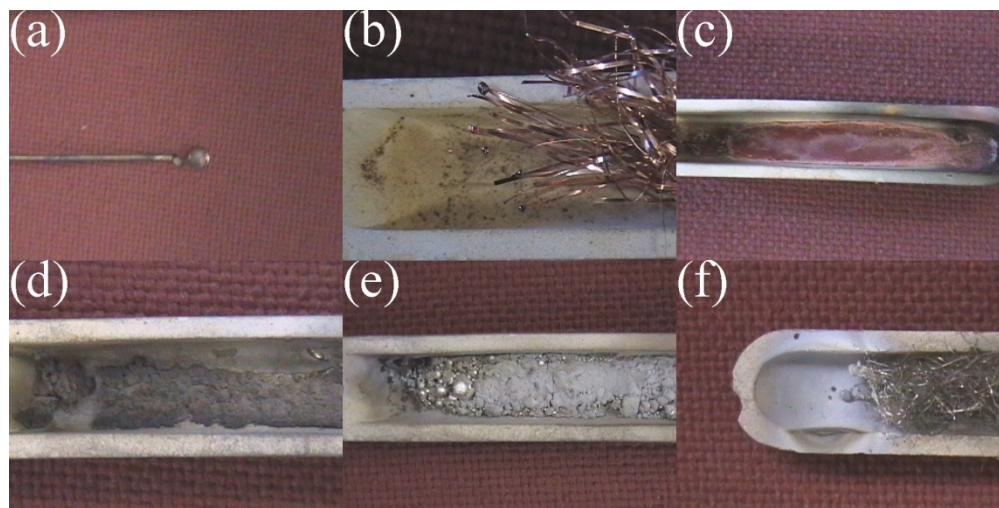


Figure 3.7. Failed concentrators, (a) Iron pin after 17 cycles, (b) Cu wire after 6 cycles, (c) Cu powder after 4 cycles, (d) Iron powder after 10 cycles, (e) Al powder after 7 cycles, (f) Fe wire after 7 cycles

Although these concentrators showed great capabilities in assisting plasma generation, most concentrators failed after several generation cycles due to melting or sintering. Some failed concentrators after experiments are shown in Figure 3.7. In order to continue assisting plasma generation, these concentrators should be replaced. However, replacing such concentrators is cheap and feasible. No contamination from the materials of the concentrators was observed since there was no significant weight loss of concentrators before and after experiment. Also no compounds were formed.

3.4. Conclusion

Several field concentrators including pin, wires, and powders have been tested to assist the plasma generation under atmospheric pressure. With the presence of these concentrators, microwave field could be enhanced and gases could be ionized at low power which cannot be realized without field concentrators. Gas mixtures and pure gases all exhibited better ionization ability. Relative low energy was required to generate plasma and the associated gas temperature was much lower. Sustainable plasma was observed in both nitrogen gas and gas mixtures. Stable hydrogen plasma could be maintained by microwave power control. Although concentrators have a limited lifetime and need to be replaced after several generation cycles, the cost for such replacement is insignificant. Application of such field concentrators in plasma industries has great feasibility and possible potentials. Hydrogen plasma or hydrogen ions could be easily generated and controlled by using this technology, which made the first step to form hydrogen clusters.

3.5. Section 3 References

- [1] M. Mozjetchkov, T. Takanashi, Y. Oka, K. Tsumori, M. Osakabe, O. Kaneko, Y. Takeiri, and T. Kuroda, *Review of Scientific Instruments*, 69 (1998) 971-973, "Microwave plasma source for the negative hydrogen ion production".
- [2] J. Park, I. Henins, H. W. Herrmann, G. S. Selwyn, J. Y. Jeong, R. F. Hicks, D. Shim and C. S. Chang, *Applied Physics Letters*, 76 (2000) 288-290, "An atmospheric pressure plasma source".
- [3] L. Lianos, D. Parrat, H. Q. Tran, and D. M. Tran, *Journal of Vacuum Science & Technology, A: Vacuum, Surfaces, and Films*, 12 (1994) 2491-2498, "Secondary ion mass spectrometry time of flight and in situ x-ray photoelectron spectroscopy studies of polymer surface modifications by a remote oxygen plasma treatment".
- [4] S. R. Wylie, A. I. Al-Shamma'a, J. Lucas, and R. A. Stuart, *Journal of Materials Processing Technology*, 153-154 (2004) 288-293, "An atmospheric microwave plasma jet for ceramic material processing".

- [5] Y. B. Golubovskii, R. V. Kozakov, V. A. Maiorov, A. V. Meshchanov, I. A. Porokhova, and A. Rousseau, *Journal of Physics D: Applied Physics*, 37 (2004) 868-874, “Dynamics of gas heating in a pulsed microwave nitrogen discharge at intermediate pressures”.
- [6] A. I. Al-Shamma'a, S. R. Wylie, J. Lucas and C. F. Pau, *Journal of Physics D: Applied Physics*, 34 (2001) 2734-2741, “Design and construction of a 2.45 GHz waveguide-based microwave plasma jet at atmospheric pressure for material processing”.
- [7] M. J. Shenton and G. C. Stevens, *IEEE Transactions on Plasma Science*, 30 (2002) 184-185, “Optical emission from atmospheric pressure nonequilibrium plasma”.

4. SALT IMPREGNATED ACTIVATED CARBON FOR HYDROGEN STORAGE

4.1 Introduction

The previous calculations have been performed under the assumption of a single molecule, however, such an assumption cannot stand in a real case unless it is in a super rarefied gas phase. In order to better understand and prove the idea that the electrostatic force could assist the adsorption interaction, real experimental work and combined computational work are needed.

Alkaline salts such as chlorides or bromides are ionic compounds where the ability of attracting hydrogen by electrostatic forces can exist on the surface of such substances. However, these salts usually have small surface area which means that the adsorption sites are limited. The overall adsorption capacity is negligible and the difference between each compound is not easily identified. Activated carbon has been widely used in adsorption of pollution in gaseous or liquid phases, storage of gas, catalyst support, and also double layer supercapacitors [1-4]. The use of activated carbon for hydrogen storage is mainly depending on its total porosity [5]. The weak interaction force (usually physisorption) prevents the activated carbon to be used as good hydrogen storage materials since significant adsorption can only occur at cryogenic temperature (77K). The extremely large surface area of activated carbon makes it an excellent adsorbent of chemicals. Here, activated carbon was used as a substrate where the ionic compounds were adsorbed onto the surface. The enhancement of hydrogen storage from the adsorbed ionic compounds on carbon could be differentiated from that of the plain carbon. Moreover, detailed information about the electrostatic force enhanced adsorption could be obtained by impregnating various ionic compounds composed of different cations and anions.

The theoretical calculations on the interaction of small molecules with bulk crystal surface often fail to correctly describe the crystal structure, bonding energy, and optimized geometry [6]. There is large discrepancy between experimental and theoretical data. Periodic ab initio is often employed in crystal calculations and is believed to match well with experimental results. However, such method is time consuming and sometimes works poorly in adsorption studies, as described by Damin [7] in their periodic study of CO adsorption on MgO surface. The calculated result is underestimated in comparison to the experimental data. The use of the cluster model to describe the adsorption with crystal surfaces is proved by the fact that there are only limited atoms which are involved in the adsorption. Early on, the cluster calculations were carried on bulk clusters where there are no surrounding charges. The accuracy depends on the size of the chosen cluster and there are reported examples that such “bare” cluster calculations yield problems in overestimating band gap [8] and inaccurate lattice parameter [9]. The Madelung potential could be compensated by embedding the cluster into an array of point charges and the calculation accuracy could be enhanced. The magnitude of point charge is not necessary to be the nominal charge, because by using nominal charge, the Madelung potential of the crystal is often overestimated [10]. In general, the point charge is to reproduce the chemical environment and

background for the cluster in simulating the bulk lattice, whereas it is not involved in direct chemical bonding. The criteria for determining the value of point charge requires the cluster to be self-consistent whether in charge consistency or bond length consistency. The value of point charge depends strongly on the cluster size. The charge value decreases as the cluster size becomes larger in order to satisfy the consistency criteria [6, 10]. Charge consistency requires that the input array of point charge results in the cluster having the same magnitude of charges as the input value, while bond length consistency requires that the value of the surrounding charges can reproduce the bulk crystal lattice parameter. Kadossov and coworkers [6] studied the correlation between the electronic properties of the NiO clusters with the magnitude of the surrounding point charges, and obtained reasonable value compared with experimental and calculated data by choosing charge value empirically to reproduce the Ni-O bond length. Here, a similar method is used for obtaining the right surrounding point charge, which can best describe the correct lattice parameter of the cluster. Then the system composed of hydrogen molecule and embedded cluster is optimized to obtain the final geometry and corresponding bonding energy.

The theoretical results combined with experimental approach reveal well the charge induced enhancement of the deposited ionic salts on the adsorption of hydrogen molecules.

4.2 Experimental

4.2.1 Preparation of samples

The salt impregnated carbon samples were prepared via impregnating 1.2 grams of activated carbon Norit A (acquired from Norit Americas Inc.) with 60 ml salt solutions under magnetic stirring for 24 hours at room temperature. The products were filtered and then dried at 120°C overnight.

4.2.2 Characterization

The surface area and the pore size distribution were measured by using a Micromeritics ASAP2000 instrument. The samples were evacuated by heating at 300 °C under vacuum for 12 hours before testing. The tubing containing degassed samples were then sealed and carefully transferred to a balance to obtain the sample weight.

A Hitachi S-4700 field emission-scanning electron microscopy (FE-SEM) was used to examine the microstructure of the samples.

The accurate weight percentage of salt impregnated on activated carbon was determined by Inductively Coupled Plasma Emission Spectrophotometer (ICP). Before analysis, the solutions

were prepared by flushing the samples several times using 10% hydrochloride acid and distill water. The cation concentration analyzed by ICP was used to calculate the total salt weight by assuming that the positive and negative ions adsorbed on carbon follow the charge stoichiometry.

4.2.3 Hydrogen adsorption measurements

Hydrogen adsorption at pressure between 0.1 bar and 80 bar was measured by using static volumetric techniques with an automatic Sieverts' apparatus (PCT-Pro 2000 from Hy-Energy LLC) at both room temperature and 77k. The simple schematic diagram of Sieverts' apparatus and principle of volumetric measurement could be found elsewhere [11]. Figure 4.1 and 4.2 show the outlook of the instrument and the operating screen of the control software. The samples were extensively evacuated for 12 hours at 300°C and transferred with care to the PCT sample holder. Further degas of samples was performed in PCT apparatus at 150 °C for 3 hours to remove any contaminations during the transfers. Around 600 mg of samples were used in each test, and ultra pure (99.999%) hydrogen and helium gases were used for all calibrations and measurements.



Figure 4.1. View of the PCT-Pro 2000 instrument

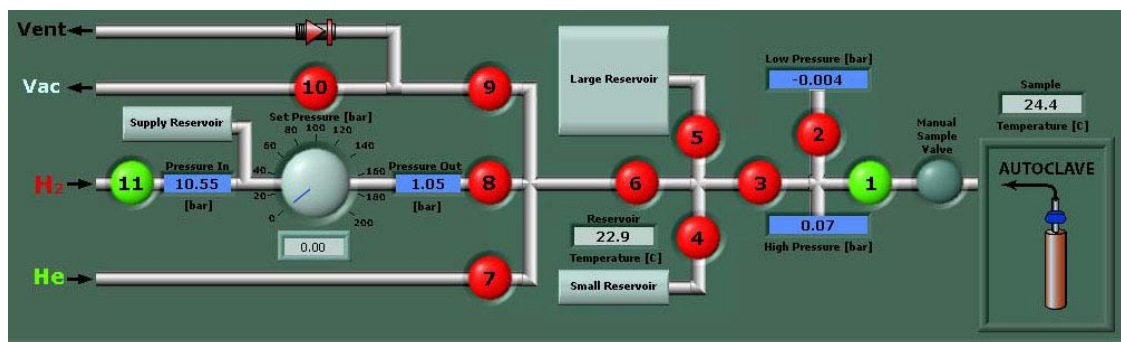
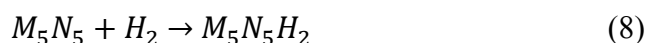


Figure 4.2. Operating screen of the PCT-Pro 2000 software

4.2.4 Computational method

The salts with only cubic structures were calculated. The clusters used here have been chosen to satisfy the criteria of being neutral, and stoichiometric. The salt solids were represented by various M_5N_5 clusters, where M indicates the cation and N indicates the anion. The clusters were embedded in an alternating positive and negative point charge of equal value. The point charge arrays were arranged at a construction of $13 \times 13 \times 13$ system. All the bonds, angles, and crystal data (CIF files) of salt crystals were obtained from an online crystallography database [12]. Geometry optimization of clusters was first performed at different values of surrounding point charges by varying the bond length of the lattice parameter while fixing all the bond angles so as to obtain the correct magnitude of point charge. The criteria used here is that the magnitude of point charges were varied until the optimized lattice parameter could well reproduce the number from the standard database.

After obtaining the correct point charge value, the point charge array was moved down along the z-axis to expose the surface atoms with the charge magnitude and structure unchanged, as shown in the schematic diagram of Figure 4.3. For modeling of hydrogen adsorption, the salt clusters were fixed at the initial structure while the hydrogen molecules were free to move. The total binding energy was calculated by the difference between the total energy of the whole adsorption system and the total energy of the separate reactants before combination, as presented in following equation:



All the calculations were performed by using DFT/B3LYP method and a basis set of 6-31 G(d) in GAUSSIAN 03 program.

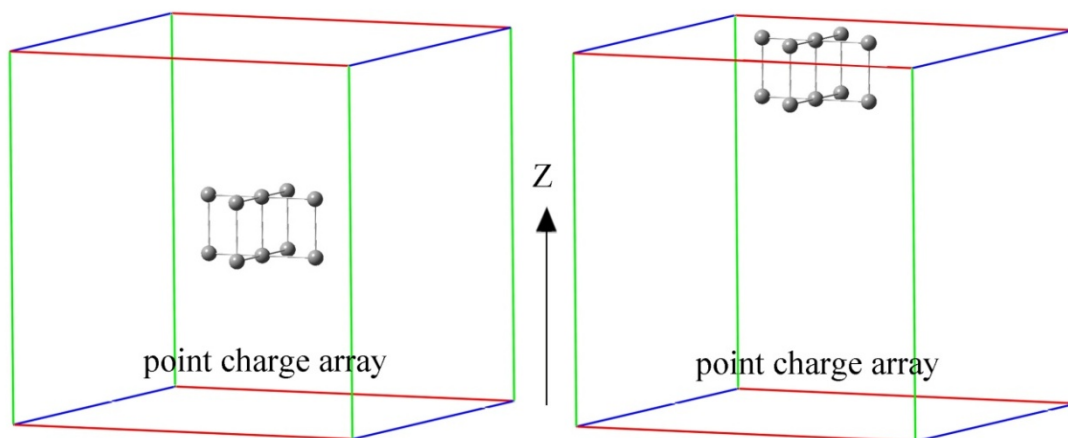


Figure 4.3. Point charge array for cluster simulation

4.3 Results and Discussion

4.3.1 Raw activated carbon

Table 4.1 contains the BET characterization of all the samples studied. AC indicates the Norit A activated carbon. Second part identifies the solution concentration and salt type used for impregnation. The raw carbon has a BET surface area of 1836 m²/g and micropore volume of 0.25cc/g.

Table 4.1. BET analysis of raw carbon and salt impregnated carbon

Sample	BET surface area (m ² /g)	Micropore volume (cc/g)	Average pore diameter (Å)
AC	1836.15	0.25	21.78
AC+1MLiCl	1702.37	0.23	21.75
AC+1MNaCl	1652.44	0.23	21.94
AC+1MKCl	1559.38	0.21	21.93
AC+1MKBr	1398.90	0.20	21.95
AC+1MNiCl ₂	1377.26	0.16	21.99

As summarized in a recent study [5], hydrogen adsorption capacity of carbon materials only depends on the total porosity of the materials, not on the pore structure. The small micropore volume of this carbon barely affects the total hydrogen storage capacity. As shown in Figure 4.4,

the total hydrogen storage capacity of Norit A carbon reaches 0.45 wt% at the pressure of 80 bars at room temperature and the trend is almost a linear line. This indicates that the weak interaction requires higher pressure to obtain the significant storage [6]. At 77K, the capacity reaches the saturation point of 3.38 wt% at around 60 bars. All the adsorption data of this type of carbon are in good agreement with the published results [5], although Norit A carbon has smaller micropore volume. This again proves that the hydrogen adsorption ability of activated carbon depends only on the total surface area with no relevance to the pore structures.

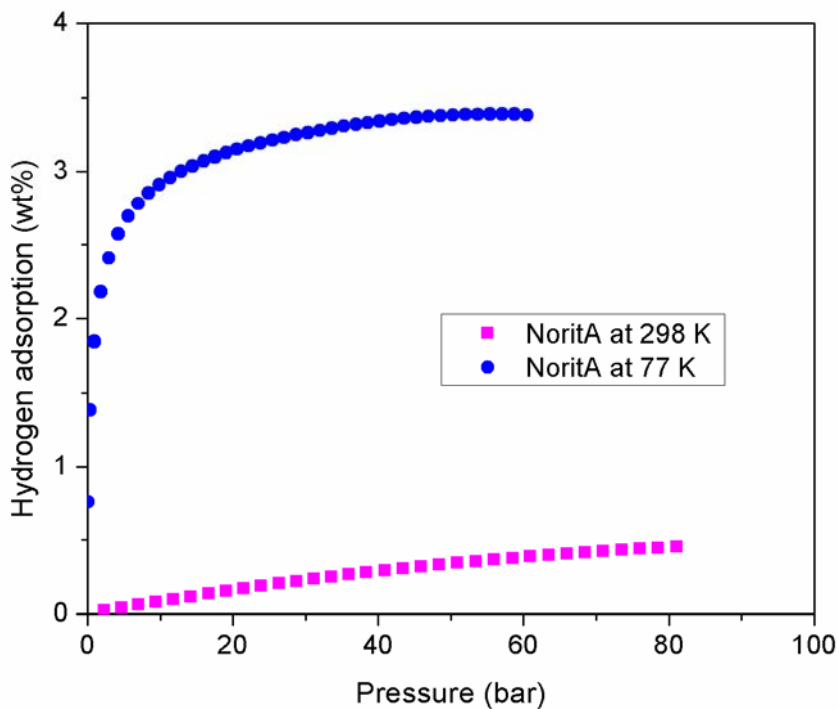


Figure 4.4. Hydrogen adsorption of activated carbon at 298 K and 77 K

4.3.2 Salt impregnated carbon

1M of salt solutions including LiCl, NaCl, KCl, KBr, and NiCl₂ were used as impregnation agents. The surface areas of treated samples are shown in Table 4.1. Obviously, the BET surface areas dropped significantly in comparison with the untreated sample. Among those, the NiCl₂ treated sample was most affected and the total surface area reduced about 30%. The micropore volume was also affected to some extent, however, the average pore diameter increased. The surface properties obtained by BET method were calculated as surface area per gram of sample. The salts adsorbed on carbon account for significant weight, which can cause underestimation of the calculation.

Table 4.2 shows the mole percentage and weight percentage of the cation and accordingly the salt of the treated samples. Except for LiCl, all other salts showed similar mole ratio, which refers to the similar dispersion on the carbon surface. Due to the differences in molecule weight, the weight percentage varied accordingly. The surface area should be adjusted based on the salt weight in order to obtain the true total surface. As shown in Table 4.3, the adjusted surface area of samples are still significantly smaller than the plain carbon, which indicates the blocking of the pores on the original carbon due to the crystallization of the impregnated salts.

Table 4.2. Concentration of the impregnated salts

Sample	AC-1MLiCl	AC-1MNaCl	AC-1MKCl	AC-1MKBr	AC-1MNiCl ₂
Cation (wt %)	0.40	2.00	3.76	3.05	5.14
Cation (mole%)	0.058	0.087	0.096	0.078	0.088
Salt (wt %)	2.45	5.10	7.19	9.30	11.36

Table 4.3. Adjusted surface area based on the salt concentration

Sample	AC	AC-1MLiCl	AC-1MNaCl	AC-1MKCl	AC-1MKBr	AC-1MNiCl ₂
Adjusted surface area (m²/g)	1836.15	1745.17	1741.17	1680.12	1542.39	1553.79

It is noted that the electrostatic force is supposed to increase the interaction so that the hydrogen adsorption in room temperature could be increased. However, every salt tested is heavier than carbon materials so that the magnitude of the total hydrogen capacity of salt impregnated carbon in weight percentage is not supposed to suppress the plain carbon. Therefore, the adsorption capacity in weight percent should be adjusted to the adsorbed hydrogen weight divided by the total carbon weight which equals to the total sample weight minus the weight of salt. Such calculation could minimize the effects from differences in molecule weight of salts. Figure 4.5 shows the hydrogen adsorption of salt impregnated samples as a function of pressure. The inserted figure pointed out that KBr and NiCl₂ impregnated carbon have better adsorption than plain carbon at pressure lower than 10 bars. NaCl and KCl samples are in close value with original carbon and LiCl samples being lower. As the pressure increased, the surface area plays a more important role in adsorption so that only the NiCl₂ sample showed better improvement while others were significantly lower.

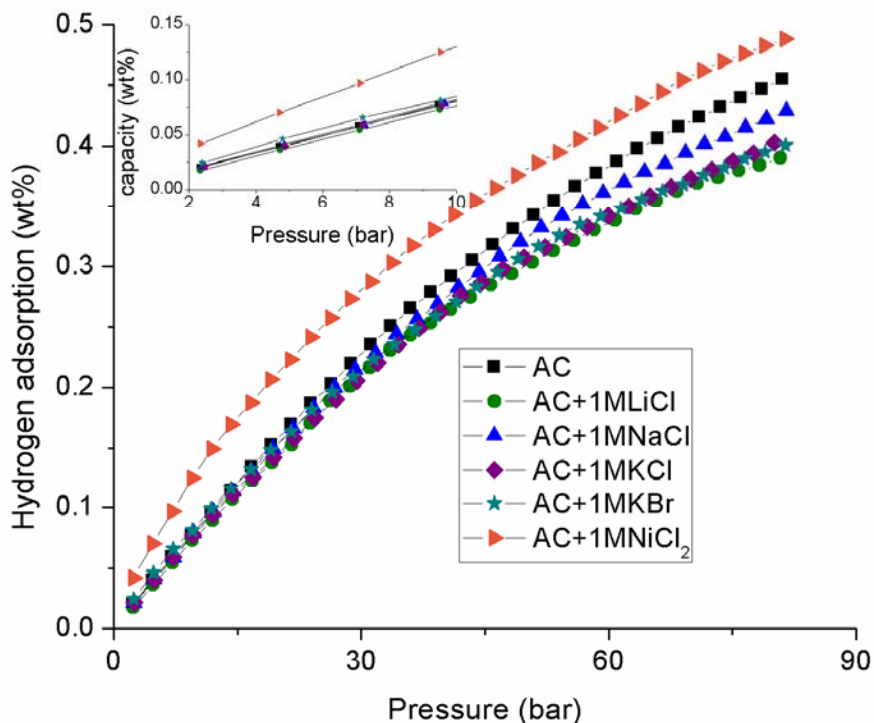


Figure 4.5. Hydrogen adsorption of salt impregnated carbon at 298 K

It should be noted from Table 4.3 that the surface areas of samples are significantly affected by the impregnated salts, therefore a profile of weight of adsorbed hydrogen (g) divided by the total surface (m^2) could give a more obvious picture of the effects from salt impregnations.

Figure 40 shows the hydrogen adsorption on impregnated carbons in weight per square meter, which describes how each surface compound contributes to the total adsorption. With respect to the original carbon, LiCl impregnated samples show smaller capacity although the difference is quite insignificant. NaCl and KCl are nearly overlapped with plain carbon indicating that coating these salts on carbon made no difference on adsorption, which also demonstrated that the adsorption energy was in close value to that of carbon. Samples with KBr showed significant enhancement indicating a stronger interaction. The increase of the NiCl_2 sample was so remarkable that nearly 30% enhancement could be achieved. As discussed in the previous chapter, the transition metal ions have unfilled d orbital whereas the donation from d electrons to hydrogen anti-bonding orbital and back-donation from hydrogen electrons to metal ion are significant. Thereby unlike alkaline salts, transition metal compounds exhibited stronger interaction in addition to the electrostatic force.

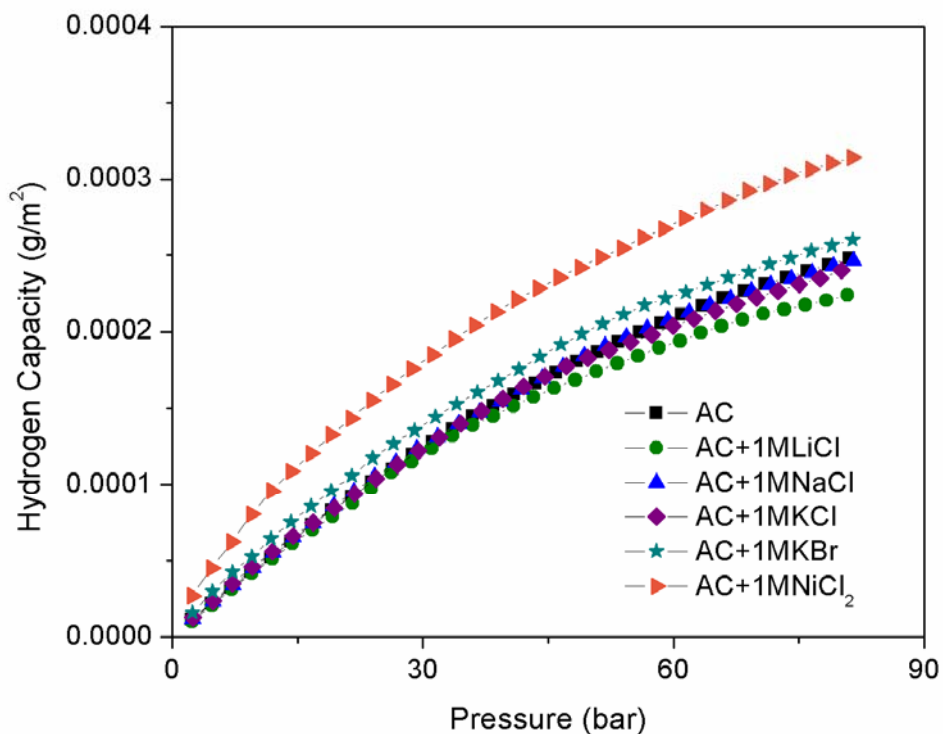


Figure 4.6. Hydrogen capacity per surface area of salt impregnated carbon

4.3.3 Computational results

4.3.3.1 Cluster optimization

The salt clusters of LiCl, NaCl, KCl, and KBr in point charges were first optimized to obtain the correct value of point charge which can well represent the crystal lattice parameters. Figure 4.7 shows the optimized structure and Table 4.4 summarizes the obtained parameters. The lattice parameter a (Å) is the cation and anion bond length which is also equal to half of length of the unit cell. The magnitude of the surrounding point charge Q_p is much smaller than the natural charge of the salts. And with Q_p equals 0 or 1, the lattice parameter was in poor agreement with the experimental value.

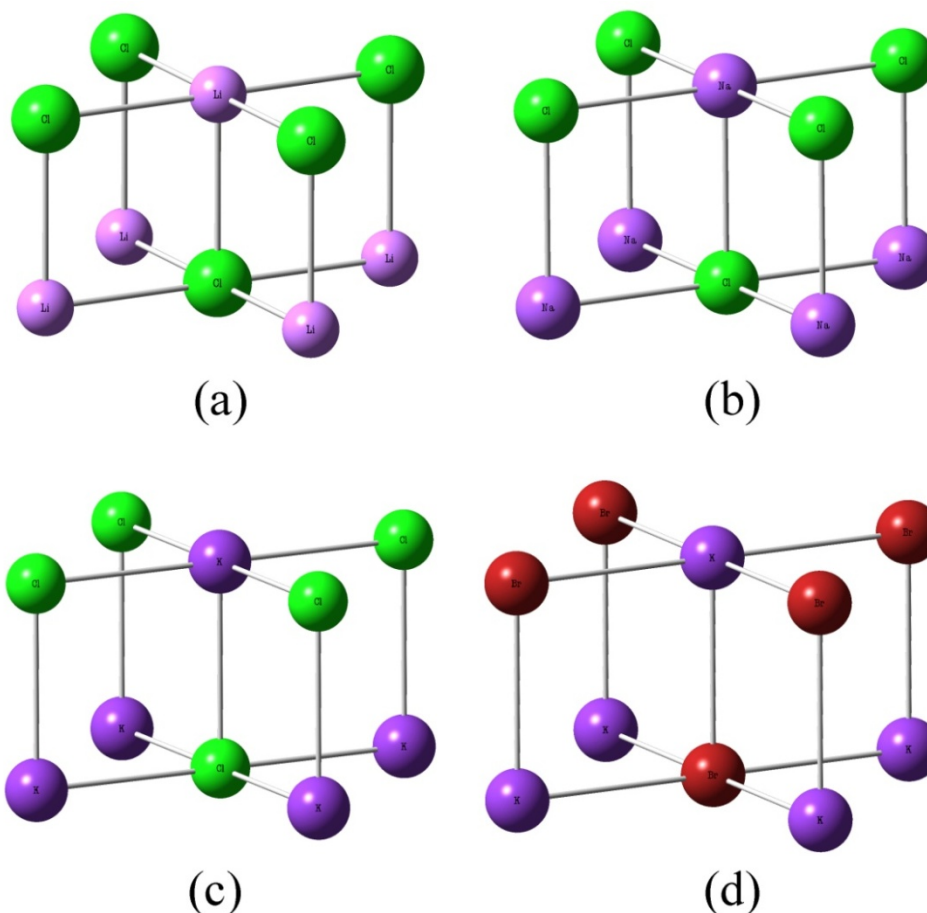


Figure 4.7. Optimized clusters in point charge

As the cation changed from lithium to potassium, the value of point charge decreased from 0.461 to 0.302, while the average Mulliken charge increased. Contradictory results were observed as the anion changes from chloride to bromide in which the point charge value increased and the Mulliken charge increased. These obtained point charges were used as the background for all the sequential hydrogen adsorption calculations.

Table 4.4. Optimized cluster parameters, where a is the lattice parameter, Q_p is the value of the surrounding point charge and Q_M is the average Mulliken charges

Cluster	a (Å)	Q_p	Q_M
Li_5Cl_5	2.565	0.461	0.61
Na_5Cl_5	2.820	0.421	0.68
K_5Cl_5	3.144	0.302	0.75
K_5Br_5	3.292	0.478	0.68

4.3.3.2 Hydrogen adsorption on first group halides

The surface atoms of the crystals have unbalanced dangling bonds which are responsible for strong surface adsorption ability. Moreover, in ionic crystals, the unsaturated bond means unbalanced charges; therefore the interaction with hydrogen molecules is stronger due to the electrostatic forces. As shown in Figure 4.8 that the surfaces of all the first group halides have the ability to absorb hydrogen molecules either on the cation site or the anion site. It follows side on adsorption (Yeager model) at the cation site and end on adsorption (Pauling model) on the anion site [13]. The free hydrogen molecules optimized by the same DFT method and basis set 6-31 G(d) had a bond distance of H-H at 0.74279 Å. For LiCl, the hydrogen molecule on the Li site was slightly elongated 0.00048 Å. The charge on Li accounted for the small electrostatic attraction and the electron cloud of the hydrogen sigma bond was weakly perturbed, which was demonstrated by the resulting positive charges on adsorbed hydrogen. On the Cl site, the end on adsorption attracted by the negative charged chloride ion caused an intrinsic dipole in the hydrogen molecule, as in Figure 42(b) that hydrogen 1 had a charge of 0.002 while hydrogen 2 had charge of 0.007. The interaction on the Cl site was a little stronger since the distance of the H-H bond was elongated 0.00126 Å. Figure 4.8(c) and 4.8(d) show the similar optimized arrangement for NaCl. However, the H-H perturbation was larger due to the more positively charged sodium 0.450 and more negative charged chloride -0.594. Better adsorption was achieved in KCl, where higher charged potassium (0.599) and chloride (-0.749) contributed to the stronger electrostatic force. The hydrogen intrinsic dipole on chloride site was promising strong, whereas the hydrogen 1 atom showed a negative charge -0.001 which indicated a vigorous force impacting on the electrons of the hydrogen molecule. By changing the anion from chloride to bromide, the potassium was less positively charged showing a number of 0.300, so did the bromide ion showing a number of -0.637. However, the H-H distance was larger, with 0.74381 on the potassium site and 0.74558 on the bromide site.

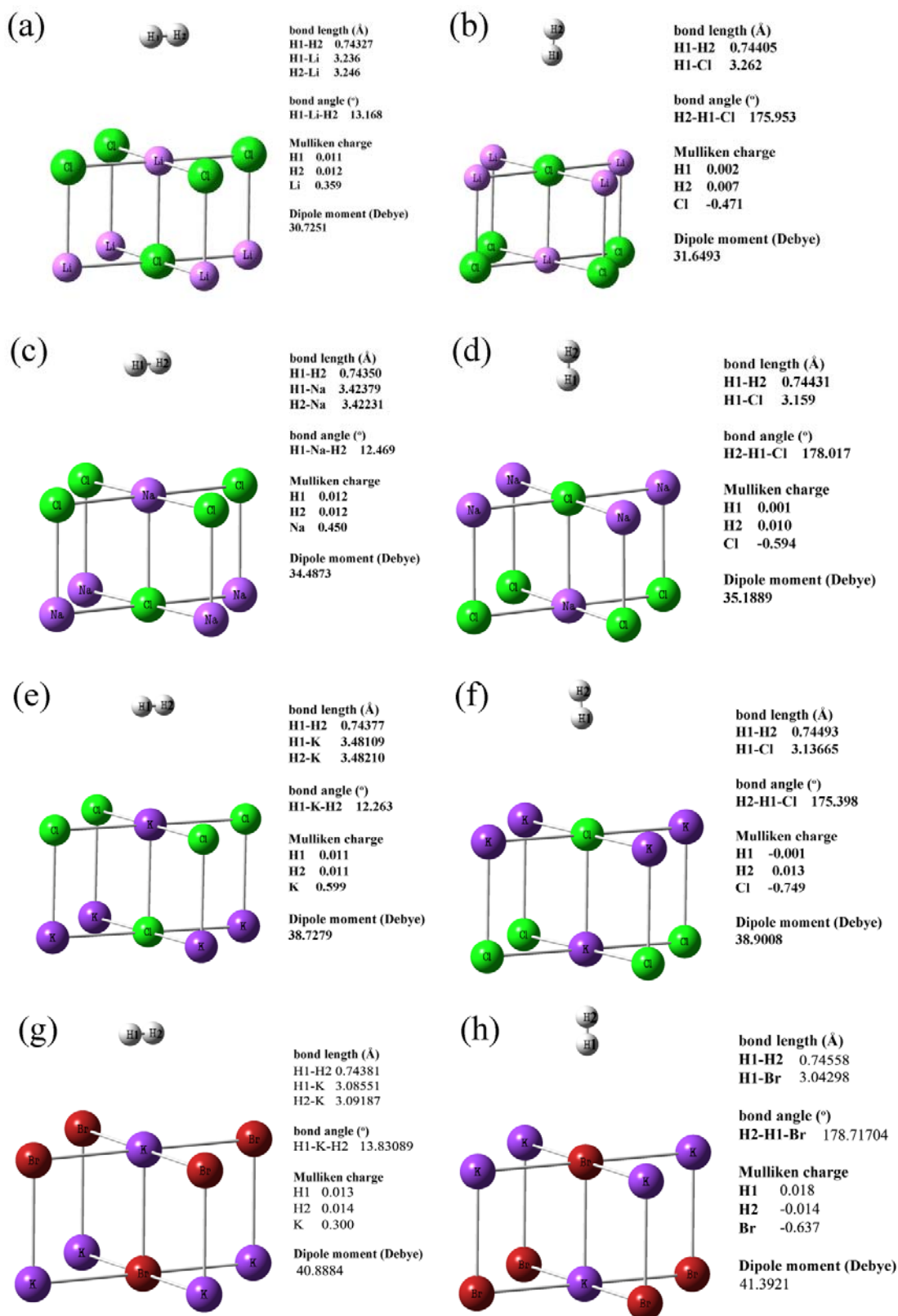


Figure 4.8. Optimized geometry of H₂ adsorbed on LiCl Li site (a) and Cl site (b), NaCl Na site (c) and Cl site (d), KCl K site (e) and Cl (f) site, KBr K site (g) and Br site (h)

A more detailed comparison is summarized in Table 4.5. Clearly, the trend is obvious that by keeping the chloride ion unchanged, increasing of cation radii from Li to K increased the adsorption energy and about 1.36 kJ/mole could be achieved on potassium of potassium chloride. The adsorption energy was consistent of the perturbation of H-H bond length which enlarged as the cation became larger. From the Mulliken charge analysis and the dipole moment of the cluster, it is obvious that the adsorption energy was enhanced as the charge and dipole moment increased. Therefore, the interaction was verified to be caused by electrostatic force. However, these results are contradictory with those obtained by calculating hydrogen interaction with isolated cation. Bushnell and coworkers [14] reported that the hydrogen adsorption energy on Na^+ is stronger than that on K^+ . It is pointed out that in their system, the cation is isolated, whereas the hydrogen molecule could be arranged in the 3-D space around the center ion. However, after introducing the anion, the positive charge was partially compensated and now the only space available for attaching hydrogen was the surface, whereby the dominating factor in compounds was that the dipole moment which was determined by both the cation and anion. It is also noted that the anion in the chloride compounds yielded better interaction with hydrogen by end on adsorption mechanism. The adsorption energy was nearly doubled by comparison with the cation in the same compound. This was attributing to the larger ionic charge magnitude and the stronger dipole moment, as summarized in the Figure 42. The same story was observed in KBr , where the adsorption energy was much stronger: 5.307 kJ/mole for K and 3.98 kJ/mole for Br. The large dipole moment accounted for the strong interaction energy.

Table 4.5. The optimized hydrogen bond length $r_{\text{H-H}}(\text{\AA})$, Mulliken charge Q_{M} , adsorption energy E_{ad} (kJ/mole), and dipole moment D (debye) of hydrogen adsorption on cluster surface

Adsorption site	$r_{\text{H-H}}(\text{\AA})$	Q_{M}	E_{ad} (kJ/mole)	D (debye)
Li of LiCl	0.74327	0.359	0.57948	30.7251
Cl of LiCl	0.74405	-0.471	1.16394	31.6493
Na of NaCl	0.74350	0.450	0.94737	34.4873
Cl of NaCl	0.74431	-0.594	1.73851	35.1889
K of KCl	0.74377	0.599	1.36453	38.7279
Cl of KCl	0.74493	-0.749	2.02167	38.9008
K of KBr	0.74381	0.300	5.30696	40.8884
Br of KBr	0.74558	-0.637	3.98134	41.3921

4.3.4 Comparison of experimental and computational results

The experimental data showed that the trend of salt impregnated samples followed the order of $\text{NiCl}_2 > \text{KBr} > \text{KCl} > \text{NaCl} > \text{LiCl}$, whereas the computational work of hydrogen adsorption on pure alkaline salts in terms of adsorption energy followed the same trend. Clearly, the computational results were in good agreement with the experimental data. It has been reported that the enthalpies for hydrogen adsorption on activated carbon are in the range of 3-6 kJ/mole [15-17]. From the above calculations, LiCl had the lowest adsorption energy which was smaller than 3 kJ/mole so that the adsorption capacity from experiment was below that of plain carbon. By comparing NaCl and KCl impregnated samples with original carbon, the adsorption energy was in close value around 3 kJ/mole whereas experimentally, the three adsorption curves almost overlapped. KBr impregnated sample exhibited the highest adsorption energy among all the alkaline impregnated samples so that the experimental adsorption curve was above the plain carbon. It is summarized that experimental results were in good agreement with computational works and both demonstrated that electrostatic forces could enhance the hydrogen adsorption and the adsorption energy could be highly increased.

4.4 Section 4 References

- [1] J. Hayashi, T. Horikawa, I. Takeda, K. Muroyama, F. N. Ani, *Carbon*, 40 (2002) 2381-2386, "Preparing activated carbon from various nutshells by chemical activation with K_2CO_3 ".
- [2] J. Yang, Z. Shen, Z. Hao, *Carbon*, 42 (2004) 1872-1875, "Preparation of highly microporous and mesoporous carbon from the mesophase pitch and its carbon foams with KOH".
- [3] Y. Ji, T. Li, L. Zhu, X. Wang, Q. Lin, *Applied Surface Science*, 254 (2007) 506-512, "Preparation of activated carbons by microwave heating KOH activation".
- [4] Y. Guo, S. Yang, K. Yu, J. Zhao, Z. Wang, H. Xu, *Materials Chemistry and Physics*, 74 (2002) 320-323, "The preparation and mechanism studies of rice husk based porous carbon".
- [5] M. Jordá-Beneyto, F. Suárez-García, D. Lozano-Castelló, D. Cazorla-Amorós, A. Linares-Solano, *Carbon*, 45 (2007) 293-303, "Hydrogen storage on chemically activated carbons and carbon nanomaterials at high pressures".
- [6] Y. Xu, J. Li, Y. Zhang, W. Chen, *Surface Science*, 525 (2003) 13-23, "CO adsorption on MgO(001) surface with oxygen vacancy and its low-coordinated surface sites: embedded cluster model density functional study employing charge self-consistent technique".
- [7] A. Damin, R. Dovesi, A. Zecchina, P. Ugliengo, *Surface Science*, 479 (2001) 255-272, "CO/MgO(0 0 1) at different CO coverages: a periodic ab initio Hartree-Fock and B3-LYP study".

- [8] T. Bredow, G. Geudtner, K. Jug, *Journal of Computational Chemistry*, 22 (2001) 89-101, "Development of the cyclic cluster approach for ionic systems".
- [9] A. B. Anderson, *Chemical Physics Letters*, 72 (1980) 514-517, "NiO Bulk properties: Initial-state molecules-orbital Ni₄O₄ and Ni₁₃O₁₄ cluster studies".
- [10] X. Xu, H. Nakatsuji, M. Ehara, X. Lü, N. Q. Wang, Q. E. Zhang, *Chemical Physics Letters*, 292 (1998) 282-288, "Cluster modeling of metal oxides: the influence of the surrounding point charges on the embedded cluster".
- [11] T.P. Blacha and E. MacA. Gray, *Journal of Alloys and Compounds*, 446-447 (2007) 692-697, "Sieverts apparatus and methodology for accurate determination of hydrogen uptake by light-atom hosts".
- [12] Crystallography Open Database, <http://www.crystallography.net/>
- [13] Zheng Shi, Jiujun Zhang, Zhong-Sheng Liu, Haijiang Wang, David P. Wilkinson, *Electrochimica Acta*, 51 (2006) 1905-1916, "Current status of ab initio quantum chemistry study for oxygen electroreduction on fuel cell catalysts".
- [14] J. E. Bushnell, P. R. Kemper, and M. T. Bowers, *Journal of Physical Chemistry*, 98 (1994) 2044-2049, "Na⁺/K⁺(H₂)_{1,2} clusters: binding energies from theory and experiment".
- [15] P. Bénard and R. Chahine, *Langmuir*, 17 (2001) 1950-1955, "Determination of the adsorption isotherms of hydrogen on activated carbons above the critical temperature of the adsorbate over wide temperature and pressure ranges".
- [16] X. B. Zhao, B. Xiao, A. J. Fletcher, and K. M. Thomas, *Journal of Physical Chemistry B*, 109 (2005) 8880-8888, "Hydrogen adsorption on functionalized nanoporous activated carbons".
- [17] Y. Kojima, Y. Kawai, A. Koiwai, N. Suzuki, T. Haga, T. Hioki and K. Tange, *Journal of Alloys and Compounds*, 421 (2006) 204-208, "Hydrogen adsorption and desorption by carbon materials".

5. HYDROGEN ADSORPTION ON METAL ELECTRODES

5.1 Introduction

Since interaction between hydrogen and polarized substances is still weak at room temperature or at applicable cryogenic conditions (77 K), by applying extremely high electric fields, the polarity of the materials could be further enhanced so that the interaction of hydrogen could be increased. Moreover, if metallic electrodes are used (e.g. Ni), such high electric fields would make the electrodes of the anode side lose their electrons, temporary becoming ionic electrodes (e.g. Ni²⁺). From previous discussion, such metallic ions may form stronger bonding to hydrogen, so that the hydrogen uptake could be enhanced. Overall, significant adsorption at room temperature may be realized.

5.2 Experimental

5.2.1 High electric field testing device

A schematic diagram of the whole system is described in Figure 5.1. A stainless steel gas line was connected to a safety high pressure case constructed with 0.25 inch thick steel. A high pressure stainless steel reactor having a 3000 psi pressure relief valve was put at the center of the steel case. The sample was put in the reactor with the two end electrodes connected to the external electrical system. A high voltage DC power supply device which is capable of providing voltage from 200 volts to 20000 volts from Del High Voltage Corp. (model RLPS 100-100 P) was used. A high voltage switch and an electric circuit were connected between the power supply and the sample. The electrical signals coming from the circuit was transformed to the computer by an InstruNet PCI Network Controller (OMEGA Engineering, INC).

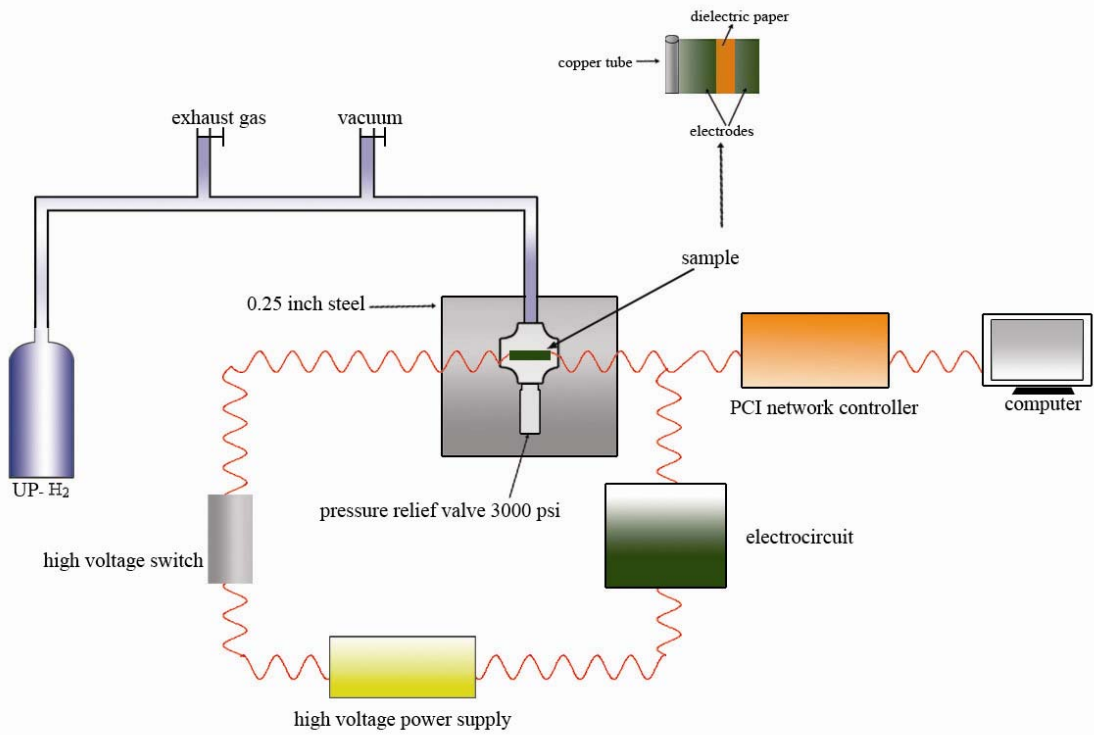


Figure 5.1. High electrical field testing system

A more detailed diagram of the electrical circuit is shown in Figure 5.2. There are two parallel voltage lines connected to the power supply. The resistor 2 connected with the reactor was used to record the leakage signals at the charging process. If there are any leaks from the reactor or if the reactor is shorted, the resistor 2 would have significant voltage on it. Resistor 1 in another parallel line was used to record the charge and discharge signals. When the reactor was being charged, there was also a voltage applied on resistor 1 and the voltage variation of resistor 1 would indicate how the reactor was being charged. After the charging process, when the high voltage switch was opened, the charges stored in the reactor would be released via the parallel line so that the responding voltage on resistor 1 can give the discharge signals. Both resistor 1 and resistor 2 were connected to a PCI network controller to transform the electrical signals to data signals. And the computer would record these signals and store them in the hard disk. The samples were rolled as the form of an aluminum electrolytic capacitor with two metal layers and two dielectric paper layers. Figure 5.3 shows how the electrodes were constructed.

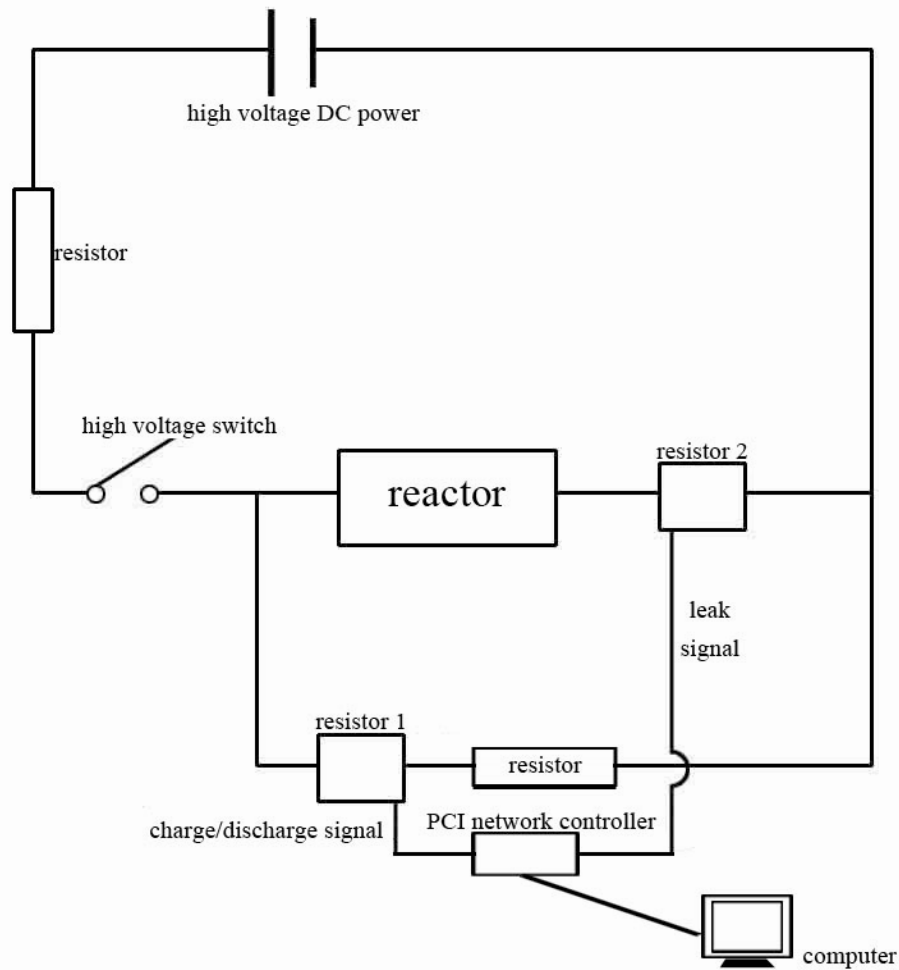


Figure 5.2. Electric circuit of the high electric field system

It is proposed that under the high electric field, the electrode itself would be ionized (e.g. $\text{Ni} \rightarrow \text{Ni}^{2+}$). And also the hydrogen molecule would be polarized under such high electric fields and then attached to the electrode surface. The surrounding hydrogen molecules may also be polarized by the previous hydrogen molecule and form hydrogen clusters. Moreover, hydrogen molecules may dissociate on the electrode surface becoming hydrogen atoms, which can in turn bond to the ionized electrode. Under extreme condition, hydrogen plasma may form and the hydrogen ions can also form bonding with the electrode surface. A detailed schematic of such a mechanism is shown in Figure 5.3.

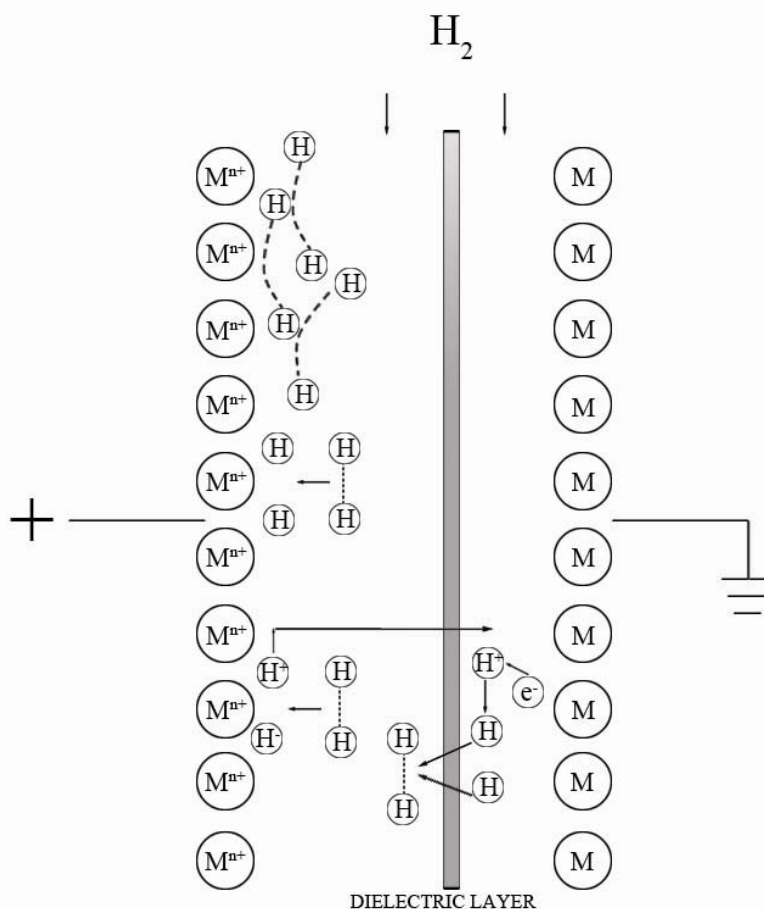


Figure 5.3. Adsorption mechanism of the electrodes

When the electric field was released, the hydrogen substances would go back to their normal condition and became hydrogen gas. The electric circuit would give corresponding signals when this phenomenon occurred. In such cases, electrodes with high surface areas would be utilized to have substantial adsorption ability.

5.2.2 Electrode formation

Two layers of nickel screen and two layer of dielectric paper were rolled up and tested. The nickel screen was at the dimension of 32.75 inch (length) \times 1.375 inch (width) \times 0.003 inch (thickness) and sieve size of 400 mesh (37 μ m). The dielectric paper was at the same dimension.

5.3 Results and Discussion

5.3.1 Nitrogen gas adsorption

Because nitrogen gas is more easily to be adsorbed than hydrogen, it was first tested in the high electrical device. The experiments were conducted at room temperature. The charging signals from resistor 1 for nitrogen gas at pressure of 50 psi and different voltage are shown in Figure 5.4. Here the notation of the lines is that n stands for nitrogen gas, 0050 stands for gas pressure in psi, and 0200 stands for the applied voltage in volts. At the same gas pressure, applying higher voltage may increase the interaction between gas molecules and electrodes. It took less than 0.1 second for the capacitor to reach the saturated voltage indicating that the charging process was very fast. The voltage added on the electrodes increased consistently with the increasing of the applied external voltage. However, at 50 psi, when the voltage increased to 2000 V, the voltage signals began to fluctuate. This is an indication of the generation of plasma. When the voltage was higher than the breakdown voltage of nitrogen gas, the nitrogen molecules would become high energy state atoms and molecules or be split into positive and negative ions. With these substances especially the ions in the chamber, the electric circuit may temporarily be shorted so that the voltage could not be added on.

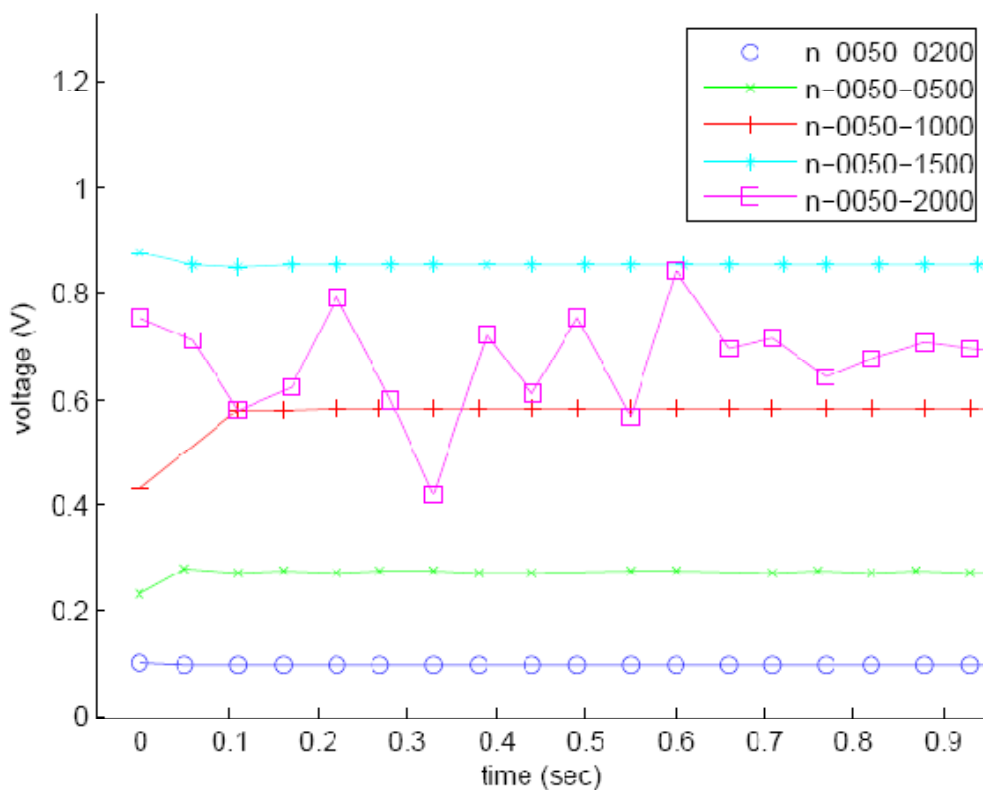


Figure 5.4. Charging signals at resistor 1 at 50 psi nitrogen pressure, applied voltage 200 V to 2000 V

The voltage signals from resistor 2, which gives the leakage signals, also confirmed this opinion. As in Figure 5.5, the leakage for voltage below 2000 volts was negligible. Big differences occurred when the voltage reached 2000 volts. Here, the voltage leaked was very high in comparison with the charging voltage. Plasma is the reason that the charging process at such voltage looked like adding voltage onto a temporary shorted circuit.

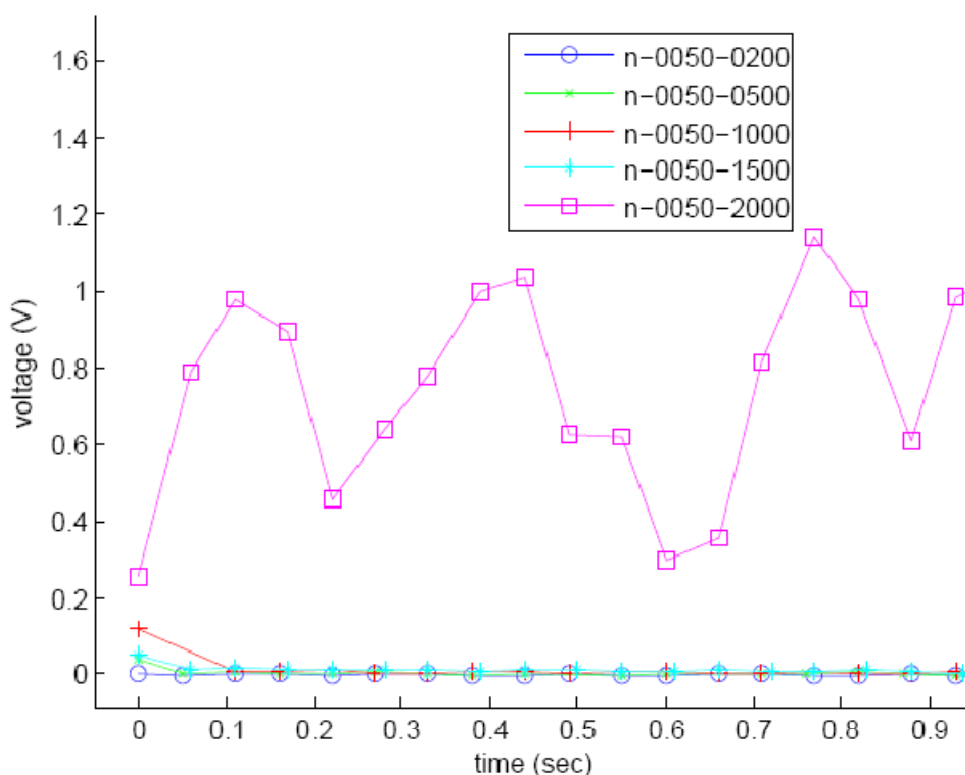


Figure 5.5. Leakage signals at charging at 50 psi nitrogen pressure, applied voltage 200 V to 2000 V

When the voltage was released, the discharge began and the signals from resistor 1 presented the discharge magnitude, which was also an indication of how much nitrogen was stored during the charging process. As shown in Figure 5.6, the discharging lines have the same characteristic shape as the normal discharge line in the capacitor. This was an obvious indication that some charges were stored on the electrodes. The trend lines also showed that at the same gas pressure, the discharging voltage increased with the increasing of charging voltage. This is easy to understand. Based on the equation (9), total charges (Q) stored in the capacitor are equal to the product of capacity (C) and applied voltage (V).

$$Q = CV \tag{9}$$

Higher voltage would result more charges stored and more nitrogen adsorbed on the electrodes. At 2000 volts, because the plasma was initiated, the actual voltage applied on the capacitor was

lower than 2000 volts, so that the final discharging voltage or nitrogen capacity was lower than 1500 volts. Therefore, for gas pressure of 50 psi, 1500 volts yielded the best adsorption.

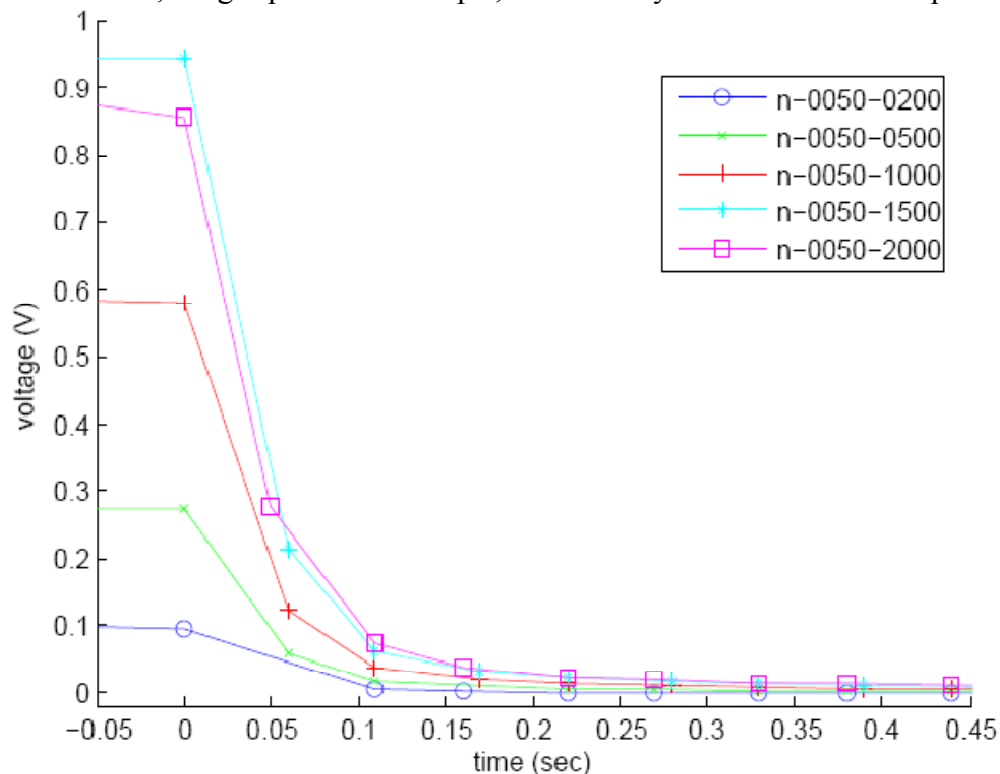


Figure 5.6. Discharge signals at 50 psi nitrogen pressure, applied voltage 200 V to 2000 V

The nitrogen gas pressure was raised to 150 Psi to study the pressure effects. The charging signals from resistor 1 are shown in Figure 5.7. The voltage charged on the electrodes increased with the increasing of applied external voltage, the same as the 50 Psi pressure. However, here the signals at 2000 volts didn't show any fluctuations, indicating no plasma was produced. It took about 0.2 seconds for the voltage to become stable. This is because that at higher gas pressure, the gas molecules are harder to be split since much more energy should be applied in order to break down so many molecules. In plasma science, usually plasma is generated under gas pressure of several millitorr. At high gas pressure, usually a field concentrator or higher energy should be used to generate plasma. The magnitude of the voltage applied on the electrode is higher than the magnitude in 50 Psi, for example, 1 V in 150 psi and 0.85 V in 50 psi, both at 1500 volts external voltage. This indicated that more nitrogen species were adsorbed on the electrodes.

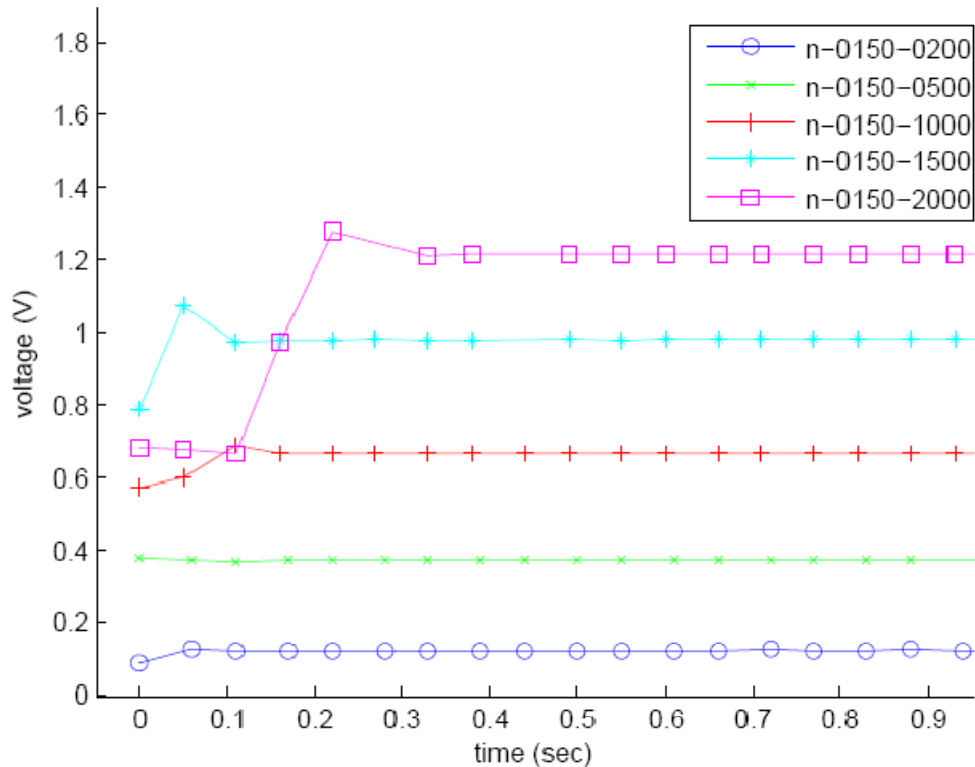


Figure 5.7. Charging signals at 150 psi nitrogen pressure, applied voltage 200 V to 2000 V

From the leakage signals of resistor 2 during charging (Figure 5.8), the leaking for every external voltage was nearly zero except the beginning of 2000 volts. This also confirms that there was no plasma generated during the charging process.

The discharge signals which are also the characteristics of nitrogen capacity are presented in Figure 5.9. Here the trend is very clear. Higher external voltage would result in better adsorption. By comparing with the results of 50 psi, the discharging magnitude was higher, which also indicated that the adsorption was better at higher pressure. Overall, higher pressure and higher applied voltage would favor nitrogen adsorption.

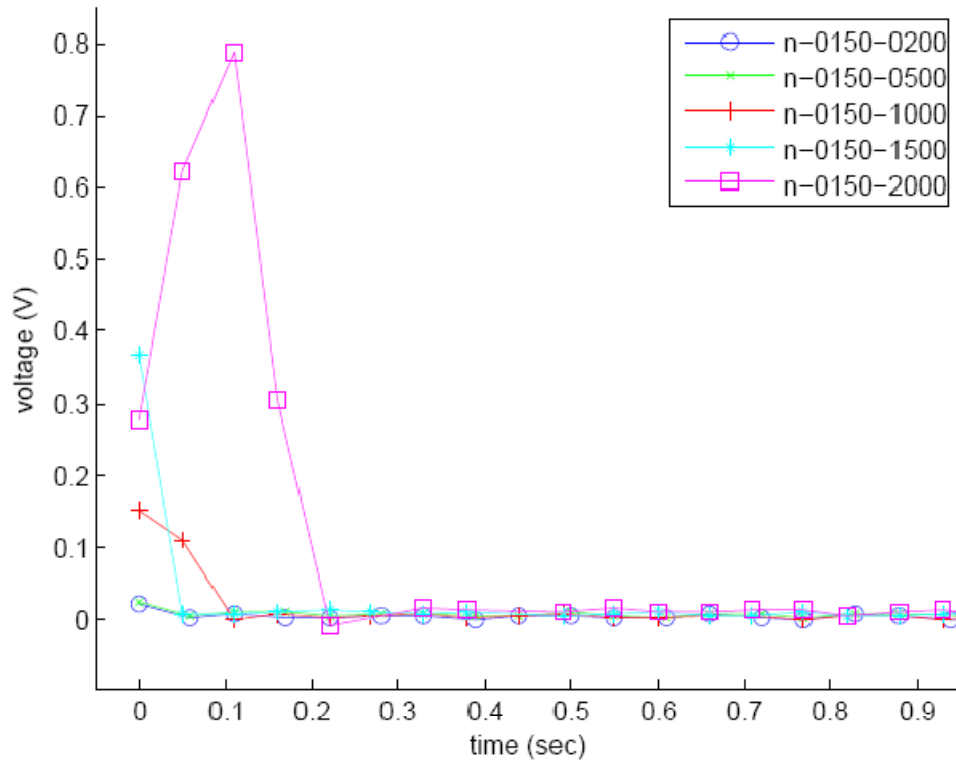


Figure 5.8. Leakage signals at 150 psi nitrogen pressure, applied voltage 200 V to 2000 V

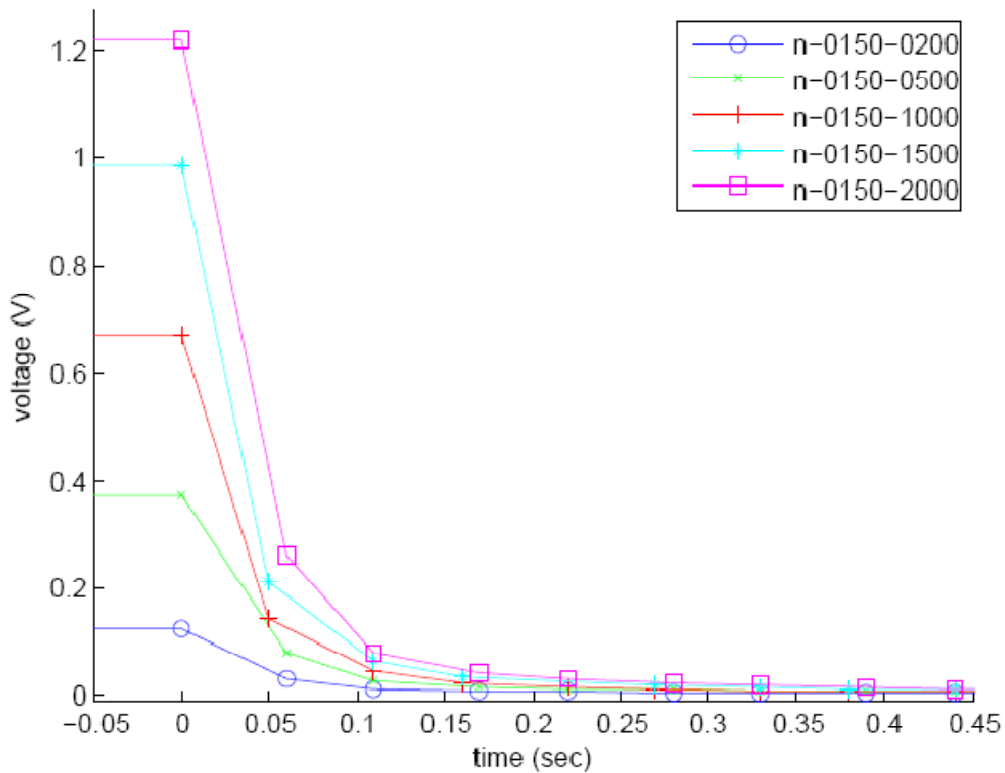


Figure 5.9. Discharge signals at 150 psi nitrogen pressure, applied voltage 200 V to 2000 V

5.3.2 Hydrogen gas adsorption

Hydrogen gas was tested the same way as nitrogen gas. The charging signals of resistor 1 for hydrogen pressure of 40 Psi are shown in Figure 5.10. The trend was the same as nitrogen gas; higher external voltage would result in higher voltage on the electrodes. However, at 1500 volts and 2000 volts, plasma was generated as presented by the fluctuated voltage signals. The voltage could not be added on under such circumstance.

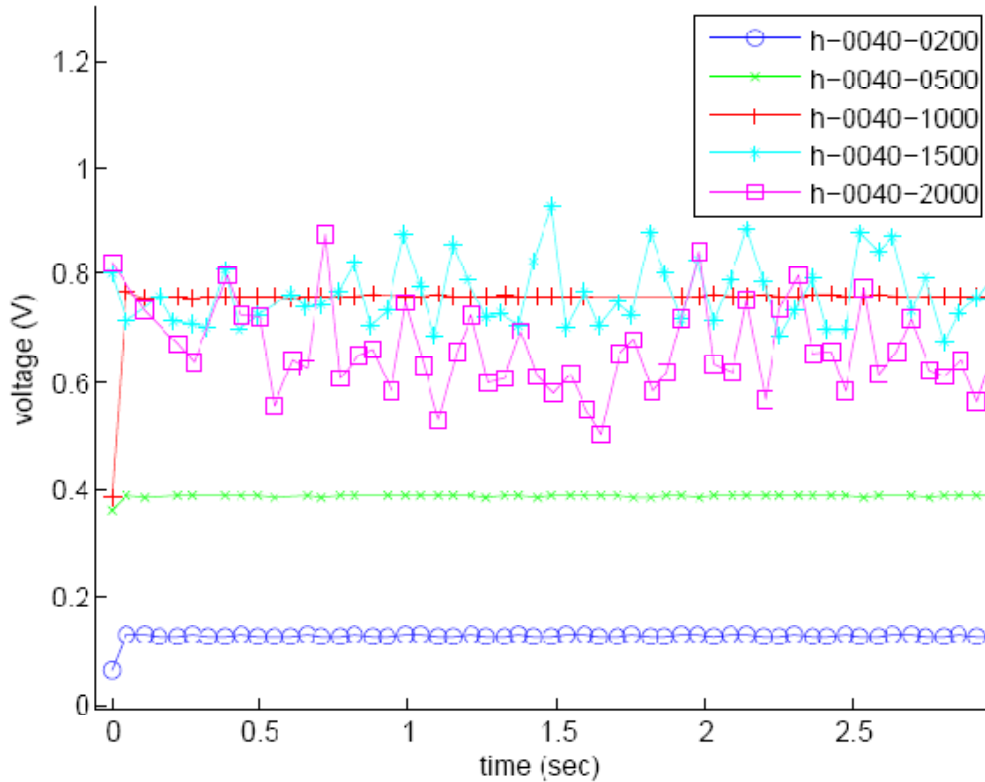


Figure 5.10. Charging signals at 40 psi hydrogen pressure, applied voltage 200 V to 2000 V

A more presented look about the plasma is shown in Figure 5.11 as the leakage signals during charging. The voltage leak for 1500 volts and 2000 volts were very large comparing nearly zero leaks at other voltages. Plasma was produced and the condition at 2000 volts was more severe.

The hydrogen adsorption capacity was presented by the discharging curve on resistor 1. As shown in Figure 5.12, higher voltage yielded better hydrogen adsorption ability. However, with the occurrence of plasma, part of the external applied high voltage was wasted in the short circuit, so that the overall adsorption was equal or less than 1000 volts.

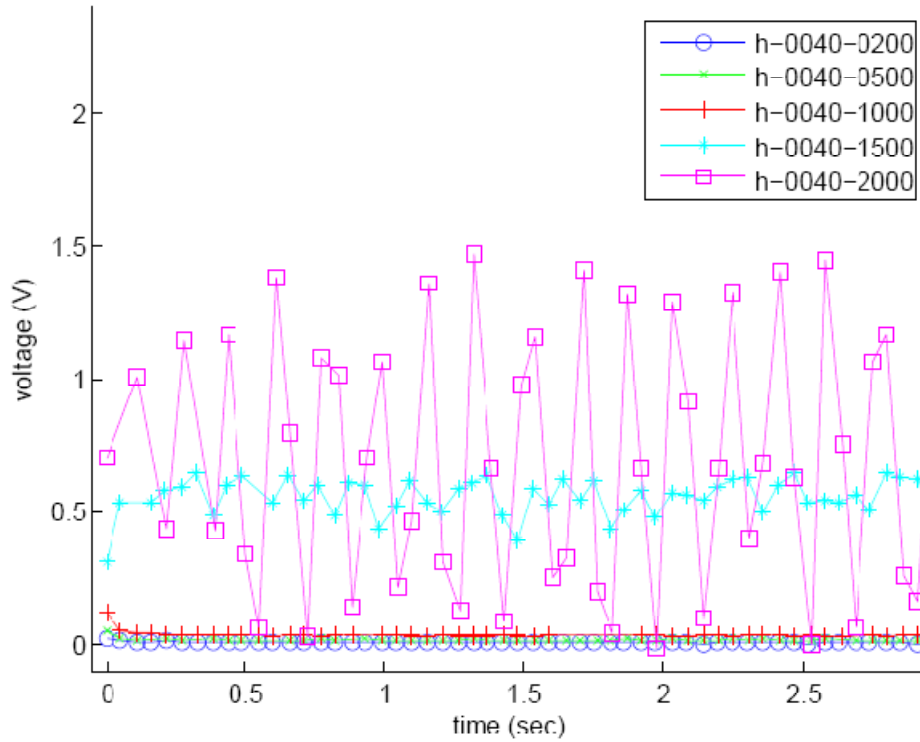


Figure 5.11. Leakage signals at 40 psi hydrogen pressure, applied voltage 200 V to 2000 V

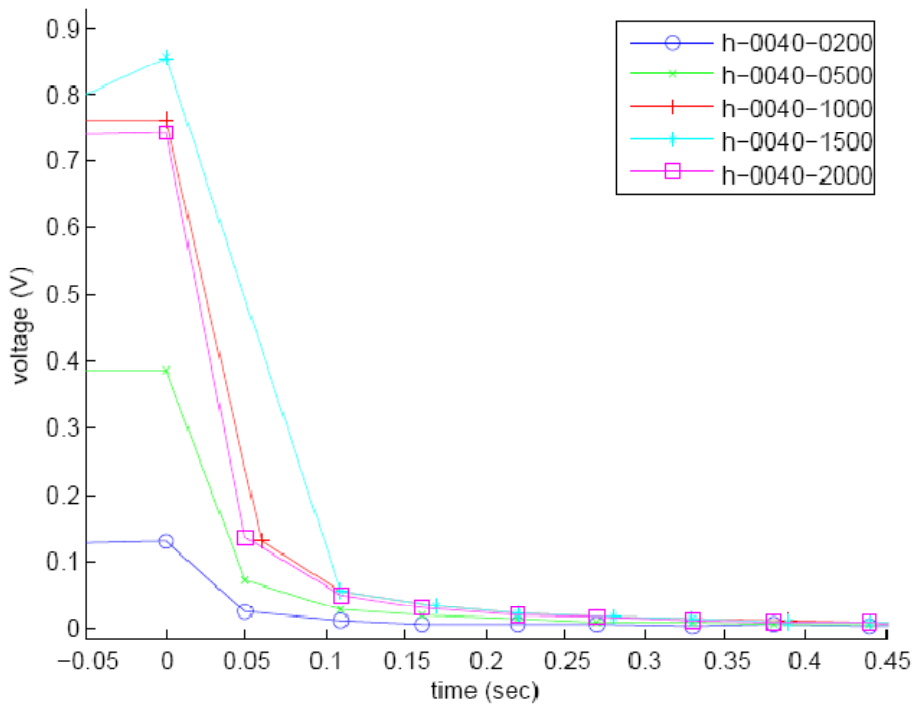


Figure 5.12. Discharge signals at 40 psi hydrogen pressure, applied voltage 200 V to 2000 V

More experiments at higher hydrogen gas pressure were also conducted. Selected results at charging process are shown in Figure 5.13. At 200 psi, there was still plasma generated as presented at the swing charging signals at high voltage. With higher pressure, the signals became stable at every voltage level because more hydrogen molecules needed higher energy to generate plasma.

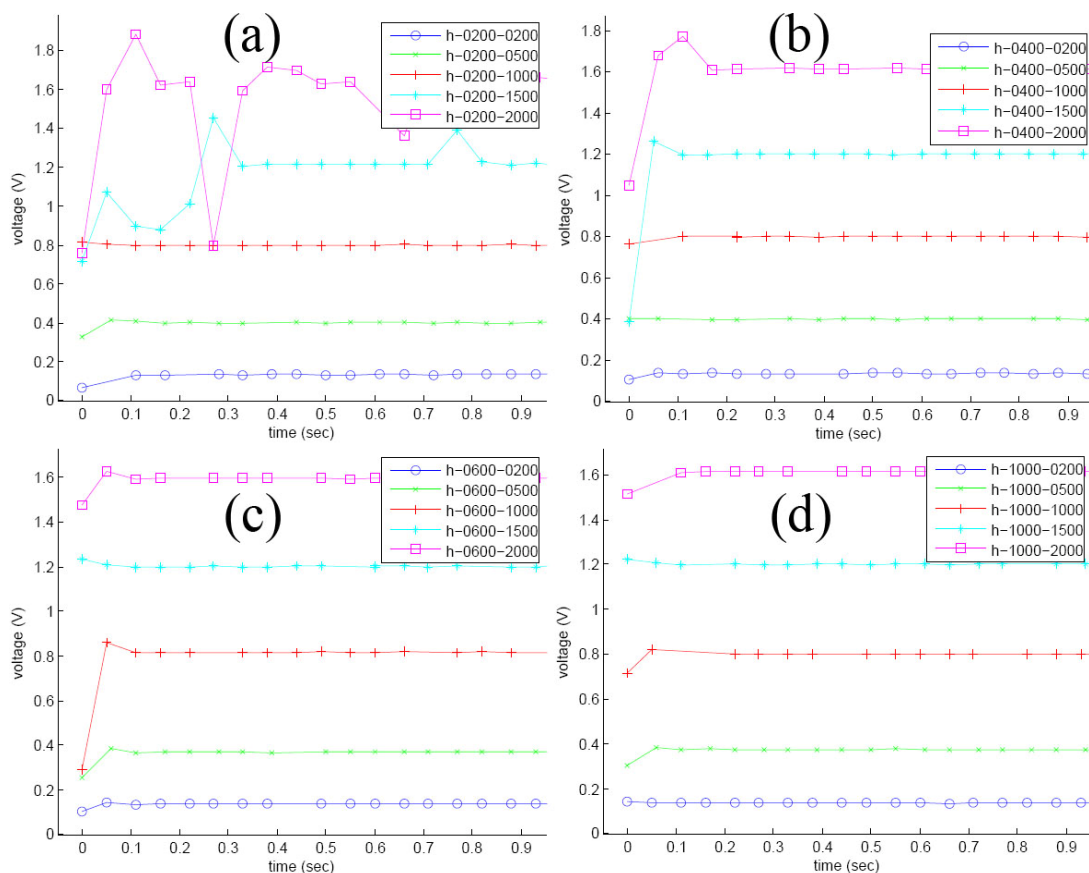


Figure 5.13. Charging signals at hydrogen pressure (a) 200 psi, (b) 400 psi, (c) 600 psi, (d) 1000 psi, applied voltage 200 V to 2000 V

Their corresponding discharge signals are shown in Figure 5.14. Higher external voltage would result in better hydrogen adsorption at any gas pressure. However, with the increasing of the gas pressure from 200 psi to 1000 psi, the magnitude of discharge or in other words, the hydrogen adsorption capacity didn't increase. For example, at 2000 volts, the highest discharge point for every pressure was about the same, which was about 1.6 volts. On the other hand, by comparing with 40 psi, the highest point at 2000 volts was 0.73. Obviously, the difference was caused by the generated plasma at 40 psi that the total voltage was not added on. If we compare all gas pressure at 1000 volts, where no plasma was produced, the discharging point was 0.77 for 40 psi

and around 0.8 for other pressure. Therefore, increasing pressure from 40 psi to 200 psi was beneficial for hydrogen adsorption. However, further higher pressure was not useful.

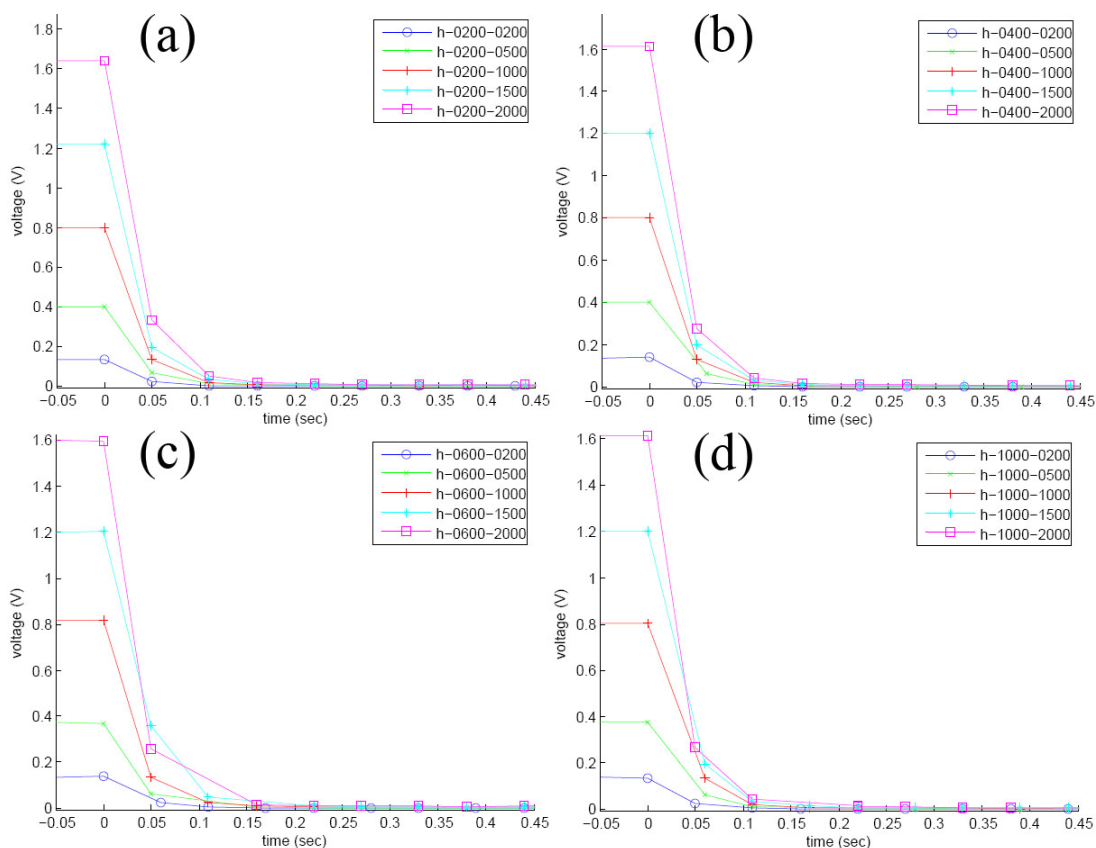


Figure 5.14. Discharge signals at hydrogen pressure (a) 200 psi, (b) 400 psi, (c) 600 psi, (d) 1000 psi, applied voltage 200 V to 2000 V

A closer look at the discharging signals of different gas pressure and the same applied external voltage is shown in Figure 5.15. At any applied voltage, changing pressure from 200 psi to 1000 psi didn't show any significant effects on the hydrogen adsorption. On the other hand, increasing applied voltage was beneficial. This is because that higher voltage would increase the interaction between hydrogen species and the electrodes so that the total hydrogen adsorbed would be increased. For the pressure, a possible explanation is that when the pressure was increased from 40 psi to 200 psi, the electrode surface was not saturated with the adsorbed hydrogen, so that more hydrogen would be attached to the electrode at higher gas pressure. However, when the pressure was above 200 psi, the electrode surface was total covered with hydrogen species so that there were no space for other hydrogen to be attached on even the total number of hydrogen molecules was in large amount.

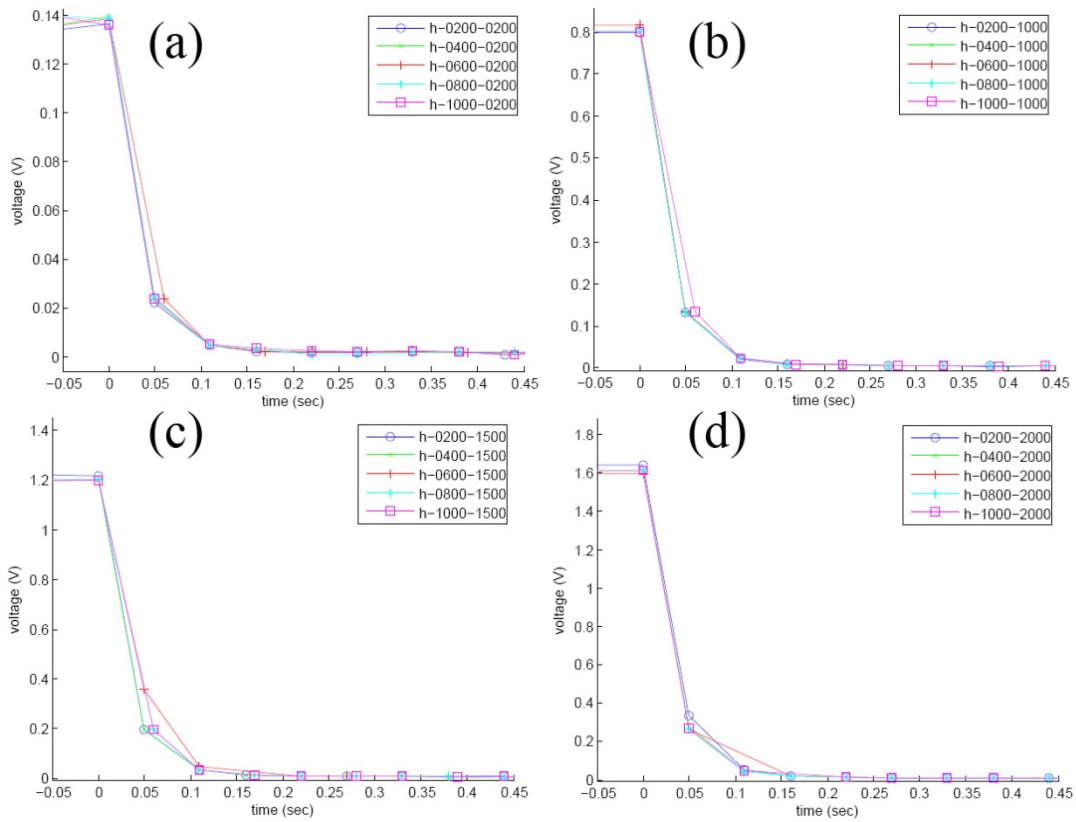


Figure 5.15. Discharge signals at applied voltage (a) 200 V, (b) 1000 V, (c) 1500 V, (d) 2000 V, Hydrogen pressure from 200 psi to 1000 psi

6. ELECTRIC FIELD ASSISTED HYDROGEN ADSORPTION ON POROUS METAL OXIDES

6.1 Introduction

After successfully observing that external electric fields showed potential enhancement on hydrogen adsorption both in experimental and by computational means, a quantitative examination was carried out to determine how much enhancement could be generated by applying the electric fields on storage materials.

Porous metal oxides have been researched and used extensively for catalyst support [1], gas storage [2-3], and sensors [4]. Among these, nickel oxides and magnesium oxides have received extensive focus due to their inexpensive costs and better properties. Moreover, due to increasing current interest in energy storage, supercapacitors have been researched extensively in recent years. Besides carbon materials, porous metal oxides including nickel oxides have been researched as alternative materials to increase capacity [5-6]. Both nickel oxides and magnesium oxides are ionic solids and have rocksalt structure, making them ideal materials for studying electrostatic attraction of hydrogen molecules. The major task of developing metal oxides for hydrogen storage is to generate oxides with high surface area and coordinative unsaturation of the metal cation sites [3]. Surfactant templating growth of nano sized metal oxides has been recently developed to achieve mesoporous oxides with high surface area, and high thermal and hydrothermal stability [7-8].

Besides the intrinsic electrostatic induced dipole, externally applied electrical potential could further enhance the electrostatic effects. Piezoelectric materials are substances that can generate electrical potential in response to the external stress [9]. Under high hydrostatic hydrogen gas pressure, substantial voltage potential could be generated across the positive and negative sides of the piezoelectric materials [10]. By embedding the piezoelectric material into the ionic adsorbent, the electrostatic interaction could be further enhanced so that the total hydrogen storage could be remarkably increased.

Here highly porous nickel oxide and magnesium oxide have been synthesized by surfactant directed growth and studied for hydrogen storage. A commercially available piezoelectric material PMN-PT was applied to generate external electric field across the oxides and corresponding effects on hydrogen adsorption have been investigated. Moreover, DFT computational work has been carried out on hydrogen adsorption on oxide surfaces and the effects of external electric field on adsorption have also been studied to reveal underlying principles.

6.2 Experimental

6.2.1 Synthesis of porous oxides

The porous oxides were synthesized following previously developed techniques [8,11]. Typically, for porous nickel oxides, 13.19 g $\text{NiCl}_2 \cdot 6\text{H}_2\text{O}$, 32.01 g sodium dodecyl sulfate (SDS), 100g urea, and 60 ml DI water were magnetic stirred at 40 °C for 1 hour to obtain a transparent solution. For porous magnesium oxides, 10.17g $\text{MgCl}_2 \cdot 6\text{H}_2\text{O}$, 28.84g SDS, 90g urea, and 54 ml DI water were mixed. And then the mixture was transferred to an 80°C oil bath and further reacted for 6 hours. The obtained slurry was cooled and filtrated, and then dried at 120 °C overnight. The solids were then ground and washed several times with ethanol to remove the surfactant. The final products were dried in oven and then heated at different temperature for various times to obtain porous oxides.

6.2.2 Platinum deposition

The platinum deposition on porous nickel oxide was prepared by the wet impregnation-reduction method [12-14]. Typically, 0.6 g porous NiO was mixed with 80 ml DI water in a 90°C oil bath with a continuous Argon gas purge. A 6.4 ml 50 mM H_2PtCl_6 solution was added to the slurry. A 2M NaOH solution was used to adjust the slurry PH to 11-13. Subsequently, a 3.75 ml HCHO (37%) was added dropwise and stirred continuously for 2h. The final products were washed, filtrated and dried in air.

6.2.3 Characterization of the synthesized oxides

The surface area and pore size distribution were analyzed by using a Micromeritics ASAP2000 instrument. The samples were evacuated by heating at 200 °C under vacuum for 12 hours before testing. The tubing containing the degassed samples were then sealed and carefully transferred to a balance to obtain the sample weight.

Differential thermo analysis was performed on NET DSC404 at a heating rate of 10 K/min. X-ray diffraction (XRD) analysis was carried out on a Scintag XDS2000 Powder Diffractometer at a scan rate of 0.08°/s with Cu radiation at 45 kV, 35 mA.

A Hitachi S-4700 field emission-scanning electron microscopy (FE-SEM) was used to examine the microstructure of the samples. The incorporated Energy Dispersive Analysis (EDS) was employed to analyze the element concentrations.

6.2.4 Hydrogen storage measurements

Hydrogen adsorption at pressure between 0.1 bar and 80 bar was measured by using static volumetric techniques with an automatic Sieverts' apparatus (PCT-Pro 2000 from Hy-Energy LLC) at both room temperature and 77k. Previous to the test, samples were degassed extensively at 200 °C for 12 hours and then carefully moved into the sample holder and evacuated again at 100 °C for 2 hours to ensure the remove of any contaminations on the sample surface. Around 100-300 mg of the sample was used in each test, and ultra pure (99.999%) hydrogen and helium gases were used for all calibrations and measurements.

A single crystal PMN-PT disk was acquired from Morgan Electro Ceramics, 5 mm in length and width, and 1 mm in thickness. As shown in Figure 6.1, the positive side of the PMN-PT was covered by a non-conductive thin BaTiO₃ film to prevent electron transfer. The film was made by BaTiO₃ powders and glue. The PMN-PT was immersed in the tested adsorbents and both were positioned in a glass tube which was placed in a stainless steel sample holder. In such arrangement, the electrons from the PMN-PT were not able to transfer to the outside so that the electric field could be preserved inside the adsorbents. The g_{33} parameter of the PMN-PT is 15.8×10^{-3} Vm/N, which means that the PMN-PT can generate significant voltage under pressure.

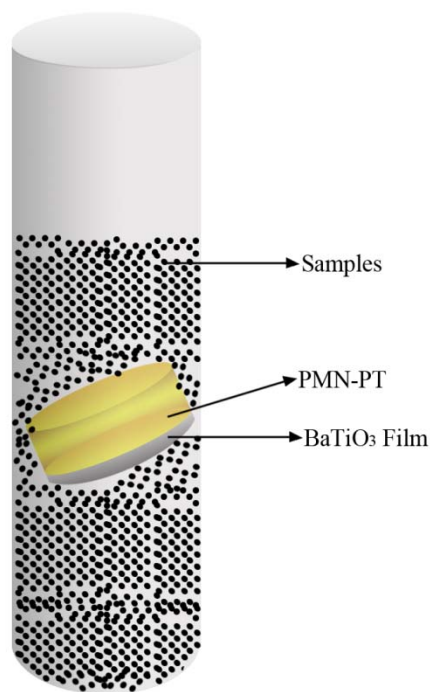


Figure 6.1. Schematic of sample holder arrangement

6.2.5 Computational method

Similar computational methods as described in Chapter six were used. The M_5O_5 oxide clusters were first embedded in $13 \times 13 \times 13$ point charges to find the value of the point charges that can well reproduce the cluster bond length. Then the clusters were moved to the surface and hydrogen adsorption was calculated. For the calculation of the effects of the external electric field, the applied field was applied along the vertical direction at a field strength of 0.001 au, 0.005 au, and 0.015 au, which equals to 5.14×10^8 V/m, 2.57×10^9 V/m, and 7.71×10^9 V/m, respectively. The total binding energy was calculated by the difference between the total energy of the whole adsorption system and the total energy of the separate reactants before combination, as presented in equation (10):



All the calculations were performed by using DFT/B3LYP method and a basis set of 6-31 G(d) in GAUSSIAN 03 program. DOS analysis was visualized in GAUSSSUM software [15].

6.3 Results and Discussion

6.3.1 Porous nickel oxides

6.3.1.1 Characterization of as synthesized oxides

The XRD graph of as synthesized porous nickel hydroxide is shown in Figure 6.2. The pattern is a good match of nickel hydroxide hydrate $3Ni(OH)_2 \cdot 2H_2O$. The wide peak interspace indicated the small particle size and low degree of crystallization.

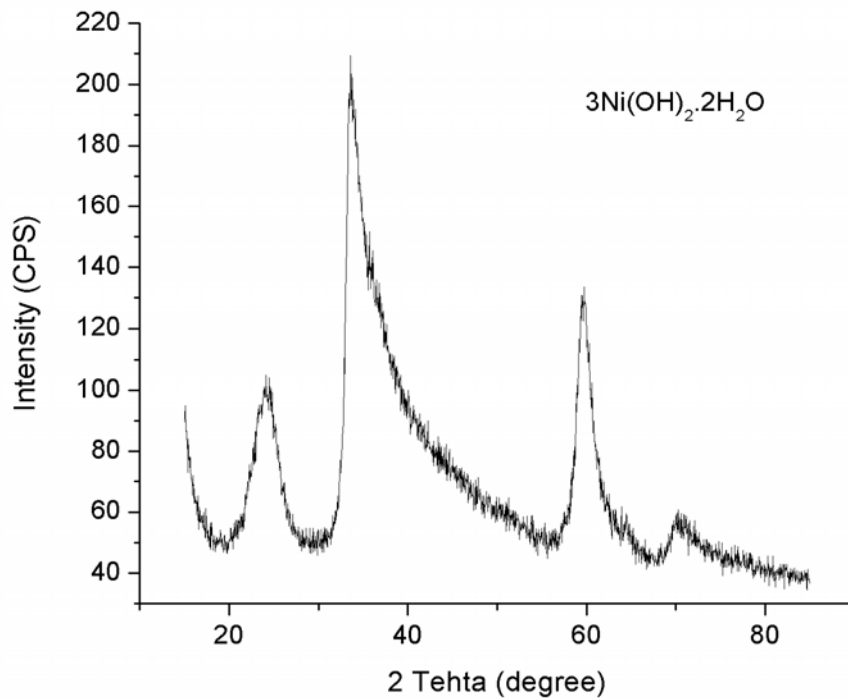


Figure 6.2. XRD pattern of as-synthesized nickel oxide

This is consistent with the SEM analysis of the synthesized particles. As in Figure 6.3, the particles are interconnected with each other and the particles size is around 100-300 nm.

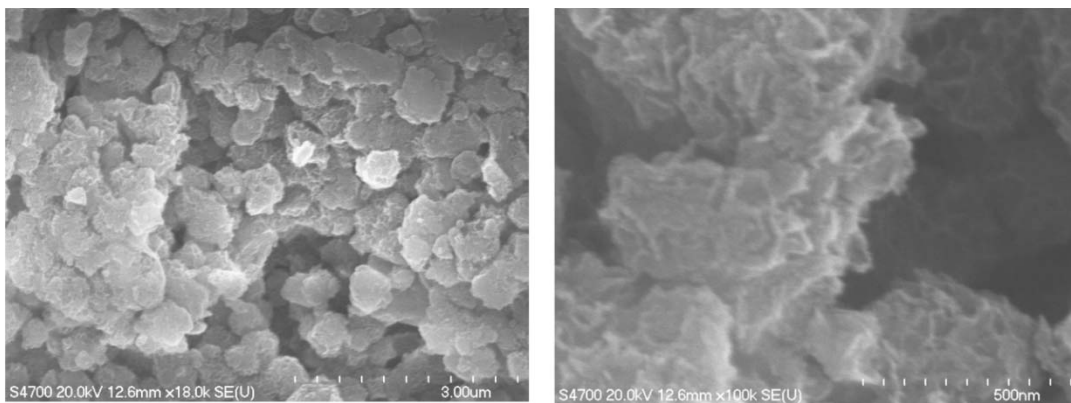


Figure 6.3. FE-SEM images of as-synthesized nickel oxides

The urea was used as the hydroxide provider for precipitation where the urea undergoes hydrolysis at temperature above 60 °C, as described by following reaction:



Then the precipitation grew along the direction of the surfactant so that the synthesized particle surface preserved the surfactant texture, as seen from the accented edges of the particles.

DTA analysis was carried out for as-synthesized nickel hydroxide in air to study the reaction process under calcinations conditions. The obtained DTA curve is shown in Figure 6.4. Two endothermic peaks were observed. The wide peak presented between 50 to 250 °C corresponds to the removal of water from the $\text{Ni}(\text{OH})_2$. The sharp peak between 300 to 400 °C corresponded to the removal of hydroxyl groups to form NiO . The calcinations temperature and time are two critical factors for obtaining oxides with highly porous structures. With the increase of temperature, the pore structure of the samples may undergo major changes so that less calcinations time should be used to prevent the collapse of the pore structure [11]. From the DTA curve, the reaction started from 300 °C and the center position of the peak was at around 360 °C. Therefore, calcinations of $\text{Ni}(\text{OH})_2$ were conducted at 300 °C and 360 °C for different time to obtain the optimum condition for achieving the porous NiO with the highest surface area.

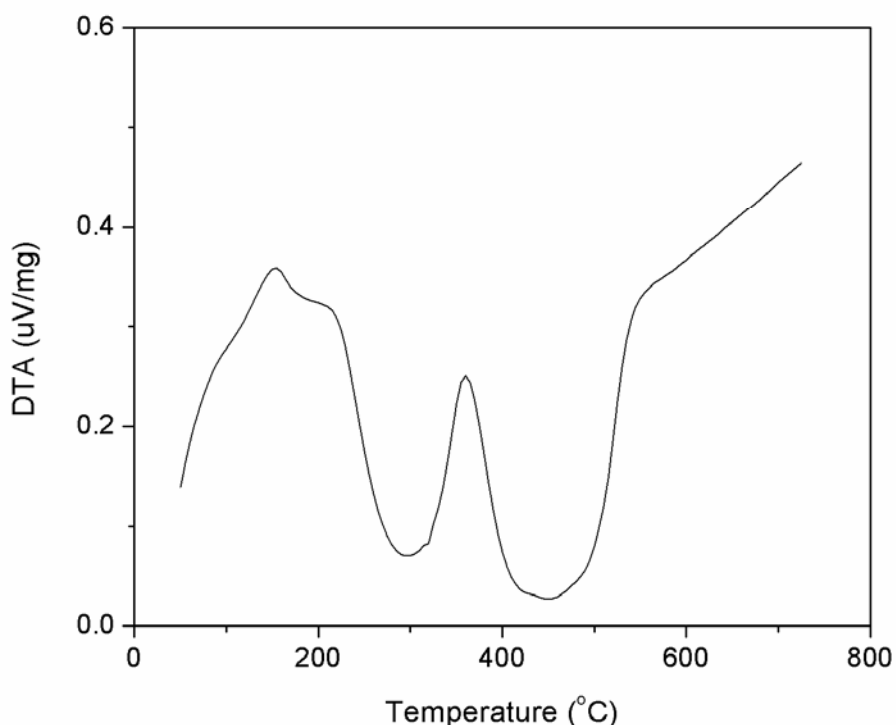


Figure 6.4. DTA curve of as-synthesized nickel oxides

The adsorption isothermals of mesoporous nickel oxides calcined at 300°C and 360 °C for various time are shown in Figure 6.5. Regardless of the calcination temperature and time, the obtained porous nickel oxides preserved mesoporous characteristic. However, by comparing curves at 300°C and 360 °C, higher temperature yielded smaller mesopore volume, and longer

calcination time at high temperature caused widening of the pore structure, as revealed by the shrinkage of the hysteresis of the adsorption isotherms.

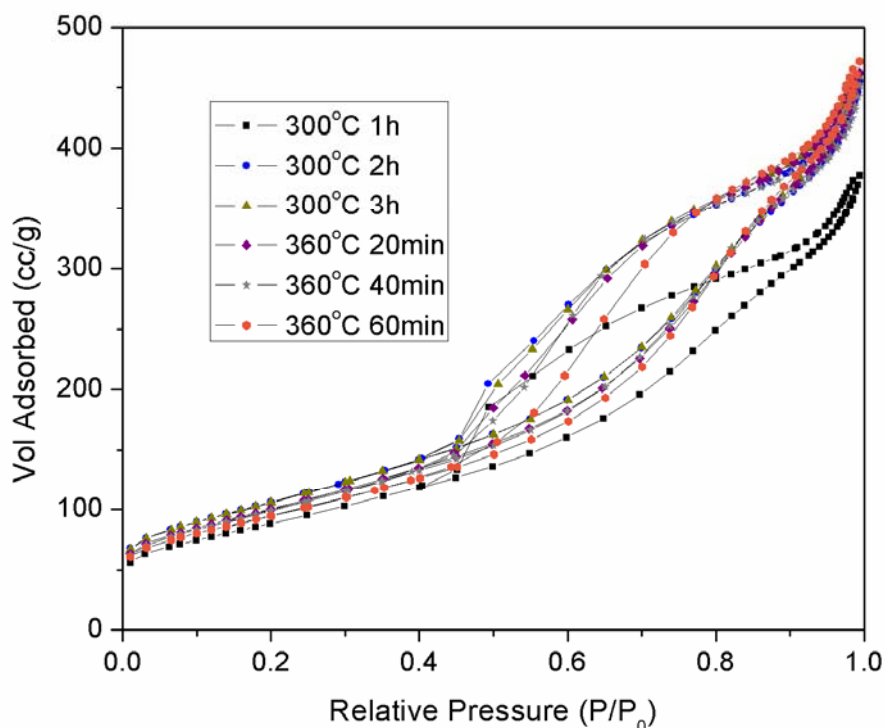


Figure 6.5. Adsorption isotherms of the mesoporous nickel oxides calcined at 300 °C and 360 °C for different time

Surface area and pore size properties of calcined products were summarized in Table 6.1. The BET surface area increased with the increasing of calcinations time from 1 hour to 2 hours at 300 °C and further increasing calcinations time caused minor enhancement on the total surface area. The average pore diameter was around 7 nm. At such temperature, the decomposition of Ni(OH)₂ slowly developed and the pore skeleton generated was very stable. With the calcinations temperature increased from 300 °C to 360 °C, the total surface area dropped and longer heating time resulted lower surface area. Obviously, the decomposition of Ni(OH)₂ took place too fast at such temperature and the pore structure collapsed upon heated. And as the calcinations proceeded longer, the pore size was enlarged and the small pores began to be sintered, as observed that the pore diameter increased to 8 nm for 1 hour heating. Therefore, slowly decomposition at lower temperature was critical for obtaining highly porous nickel oxide, where the best result was achieved at calcinations at 300 °C for 3 hour and the highest surface area obtained was 382.56 m²/g with an average pore diameter of 7.08 nm.

Table 6.1. Surface properties of calcined nickel oxides

Samples	BET surface area (m ² /g)	Average pore diameter (nm)
NiO (300 °C 1h)	318.29	6.95
NiO (300 °C 2h)	382.23	7.08
NiO (300 °C 3h)	382.56	7.08
NiO (360 °C 20min)	361.82	7.47
NiO (360 °C 40min)	357.57	7.48
NiO (360 °C 60min)	341.25	8.09

Figure 6.6 shows the SEM images of mesoporous NiO calcined at 300 °C for 3 hours. The particles preserved the texture and size of the as-synthesized nickel hydroxide. The macropores and mesopores could be observed clearly on the right figure. Obviously, such porous structures are ideal adsorption sties for hydrogen storage.

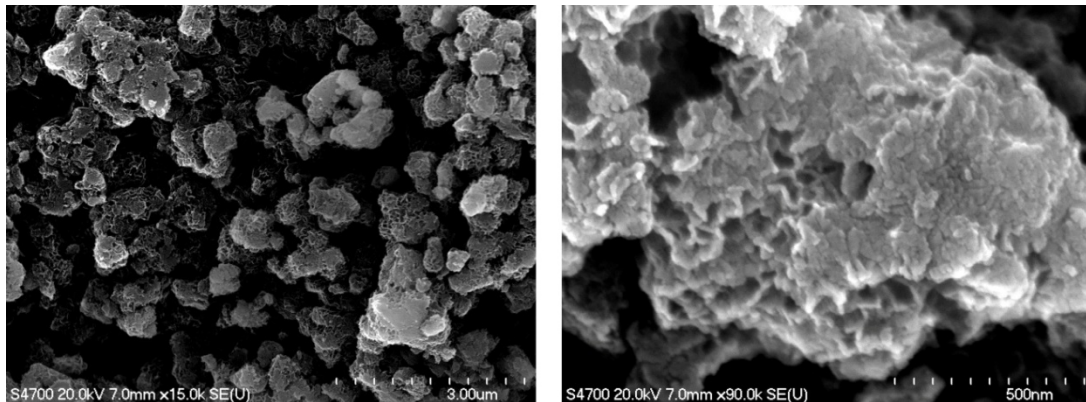


Figure 6.6. FE-SEM images of NiO calcined at 300 °C for 3 hours

6.3.1.2 Hydrogen storage of nickel oxide

6.3.1.2.1 Hydrogen storage of electric field assisted porous nickel oxide

Hydrogen adsorption isotherms at 298 K for porous NiO (calcined at 300 °C for 3 hours) and NiO+PMN-PT are shown in Figure 6.7. The porous nickel oxide had a total hydrogen capacity of about 0.08 wt% at 135 bars. The shape of the adsorption curve was almost a linear line, which indicated the absences of a saturation point and suggested that further increase in capacity could be realized at pressure greater than 135 bars. The curve also presented a typical physisorption type caused by the low interaction force of the hydrogen molecule and nickel oxide surface. By simply embedding an electric field generating material PMN-PT into the porous nickel oxide, the

hydrogen uptake had been remarkably enhanced to 0.11 wt% at 135 bars, which was about 37.5% increase. It should be noted that the PMN-PT alone had almost zero adsorption at the same condition. Such significantly enhancement was clearly the evidence of the assisted increase from the PMN-PT generated electric field. Moreover, it is noted that the magnitude difference between the two lines continuously increased from 0 bar to 60 bar, and became almost constant at pressure higher than 60 bars. This implied that there was a saturation point from where further enhancement of the electrical strength had no effect on the hydrogen interaction.

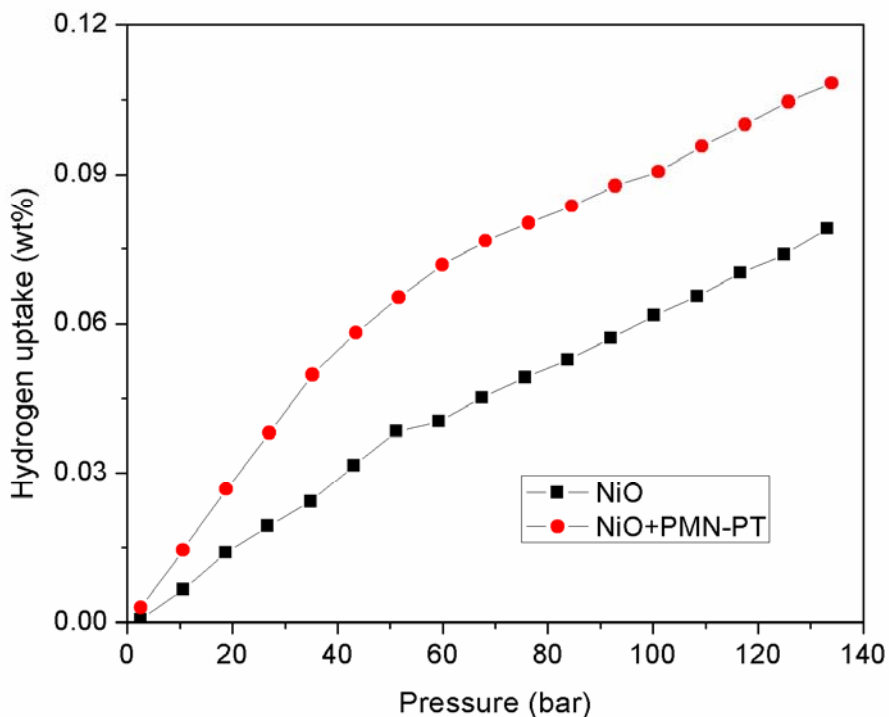


Figure 6.7. Hydrogen adsorption isotherms at 298 K for NiO samples

6.3.1.2.2 Hydrogen storage of electric field assisted spillover on nickel oxide

Hydrogen spillover has become a hot topic in hydrogen storage research in recent years. It is believed that the hydrogen molecules would dissociate into atomic hydrogen when they are in contact or closed range with the catalytic surface. The atomic hydrogen then spills over to the adsorbent surface via surface diffusion [16]. Spillover has been successfully used for hydrogen storage in carbon materials [16], metal-organic frameworks [17-21], and porous inorganic materials [22]. The bonding between atomic hydrogen and the materials surface is much stronger than that of molecule hydrogen so that significant adsorption could be realized especially at room temperature. The possible drawbacks are the blocking of the pores by the deposited catalysts and also the decreased surface area for adsorption.

The nitrogen adsorption/desorption of the platinum deposited porous nickel oxide (calcined at 300 °C for 3 hours) is shown in Figure 6.8. After deposition of platinum by wet chemical method, the nickel oxide still maintained its mesoporous characteristics which were determined from the hysteresis loop of the adsorption/desorption isotherms and the pore size distribution (insert). However, the total surface area dropped to 243.29 m²/g, a nearly 35% decrease from the calcined product.

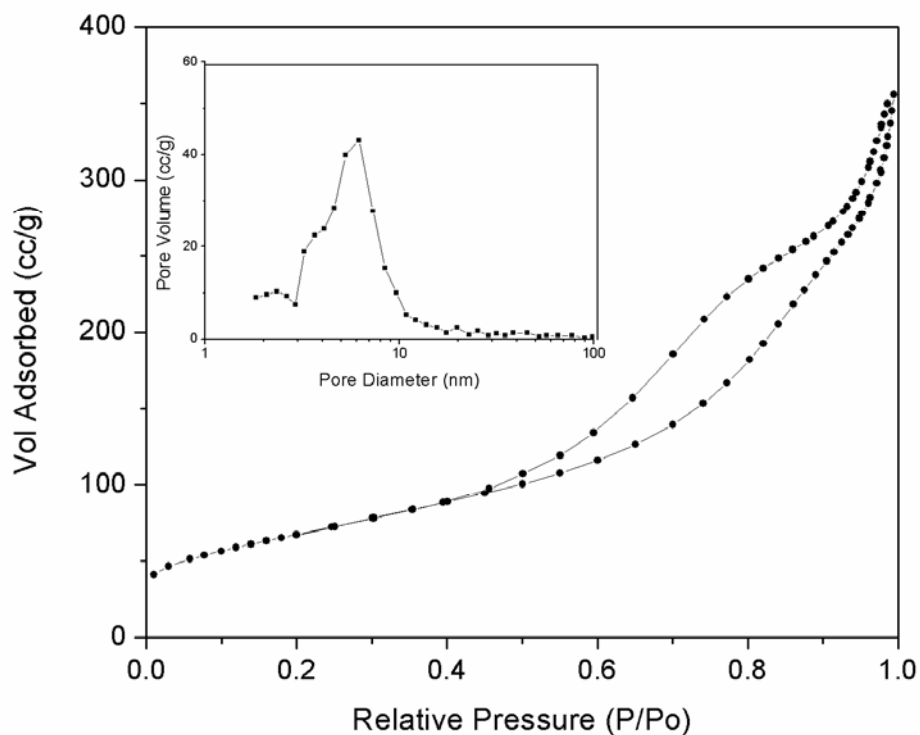


Figure 6.8. Nitrogen adsorption/desorption isotherms of Pt deposited porous NiO, insert: BJH pore size distribution obtained by desorption isotherms

Figure 6.9 shows the FE-SEM images and the EDS analyzed elemental compositions of the platinum deposited nickel oxides. The tiny spheroids on the surface were mainly deposited platinum particles at the size of about 50-100 nm. Such small particle size made the platinum very reactive where the hydrogen dissociation would easily occur on the platinum surface. The EDS spectrum shows that the deposited platinum is about 20 wt%.

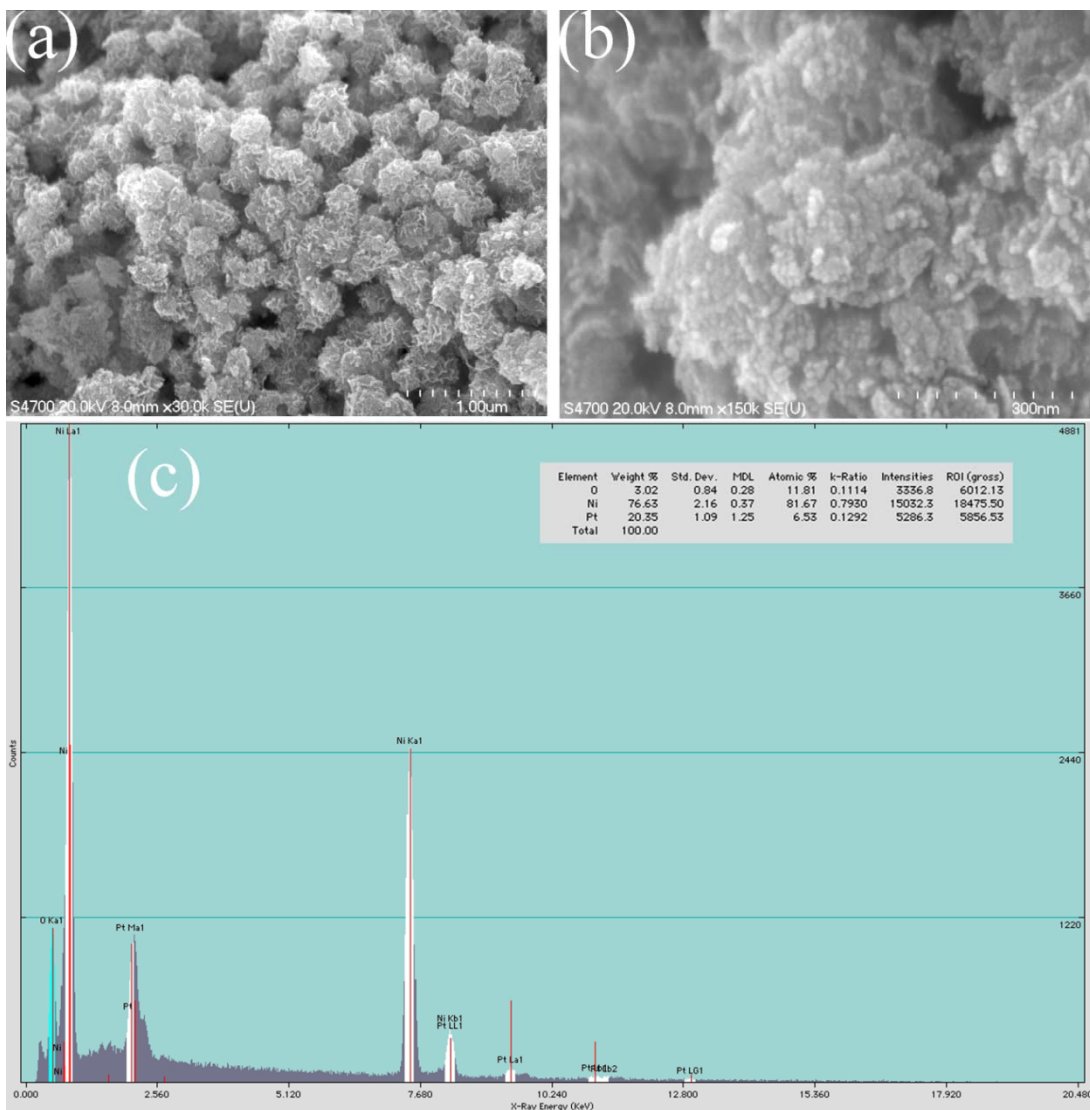


Figure 6.9. FE-SEM images of platinum deposited porous nickel oxide (a)(b), and EDS spectrum (c)

The hydrogen adsorption curves of the Pt deposited NiO at 298 K are shown in Figure 6.10. Hydrogen spillover on nickel oxide improved the uptake to 0.22 wt% at 120 bars, which was about 3 times the capacity of the nickel oxide without platinum. No apparent saturation point was approached for the Pt deposited sample and the adsorption trend followed a linear line where further increase in total capacity could be expected at higher pressure. Under the PMN-PT generated electric field, the total hydrogen uptake has been tremendously improved. It reached about 0.31 wt% at 120 bars, which was another 50 % increase over the spillover nickel oxides. There was also no apparent saturation value for adsorption. The results also proved that the external electric field imposed on the nickel oxide could also attract atomic hydrogen and enhance the bonding interaction. The enhancement from PMN-PT was small at low pressure whereas it increased as the pressure increased. At about 20 bars, the magnitude of the

enhancement became constant indicating that the significant effect of the electric field on atomic hydrogen adsorption only occurred at low pressure. By combining the enhancement from hydrogen spillover and PMN-PT generated electric field, the total capacity has been increased remarkably by a factor of 4.

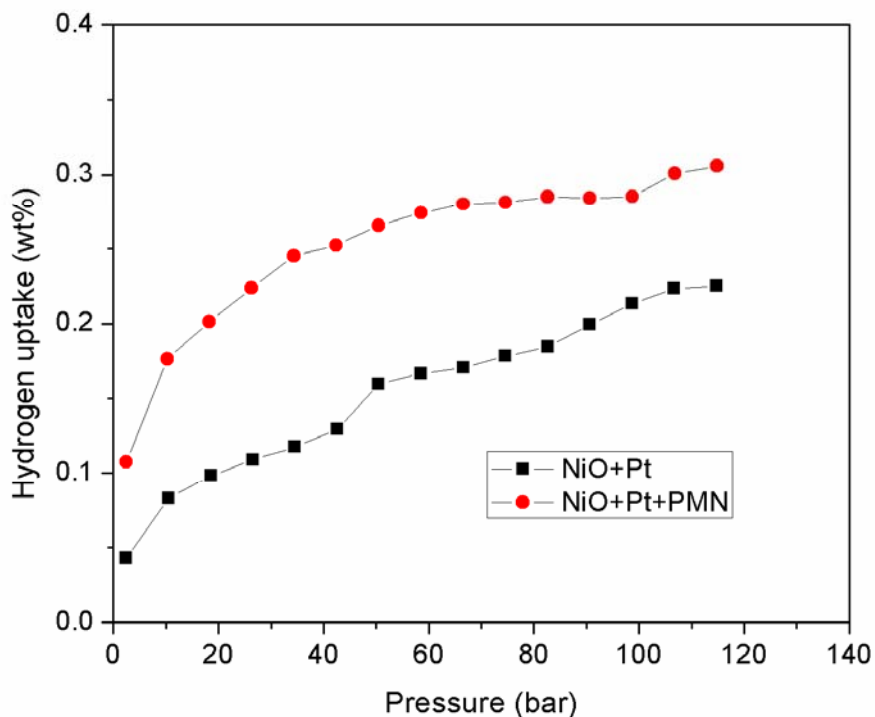


Figure 6.10. Hydrogen storage of Pt deposited porous NiO and enhancement from the PMN-PT

The computer simulation of optimized nickel oxide clusters is shown in Figure 6.11. The nominal charge for nickel oxide is 2; however, the point charge used to reproduce the lattice parameter is 1.2648. Carefully selecting the point charge value is critical to have reliable modeling results.

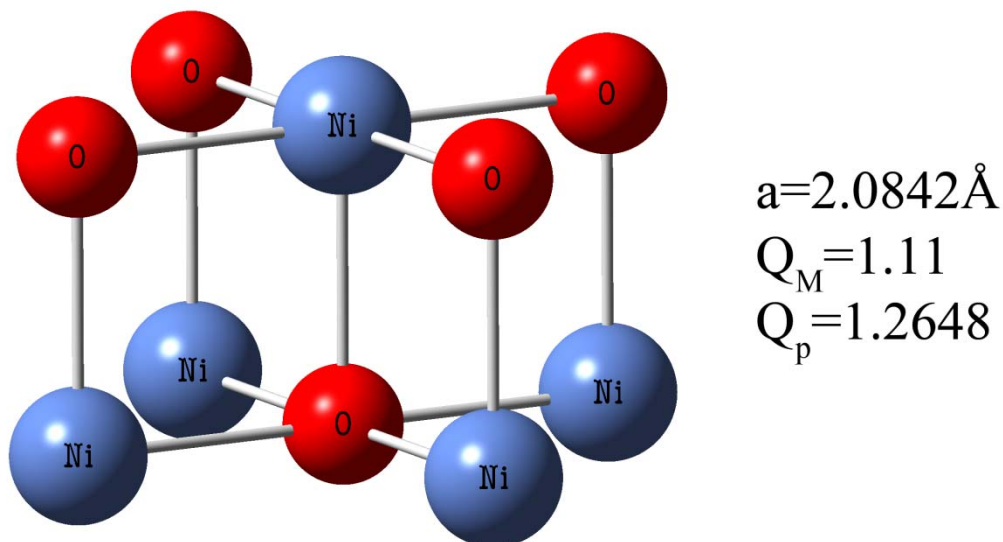


Figure 6.11. Optimized Ni_5O_5 clusters in $13 \times 13 \times 13$ point charges, where a is the lattice parameter, Q_M is the average Mulliken charge, and Q_p is the magnitude of the point charge

The modeling work of hydrogen adsorption on nickel cation site of nickel oxides under different electrical field strength is shown in Figure 6.12. Hydrogen molecules could be adsorbed onto the nickel site of nickel oxide with a small binding energy. When the electrical field is applied, the hydrogen molecules are more perturbed and attracted closer to the nickel atom, indicating a stronger interaction. The effects increase consistently with the increasing of electrical field strength, where the highest binding energy at 0.015 au increased three times. These remarkable phenomena are in good agreement with the experimental observations.

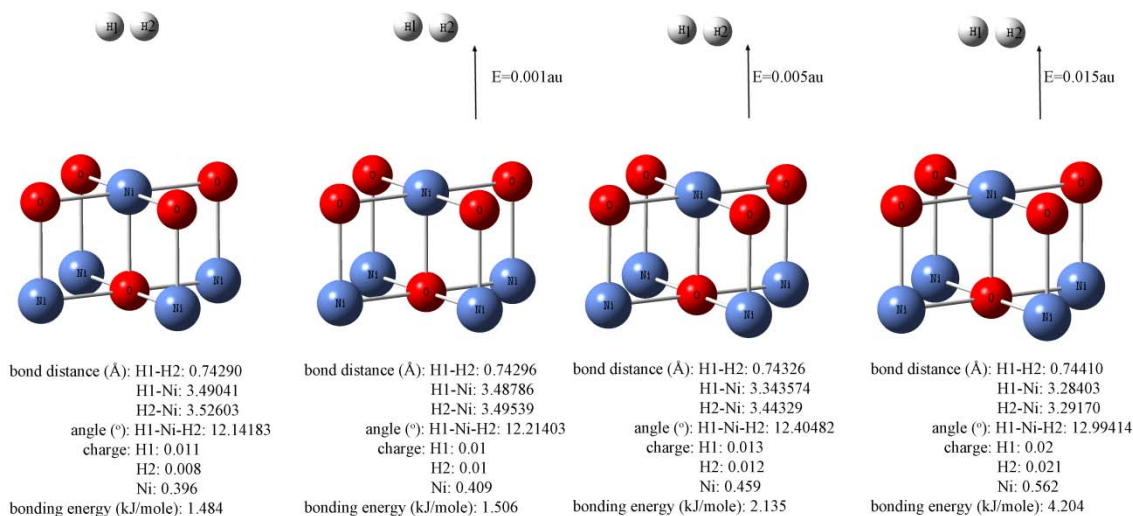


Figure 6.12. Optimized geometry of hydrogen adsorbed on nickel site under the influence of electric field

An explanation could be well obtained from the DOS analysis of atom orbital. Figure 6.13 shows the DOS spectrum of hydrogen orbital. Free hydrogen molecules only have one peak at around -12 eV, indicating the localization of the electrons. When they are adsorbed onto nickel site, there are two more peaks occurring at energy between -10 to -2 eV, indicating part of the electrons moving to higher energy state. Such electrons overlap with the electrons from nickel outer shell so that the adsorption bonding is formed. When an electrical field was applied, there were more peaks presented due to more electron overlapping and better interaction between hydrogen and nickel. The overall effects increased with the increasing of electrical strength, which explained why the bonding energy increased consistently with the field strength.

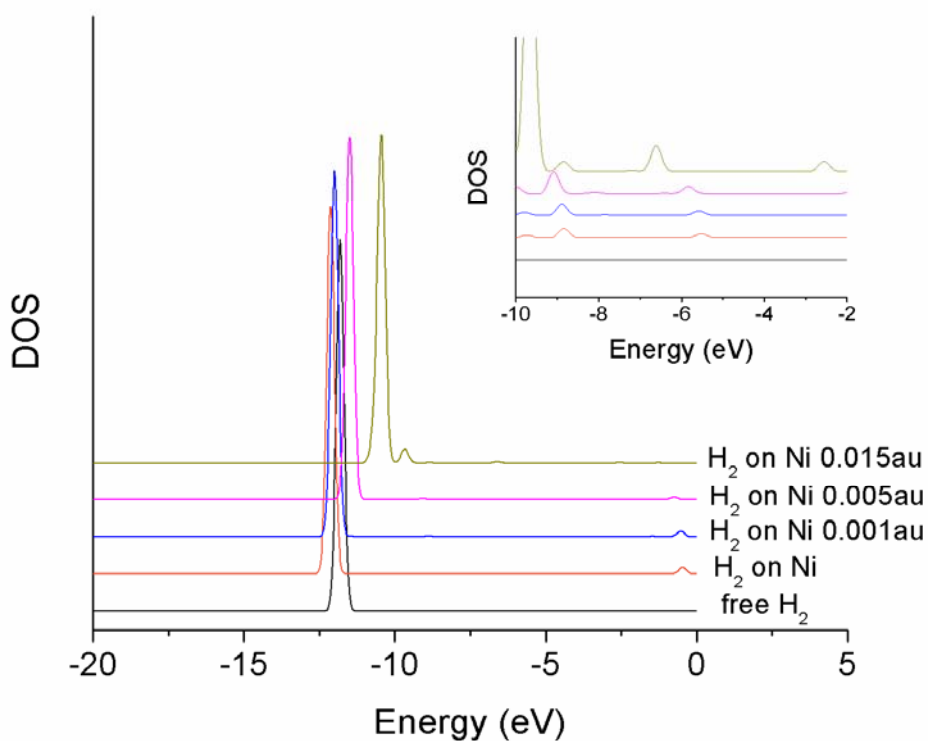


Figure 6.13. DOSs of orbital of hydrogen molecules which adsorbed on nickel site of the nickel oxide under the applied electric field, insert: higher magnification of the DOSs between -10 to -2 eV

The same modeling work was performed on oxygen site of the nickel oxide. Figure 6.14 shows that the same trend occurs on oxygen site. The bonding energy increased with the increasing strength of the electric field. The DOS analysis (Figure 6.15) also showed that the electron clouds were pulled over to the oxygen site, and the bonding was formed due to the overlapped electrons.

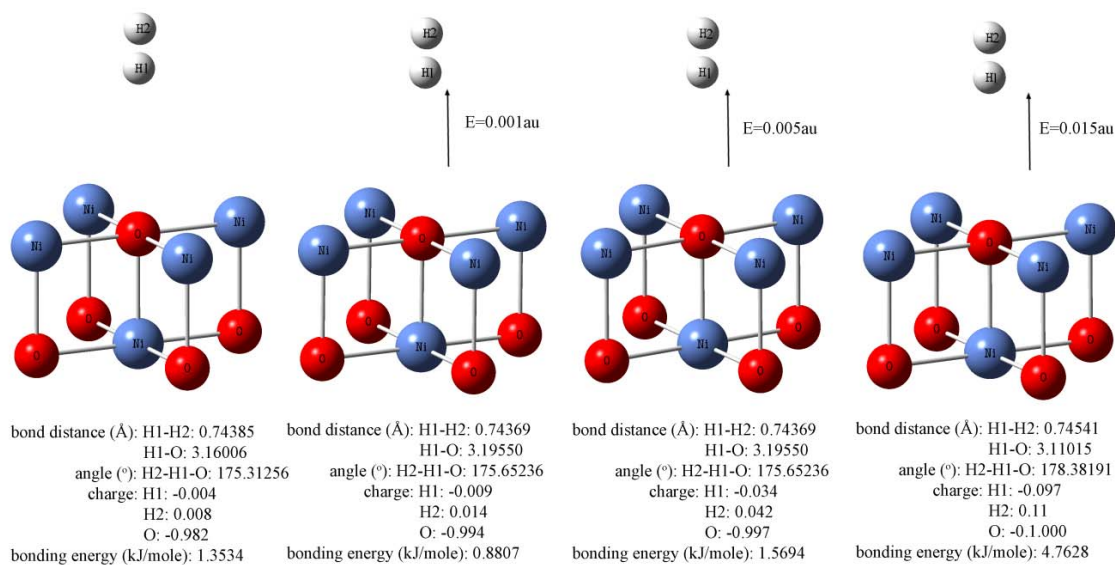


Figure 6.14. Optimized geometry of hydrogen adsorbed on oxygen site under the influence of electric field

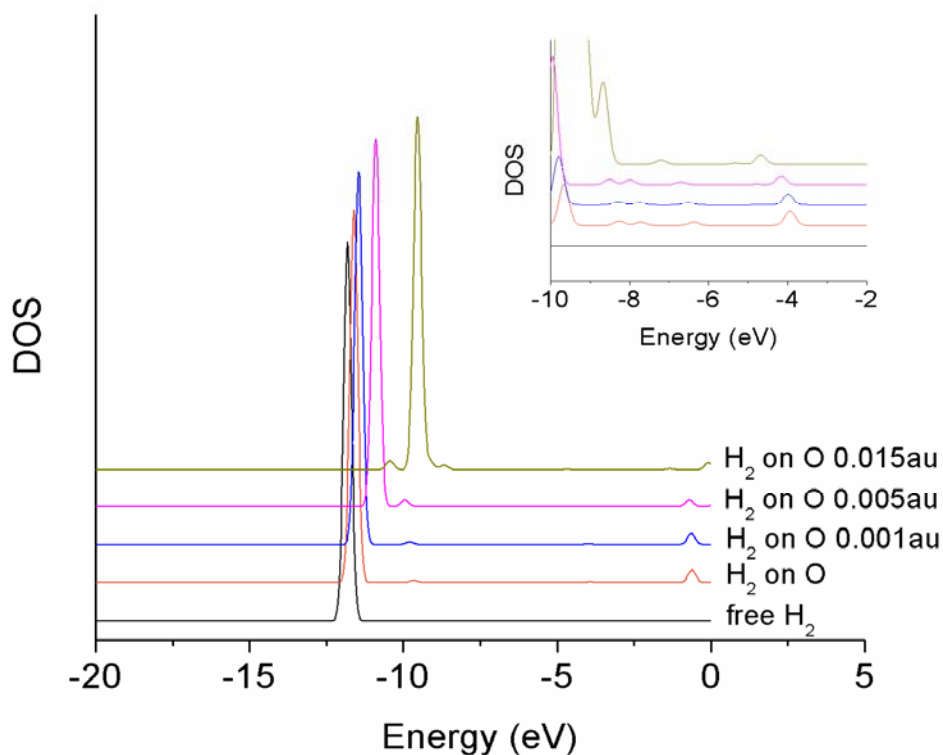


Figure 6.15. DOSs of orbital of hydrogen molecules which adsorbed on oxygen site of the nickel oxide under the applied electric field, insert: higher magnification of the DOSs between -10 to -2 eV

6.3.2 Porous magnesium oxides

6.3.2.1 Characterization of as synthesized oxides

Figure 6.16 shows the XRD pattern of the as-synthesized magnesium oxide. The pattern is a good match of the magnesium carbonate hydroxide hydrate which is also called hydromagnesite. The compound was formed by the reaction of magnesium cations and the carbon dioxides and hydroxide ions from the hydrolysis of urea. Upon heating, the decomposition of the compound caused carbon dioxide and water vapor to be developed and the porous structures to be generated.

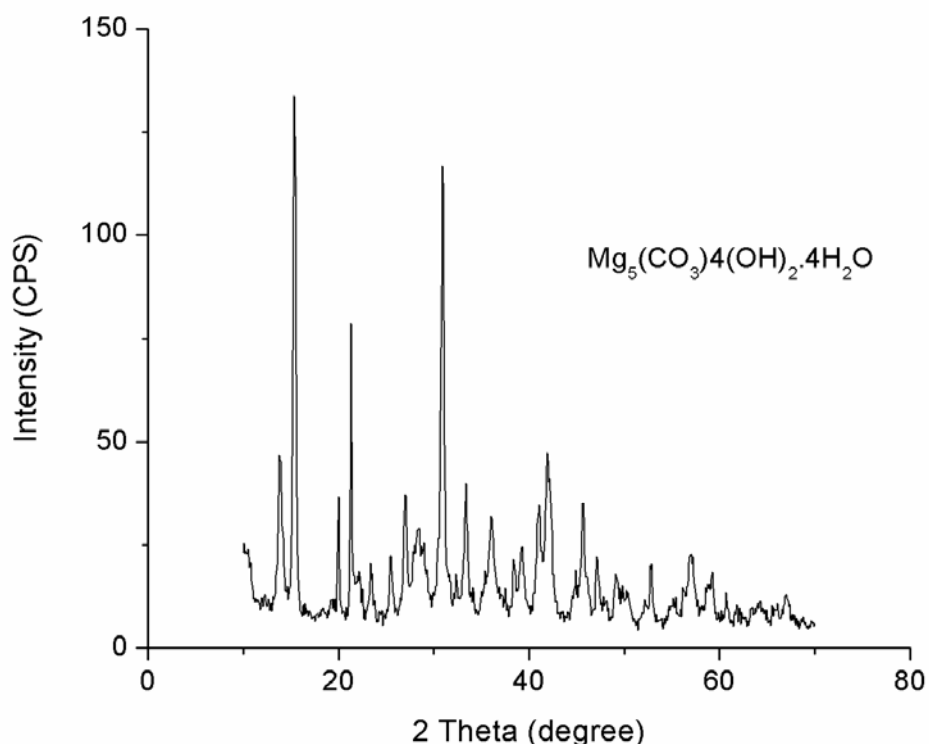


Figure 6.16. XRD pattern of as-synthesized hydromagnesite

Figure 6.17 shows the DTA curve in air of the as-synthesized hydromagnesite. A wide peak was presented between 200 °C and 350 °C and a sharp peak was observed between 400 °C and 500 °C, which corresponded to the dehydration reaction and decarbonization reaction of the hydromagnesite, respectively. As with the nickel hydroxide, low calcinations temperature of 400 °C and long time period of 3 hours were selected to obtain the porous product with the highest surface area.

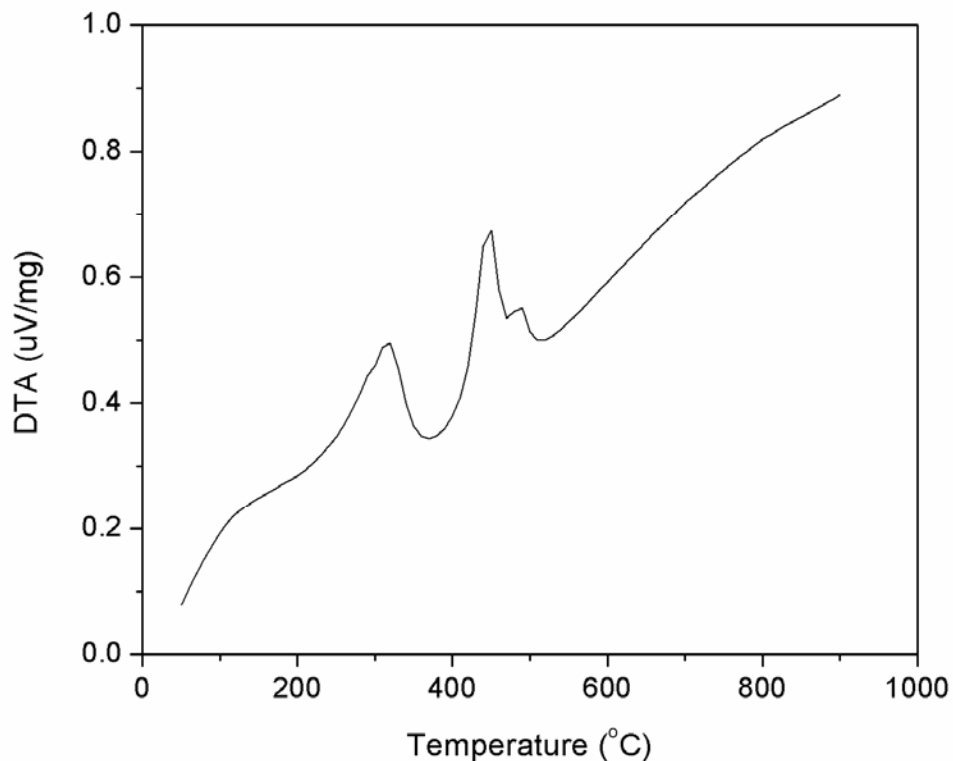


Figure 6.17. DTA curve of as-synthesized hydromagnesite

Representative x-ray diffraction pattern of the calcined product is shown in Figure 6.18. It clearly represented the single phase of only magnesium oxide with no other impurities, indicating that the decomposition reaction was complete. The significant peak broadening revealed that the calcined particles have small grain size.

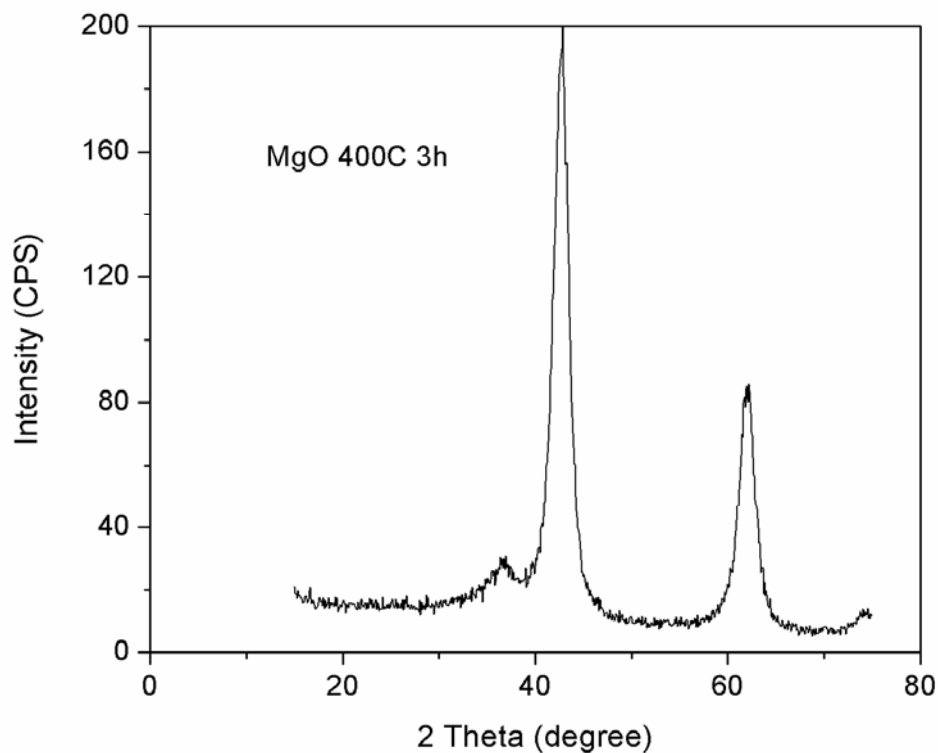


Figure 6.18. XRD pattern of calcined magnesium oxide

The corresponding morphology was examined by FE-SEM. As shown in Figure 6.19, the particles had nano-plate structures, which were stacked together irregularly. The higher magnification image, as in Figure 6.19(b), revealed that each particle looked like well defined nano-platelet with a thickness of 30-50 nm and a lateral dimension of around several microns. More details about developed pore structures are presented in Figure 6.19(c) and 6.19(d), where obvious pores and cracks generated by calcinations were well observed. Various macropores and mesopores revealed that the product was highly porous.

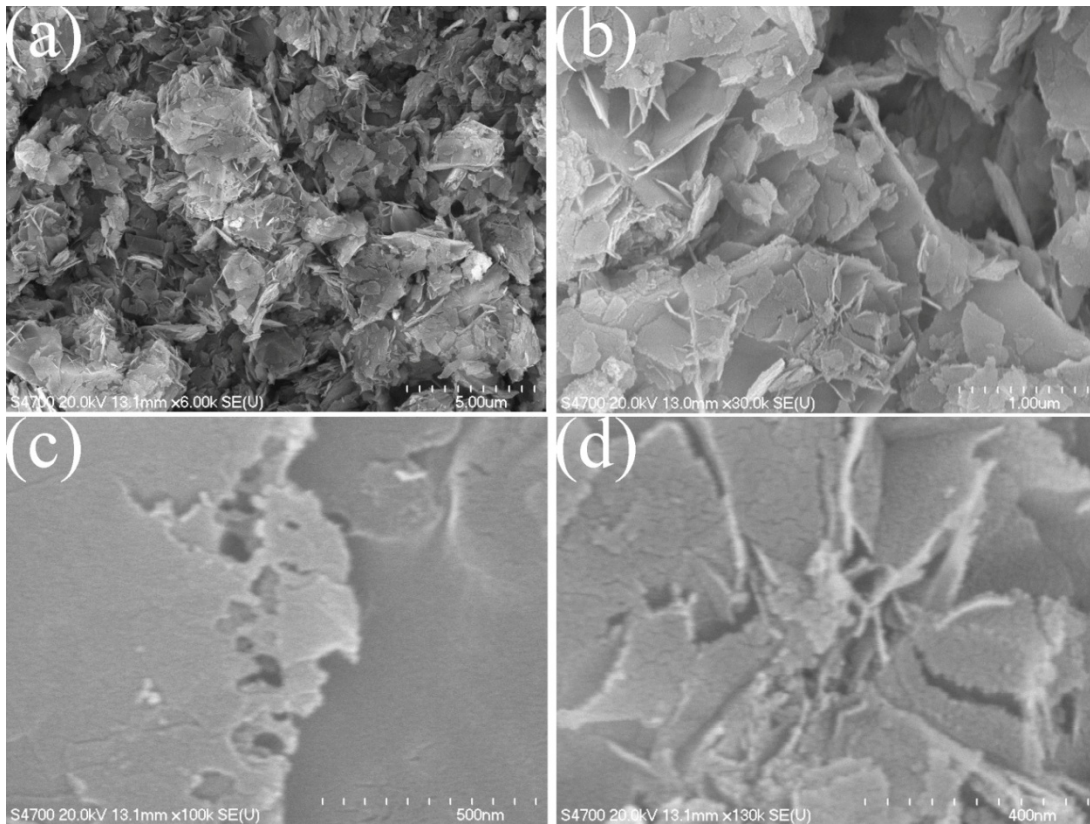


Figure 6.19. FE-SEM images of MgO calcined at 400 °C for 3 hours

Nitrogen adsorption/desorption isotherms and BJH pore size distributions are shown in Figure 6.20. The significant hysteresis loop of the isotherms indicated that the product had mesopore structure. The pore size distribution as calculated by BJH desorption isotherms confirmed that the calcined MgO was mainly composed of small mesopores with average pores diameter of 3.87 nm. The total surface area and pore volume are 363.59 m²/g and 0.35 cc/g, respectively. Such surfactant directed grown porous magnesium oxide had much higher surface area than other porous MgO obtained by hydrothermal treatment [21], direct dehydration [22], and wet precipitation methods [23].

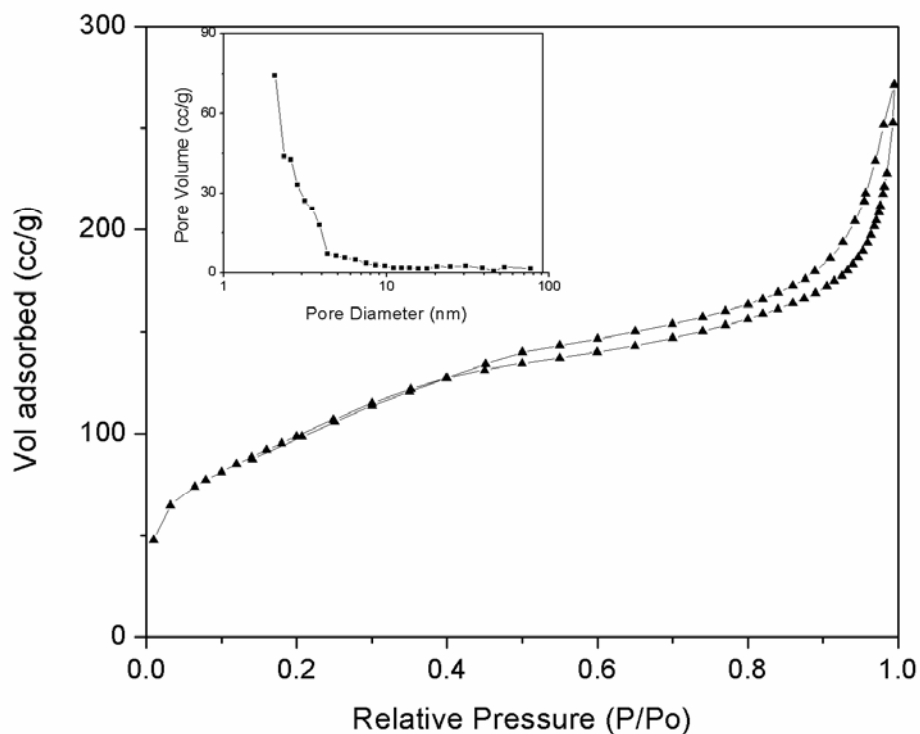


Figure 6.20. Nitrogen adsorption/desorption isotherms of the MgO product calcined at 400°C for 3 hours, insert: BJH pore size distribution obtained from desorption isotherms

6.3.2.2 Hydrogen storage of electric field assisted porous magnesium oxide

The hydrogen uptake curves of porous magnesium oxide at 298 K are shown in Figure 6.21. The curve followed a linear trend indicating that no apparent saturation point was observed. It had very low hydrogen uptake at pressure below 30 bars whereas the uptake increased vigorously when the pressure reached over 30 bars. The optimum adsorption at 90 bars reached about 0.2 wt%. With the assistance from the PMN-PT, the hydrogen uptake had improved remarkably to 0.25 wt% at 90 bars, about 25 % increase. The curve still preserved the linear trend and no saturation was expected. The enhancement increased with the increasing of hydrogen pressure and at over 60 bars, the magnitude of the enhancement became almost constant indicating the optimum effects of the PMN-PT generated electric field. In order to better understand the effects from the external electric field, DFT computer simulation was carried out on the Mg_5O_5 clusters embedded in point charge.

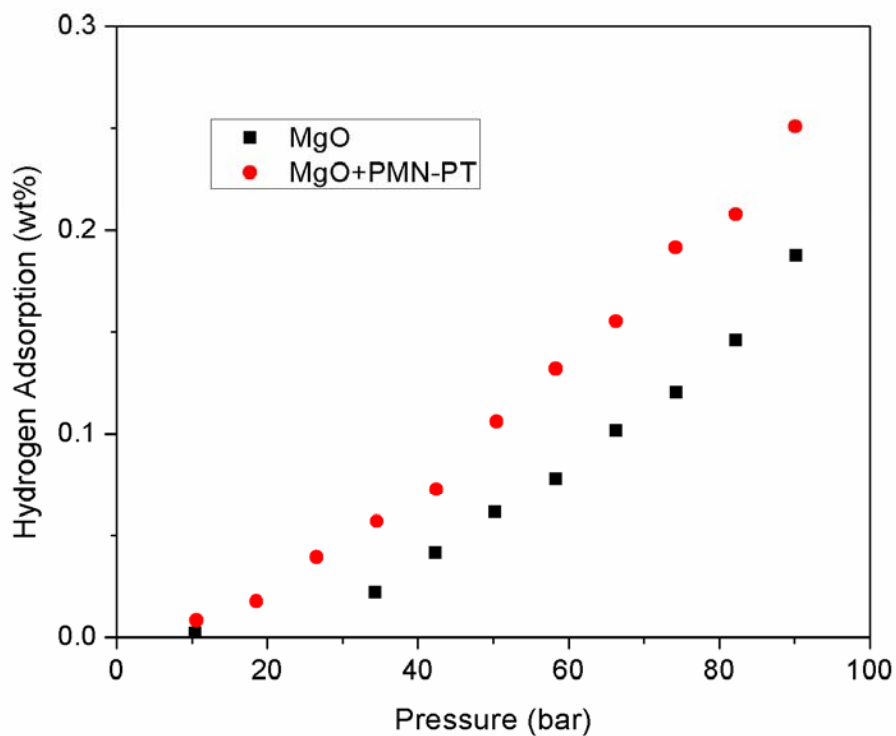


Figure 6.21. Hydrogen adsorption at 298 K for the porous MgO sample and MgO+PMN-PT sample

Figure 6.22 shows the optimized geometry of Mg_5O_5 clusters embedded in $13 \times 13 \times 13$ point charges. The surrounding point charges were found to be 0.706 to reproduce the lattice parameter of the MgO crystal. The cluster was then moved to the point charge surface to calculate the hydrogen adsorption interactions.

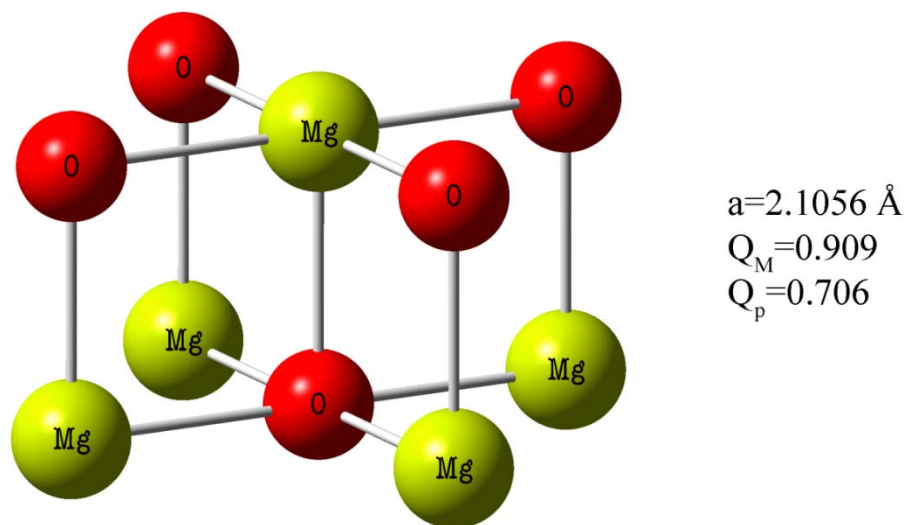


Figure 6.22. Optimized Mg_5O_5 clusters in $13 \times 13 \times 13$ point charges, where a is the lattice parameter, Q_M is the average Mulliken charge, and Q_p is the magnitude of the point charge

Figure 6.23 shows the optimized geometry of hydrogen adsorption on magnesium site in magnesium oxide without and under the external electric field.

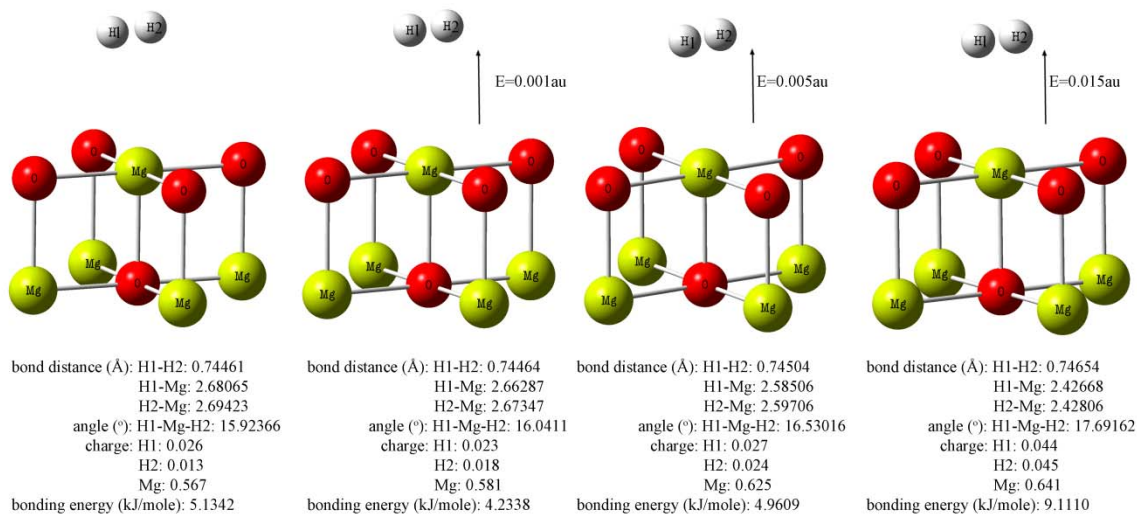


Figure 6.23. Optimized geometry of hydrogen adsorbed on magnesium site under the influence of electric field

Without the external electric field, the H-H distance was perturbed about 0.00182 \AA (recall from chapter six that the free hydrogen molecule distance is 0.74279 \AA). The charges on hydrogen

atoms were positive indicating that the electron cloud was pulled to the magnesium site. The electric field was applied along vertical direction, as described in the figure. By supplying a small electric field 0.001 au, the H-H distance was further affected that the bonding energy increased. With each increase of the electric field strength, hydrogen molecules became more perturbed along with the total binding energy. At electric field of 0.015 au, the charges on hydrogen became positive 0.044, which was about two times of the adsorbed hydrogen without electric field.

From calculations of the partial density of states (DOS), the nature of the chemical bonding in the studied system could be visualized. Figure 6.24 shows the calculated DOSs of s orbital of hydrogen molecules that adsorbed on the magnesium site of MgO under the different electric field. For the free hydrogen molecules, there was only one peak which indicated the localization of the s orbital. As the hydrogen molecule adsorbed onto the magnesium site, a small peak around -6 eV appeared. When the applied electric field strength increased, more peaks emerged and the intensity of the peaks increased. The appearance of the new peaks indicated the overlap of electrons between hydrogen and magnesium. The trend demonstrated that more electrons overlapping occurred as the field strength increased.

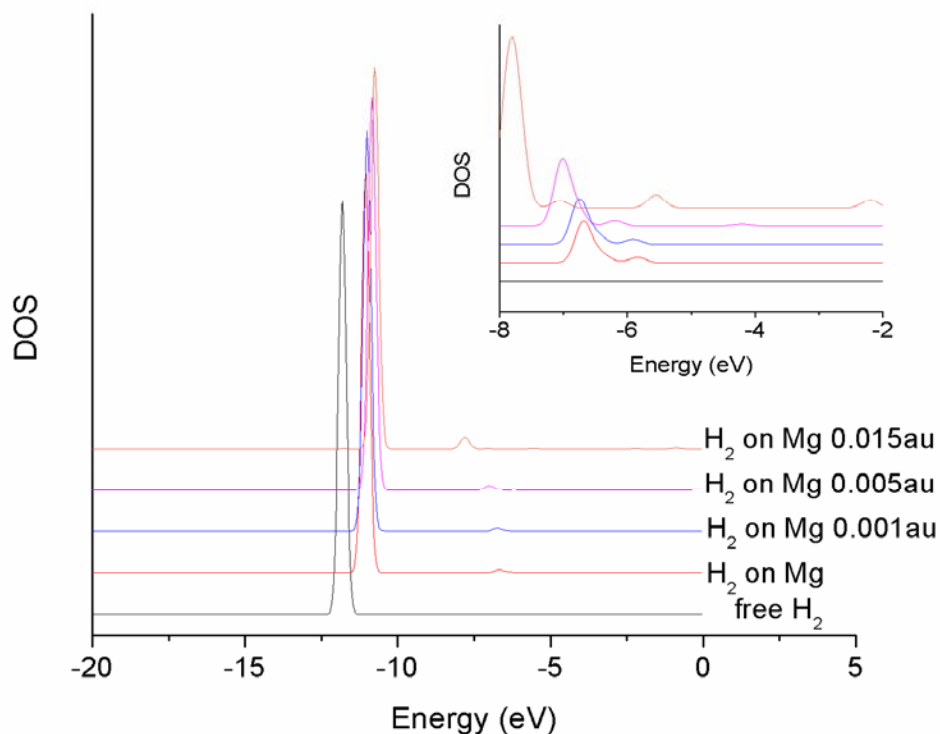


Figure 6.24. DOSs of s orbital of hydrogen molecules which adsorbed on magnesium site of the magnesium oxide under the applied electric field, insert: higher magnification of the DOSs between -8 to -2 eV

Figure 6.25 shows a schematic figure of the electron movement under the electric field. With the applied field, the electron clouds of hydrogen molecules were more strongly pulled over the magnesium site, as was evident from the resulting high positive charges of the hydrogen atoms. Therefore, the hydrogen electrons overlapped with the magnesium electrons so that total bonding strength increased.

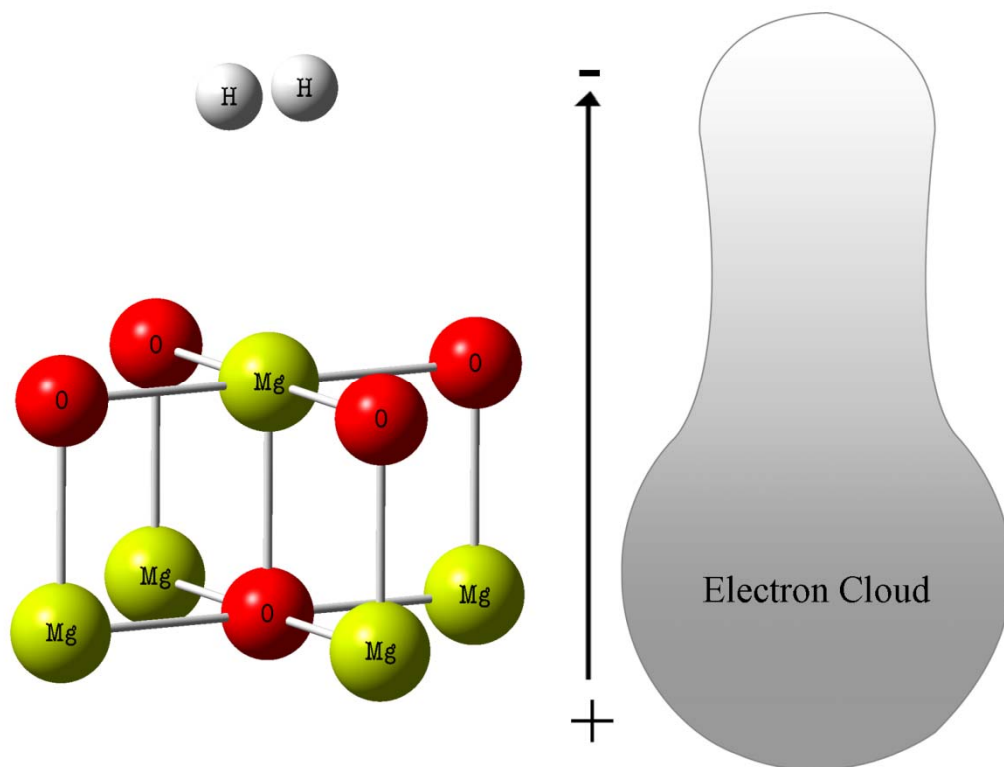


Figure 6.25. Schematic of the shape of the electron cloud under external electric field

The same calculation was carried out on the hydrogen adsorption on oxygen site of the MgO under various applied fields, as shown in Figure 6.26. The adsorption on oxygen site still followed end-on model. Without an electric field, the bonding energy was very small, only 0.5219 kJ/mole. However, as the field was applied, the bonding energy increased consistent with the increasing of the electric field strength. The H-H bond length, H-O distance, and charges also supported this observation. Furthermore, the alignment of hydrogen molecule became more vertical toward the oxygen atom when the field strength became larger. Also large intrinsic dipole moment of the hydrogen molecule was generated by the electric field, as demonstrated by the different signs of charges on two hydrogen atoms.

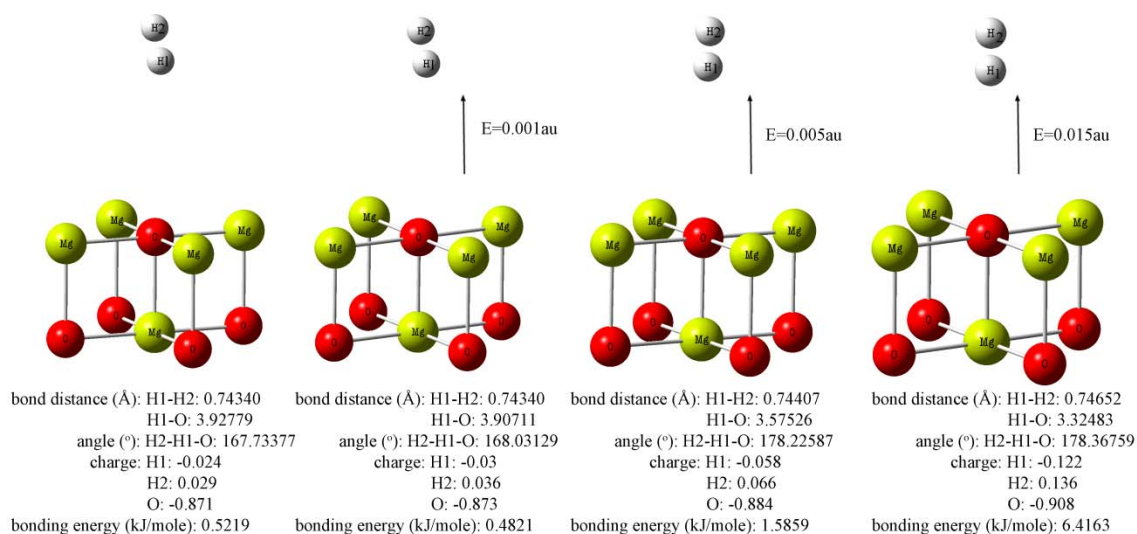


Figure 6.26. Optimized geometry of hydrogen adsorbed on oxygen site under the influence of electric field

Similar to what happened on magnesium site, the electric field had the potential to cause the electrons from hydrogen molecules and oxygen ion to be overlapped. As from Figure 6.27, more peaks were observed under higher electric field strength, whereas the intensity of the peaks followed the same trend.

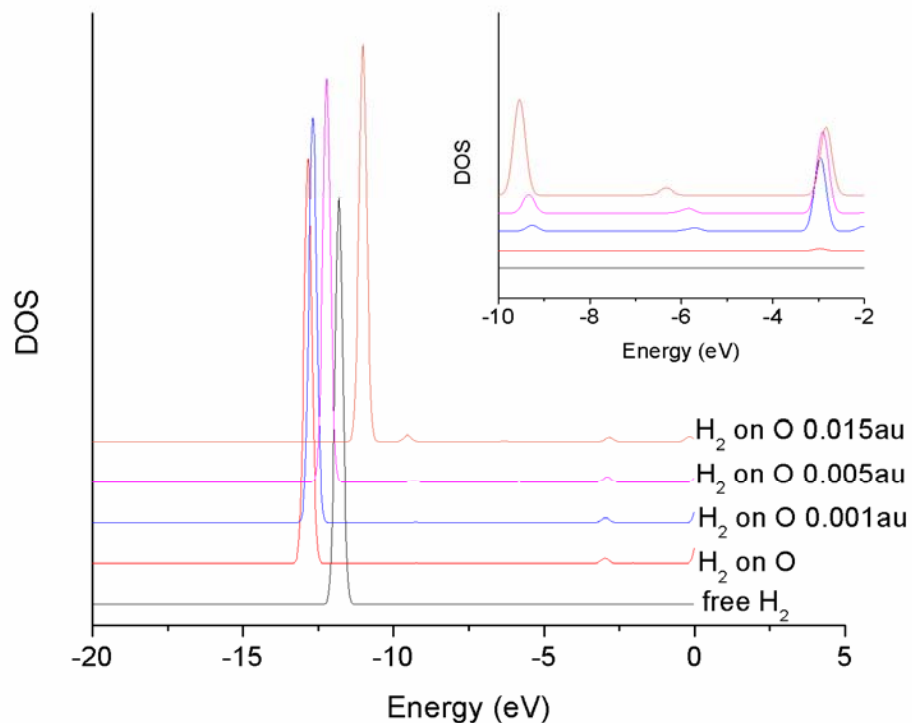


Figure 6.27. DOSs of s orbital of hydrogen molecules which adsorbed on oxygen site of the magnesium oxide under the applied electric field, insert: higher magnification of the DOSs between -10 to -2 eV

6.4 Summary

The adsorption of hydrogen on porous nickel oxides and magnesium oxides under an external electric field has been quantitatively studied both experimentally and theoretically. The results demonstrated that the storage enhancement from an electric field was remarkable. About 35% and 25% increase could be achieved in nickel oxides and magnesium oxides, respectively. Moreover, by combining hydrogen spillover and electric field effects, the storage capacity could be enormously enhanced about 400%. Computer simulation had consistent results with the experimental observations and revealed that the electric field pulled hydrogen electrons to the adsorbent sites causing electron overlapping, which tremendously increased the bonding energy.

6.5. Section 6 References

- [1] Y. H. Hu and E. Ruckenstein, *Advances in Catalysis*, 48 (2004) 297-345, "Catalytic conversion of methane to synthesis gas by partial oxidation and CO₂ reforming".
- [2] Z. P. Guo, L. Yuan, K. Konstantinov, Z. G. Huang, H. K. Liu, *Materials Letters*, 60 (2006) 3891-3894, "Preparation of spherical clusters of metal oxide nanorods and their hydrogen storage behavior".
- [3] X. Hu, B. O. Skadtchenko, M. Trudeau, and D. M. Antonelli, *Journal of the American Chemical Society*, 128 (2006) 11740-11741, "Hydrogen storage in chemically reducible mesoporous and microporous Ti oxides".
- [4] Y. Wang, J. Cao, S. Wang, X. Guo, J. Zhang, H. Xia, S. Zhang, and S. Wu, *Journal of Physical Chemistry C*, 112 (2008) 17840-17808, "Facile synthesis of porous #-FeO nanorods and their application in ethanol sensors".
- [5] K-W. Nam, K-B. Kim, *Journal of the Electrochemical Society*, 149 (2002) A346-A354, "A study of the preparation of NiO_x electrode via electrochemical route for supercapacitor applications and their charge storage mechanism".
- [6] Venkat Srinivasan and John W. Weidner, *Journal of the Electrochemical Society*, 147 (2000) 880-885, "Studies on the capacitance of nickel oxide films: effect of heating temperature and electrolyte concentration".
- [7] Q. Huo, D. I. Margolese, G. D. Stucky, *Chemistry of Materials*, 8 (1996) 1147-1160, "Surfactant control of phases in the synthesis of mesoporous silica-based materials".
- [8] S. Banerjee, A. Santhanam, A. Dhathathreyan, and P. M. Rao, *Langmuir*, 19 (2003) 5522-5525, "Synthesis of ordered hexagonal mesostructured nickel oxide".
- [9] Piezoelectric, Wikipedia, <http://en.wikipedia.org/wiki/Piezoelectric>
- [10] Piezoelectric materials, <http://www.piezomaterials.com/>
- [11] W. Xing, F. Li, Z-F. Yan, G. Q. Lu, *Journal of Power Sources*, 134 (2004) 324-330, "Synthesis and electrochemical properties of mesoporous nickel oxide".
- [12] J. Zhang, X. Wang, C. Wu, H. Wang, B. Yi, and H. Zhang, *React. Kinet. Catal. Lett.*, 83 (2004) 229-236, "Preparation and characterization of Pt/C catalysts for PEMFC cathode: effect of different reduction methods".
- [13] M. Kim, J-N. Park, H. Kim, S. Song, W-H. Lee, *Journal of Power Sources*, 163 (2006) 93-97, "The preparation of Pt/C catalysts using various carbon materials for the cathode of PEMFC".
- [14] H. Kim, J-N. Park, W-H. Lee, *Catalysis Today*, 87 (2003) 237-245, "Preparation of platinum-based electrode catalysts for low temperature fuel cell".
- [15] N. M. O'Boyle, A. L. Tenderholt and K. M. Langner. *J. Comp. Chem.*, 29 (2008) 839-845, "cclib: A library for package-independent computational chemistry algorithms".
- [16] A. J. Lachawiec, G. Qi, and R. T. Yang, *Langmuire*, 21 (2005) 11418-11424, "Hydrogen storage in nanostructured carbons by spillover: bridge-building enhancement".

- [17] Y. Li, and R. T. Yang, *Journal of the American Chemical Society*, 128 (2006) 8136-8137, "Hydrogen storage in metal-organic frameworks by bridged hydrogen spillover".
- [18] Y-Y. Liu, J-L. Zeng, J. Zhang, F. Xu, and L-X. Sun, *International Journal of Hydrogen Energy*, 32 (2007) 4005-4010, "Improved hydrogen storage in the modified metal-organic frameworks by hydrogen spillover effect".
- [19] Y. Li, and R. T. Yang, *AIChE Journal*, 54 (2008) 269-279, "Hydrogen storage in metal-organic and covalent-organic frameworks by spillover".
- [20] Y. Li and R. T. Yang, *Journal of Physical Chemistry B*, 110 (2006) 17175-17181, "Hydrogen storage in low silica type X zeolites".
- [21] J. C. Yu, A. Xu, L. Zhang, R. Song, and L. Wu, *Journal of Physical chemistry B*, 108 (2004) 64-70, "Synthesis and characterization of porous magnesium hydroxide and oxide nanoplates".
- [22] M. H. Lee and D. G. Park, *Bull. Korean Chem. Soc.*, 24 (2003) 1437-1443, "Preparation of MgO with High Surface Area and Modification of Its Pore Characteristics".
- [23] J. Lv, L. Qiu, B. Qu, *Journal of Crystal Growth*, 267 (2004) 676-684, "Controlled growth of three morphological structures of magnesium hydroxide nanoparticles by wet precipitation method".

7. CHARGE ENHANCED HYDROGEN ADSORPTION ON ACTIVATED CARBON

7.1 Introduction

The hydrogen adsorption capacities in different materials have been reported, including the metal hydrides, metal organic frameworks, carbon nanotubes, carbon nanofibres and activated carbon, etc. [1–10]. Activated carbon receives special attention for hydrogen storage because of its high surface area nature, availability, low cost and unique surface interaction with H₂ gas molecules [11–12]. Hydrogen adsorption on activated carbon at moderate temperature is due to physical adsorption based on van der Waals force between adsorbent and adsorbate [13]. This interaction force is very weak at room temperature. As a result, significant storage can only be achieved at liquid nitrogen temperature.

Introducing an external electric field may have the potential to increase the interacting force and hence increase the hydrogen adsorbability. Two approaches can be utilized for the generation of external electric field. The first one is to utilize the piezoelectric material. The second one is to apply the field through a high voltage device.

7.2 Adsorption Enhancement using Piezoelectric Materials

7.2.1 Background

Piezoelectric materials can produce a voltage in response to an applied force. Under high hydrogen gas pressure, substantial voltage potential could be generated across the positive and negative sides of the piezoelectric materials. The single crystal PMN-PT (lead magnesium niobate - lead titanate) has been formulated to exhibit high piezoelectric coefficients, large electric-mechanical coupling coefficients, high dielectric constants and low dielectric losses [14, 15]. Embedding the PMN-PT into the activated carbon is a potential way to enhance the adsorption energy.

7.2.2 Experimental

7.2.2.1 Materials

Two activated carbon samples were used in the experiments as adsorbents for hydrogen storage. One was Norit A supra activated carbon (NAC) from Norit Corporate with BET surface area of 1836m²/g. The other was high surface area activated carbon (HAC) from Osaka Gas Co. LTD (Japan) with BET surface area of 3211 m²/g. The BET surface areas were analyzed using a Micromeritics ASAP2000 instrument.

Single crystal PMN-PT disks acquired from Morgan Electro Ceramics were used, 5 mm in length and width, and 1 mm in thickness. The chemical structural formula of PMN-PT is $(1-x)[\text{Pb}(\text{Mg}_{1/3}\text{Nb}_{2/3})\text{O}_3]$ and $x[\text{PbTiO}_3]$. The piezoelectric charge constant (d_{33}) of PMN-PT is 1200 to 2000 pC/N, which is provided by Morgan Electro Ceramics [17].

7.2.2.2 Hydrogen adsorption

Hydrogen adsorption experiments were carried out with a Hy-Energy's PCT Pro 2000 sorption equipment. This fully automated Sievert's-type instrument can run at maximum pressure of 170 bars. The positive side of the PMN-PT was covered by a non-conductive thin film of cured glue to prevent electron transfer. In the hydrogen adsorption measurements, the PMN-PT was embedded in the activated carbon and both were positioned in a glass reaction container. The glass container was placed in a stainless steel sample holder. In such arrangement, the electrons from the PMN-PT were not able to transfer to the outside, so the electric field could be preserved inside the activated carbon. The hydrogen storage properties of activated carbon with PMN-PT were measured at both room temperature (293K) and 77K. For the experiments to determine the hydrogen storage properties at 77K, the sample holder was immersed into liquid nitrogen carried in a Dewar vessel.

7.2.3 Results and discussion

The effects of PMN-PT on hydrogen adsorption of the HAC and NAC at room temperature were measured. The pressure for each test ranges from 0 to 90 bars. The results are illustrated in Figure 7.1, where the errors for these measurements are between 1% and 8% (see error bars in Figure 7.1) based on three repeated experiments. The error between adsorption data from repeated measurement on NAC with PMN-PT (8%) was higher than NAC (3%).

The results show that, at 90 bars and 293K, the hydrogen adsorption capacities of NAC and HAC are 0.506wt% and 0.668wt%, respectively. When PMN-PT is inserted, the hydrogen adsorption capacities are remarkably enhanced to 0.592wt% for NAC and 0.756wt% for HAC under the same pressure and temperature.

The enhancement of hydrogen adsorption due to the insertion of PMN-PT becomes obvious at pressures exceeding 15 bars and is more pronounced as the hydrogen pressure increased, as shown in Figure 1. Such a phenomenon was attributed to piezoelectric properties of PMN-PT. The relationship between a force applied to PMN-PT disk and the charge produced by the PMN-PT can be expressed by:

$$Q = - (d_{33}F) = - (d_{33}TA) \quad (1)$$

Where Q is generated charge, F is applied force, T is axial stress, and A is cross section of PMN-PT disk. The charges increase with the increase of the applied pressure.

Activated carbon is a conductive material. The charge generated from PMN-PT due to hydrogen pressure will accumulate at the surface of activated carbon. This may result in the polarization of nearby hydrogen molecules or even the dissociation of hydrogen molecules when the voltage is sufficiently high. By supplying enough electrical energy, the electron clouds of the hydrogen molecules could be attracted to the adsorbent site, where electron overlapping may occur. This in turn can remarkably enhance the adsorption energy.

Figure 7.2 shows the hydrogen adsorption increased amount by the insertion of PMN-PT. The results show that higher hydrogen pressure yield higher hydrogen adsorption increase. The increases of hydrogen adsorption capacity for both NAC and HAC due to the insertion of PMN-PT are about identical; both are 0.086wt% at 90 bars and 293K, as shown in Figure 7.2. This indicates that surface area difference between the two samples has essentially little effect on the amount of adsorption enhancement. The hydrogen adsorption enhancement depends primarily on the charge from PMN-PT. Large charge population under high hydrogen pressure yields high hydrogen adsorption enhancement.

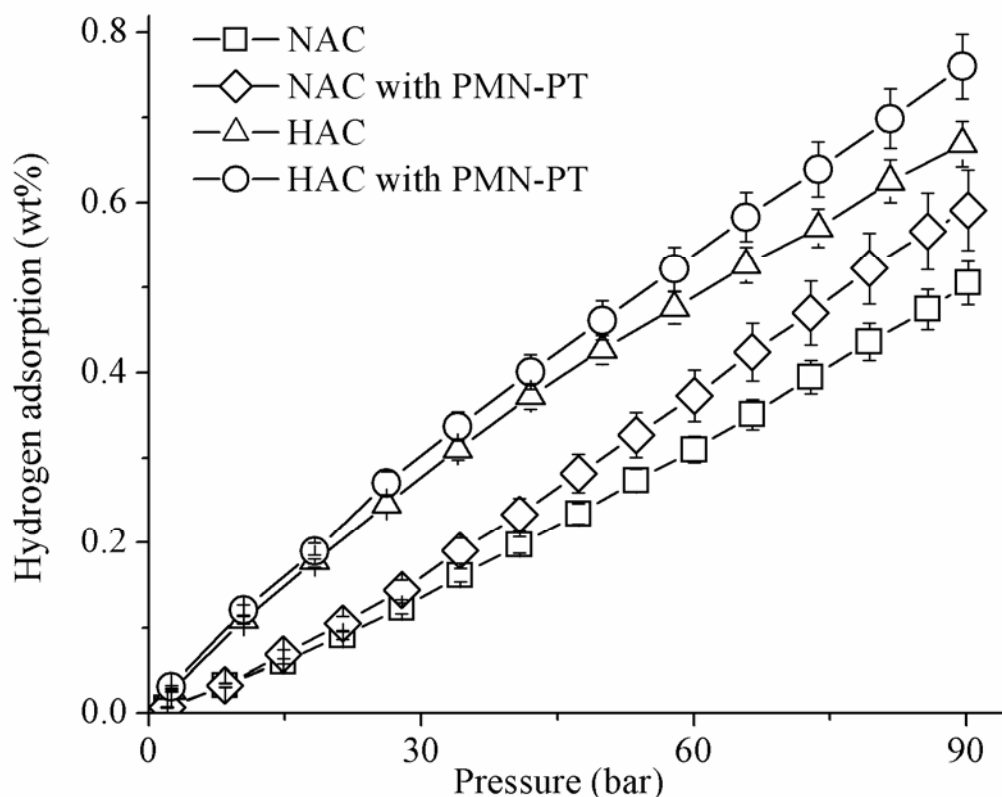


Figure 7.1. PMN-PT effect on H₂ adsorption of NAC and HAC at 293K

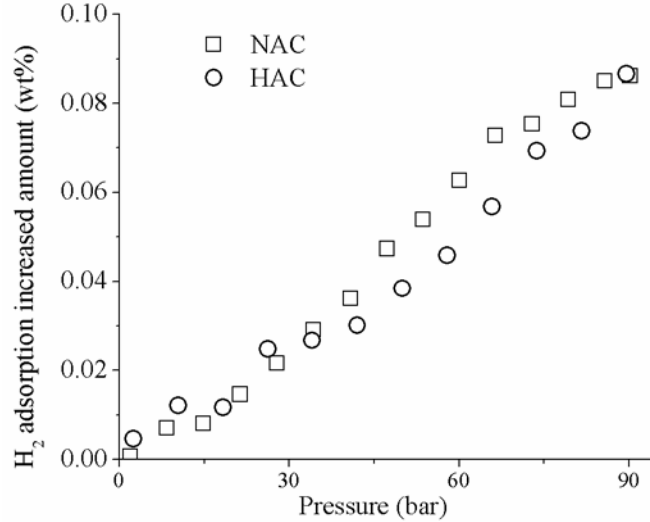


Figure 7.2. H₂ adsorption increased amount of NAC and HAC at 293K

Hydrogen adsorptions on NAC and HAC with PMN-PT at 77 K with pressure up to 60 bars were also investigated. Figure 7.3 shows the results. The error between three repeated measurements was less than 4% (see error bars in Figure 7.3). At 77K, the hydrogen adsorption of NAC is 3.25wt% at 60bar and the hydrogen adsorption of HAC is 4.37wt% at the same condition. With the addition of PMN-PT, NAC has the hydrogen adsorption capacity increased to 3.69wt% and HAC has the hydrogen adsorption capacity increased to 4.75wt% at 60bar and 77K. The hydrogen adsorption increased amount is proportional to the increase of hydrogen pressure, which is the same as at 293K. However, the amount of increase at 77K is much higher than that at 293K. At 77K and 60 bar, the hydrogen adsorption increased by about 0.44wt% and 0.38wt% for NAC and HAC, respectively. At 293K and 90 bar, the increase is only 0.08wt% for both samples.

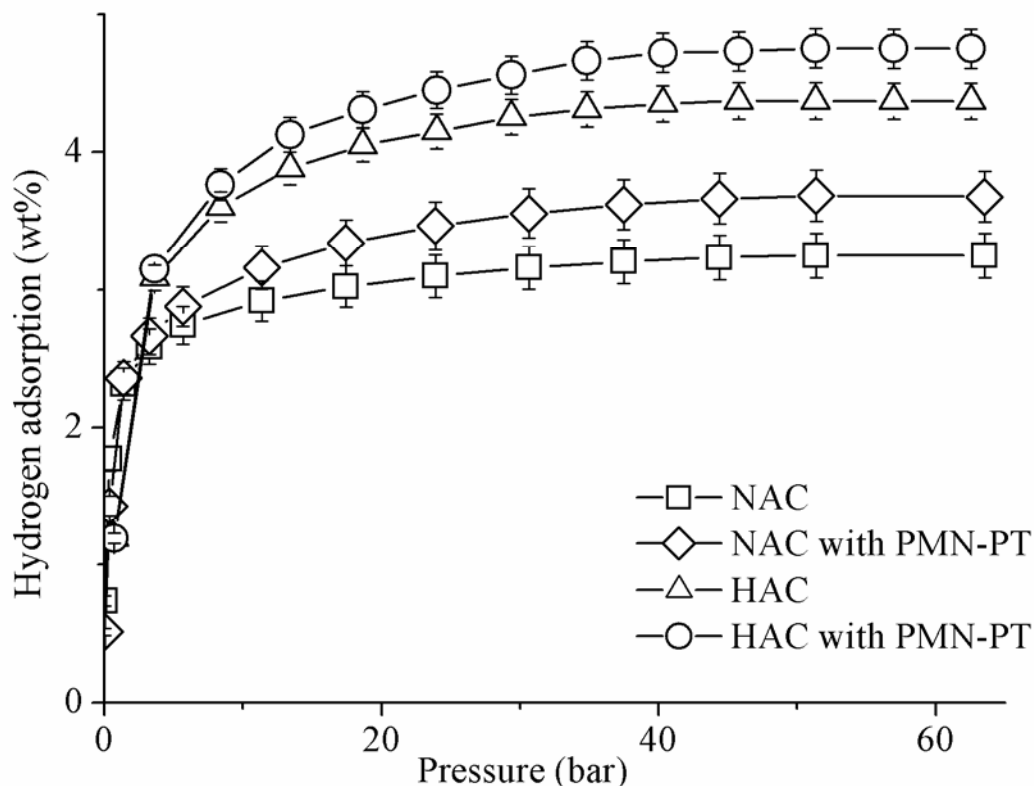


Figure 7.3. PMN-PT effect on H₂ adsorption of NAC and HAC at 77K

At 293K, hydrogen adsorption enhancement is observed at hydrogen pressure exceeds 15 bars. However, the enhancement can be observed at pressure of about 5 bars when the temperature is lowered to 77K. Hydrogen molecules have lower kinetic energy at 77K than at 298K. Consequently, the static bonding force exerted on H₂ molecules can easily be affected by charge from PMN-PT and becomes stronger.

Hydrogen adsorption capacities of the PMN-PT under the same experimental conditions have also been determined. The significantly hydrogen adsorption enhancement observed in this study was clearly the due to the charges generated from the pressurized PMN-PT.

7.3 Activated Carbon and Platinum Coated Activated Carbon under External Electric Potential

7.3.1 Background

Recent studies have shown that the hydrogen storage capacity of carbon materials could be significantly improved by hydrogen spillover using a carbon supported platinum catalyst [18-22]. The fundamental hydrogen spillover concepts were established in the late 1960s and 1970s and

refer to the migration of surface hydrogen species, produced by the dissociation of hydrogen molecules on metal sites, to a support that has no activity for dissociative hydrogen adsorption under the same conditions [20].

Our target in this work is studying the effect of electric potential for the adsorption of hydrogen on activated carbon and platinum coated activated carbon at room temperature.

7.3.2 Experimental

7.3.2.1 Materials

Two kinds of activated carbon were used in this study as adsorbents for hydrogen storage. One was Norit A supra activated carbon (NAC) from Norit Corporate with a BET surface area of $1836\text{m}^2/\text{g}$ (measured with a Micromeritics ASAP 2000 apparatus). The other was a mixture of the NAC and a platinum coated NAC (Pt-NAC). Pt-NAC was prepared by mixing NAC and platinum on activated carbon (contains 5wt% platinum, from Aldrich Chemistry) at a ratio of 4 to 1. The mixed sample is designated as Pt/NAC and its BET surface area is measured at $1352\text{m}^2/\text{g}$.

7.3.2.2 Hydrogen adsorption

Hydrogen storage adsorption experiments were carried out with a Hy-Energy's PCT Pro 2000 sorption instrument. This fully automated Sievert's-type instrument can run at a maximum pressure of 170 bars. The sample holder of the equipment was modified, as shown in Figure 7.4, to provide the capability for introducing electric potential to the testing material. The electrode in the center of the cylindrical sample holder was connected to a high voltage power supply (RLPS100-100P, from Del Electronics Corporation). The wall of the sample holder is electrically grounded. A dielectric layer with thickness of 0.2 mm coated the inner wall for charge holding. Around 1.5 gram activated carbon in the sample holder covered the electrode and contacted with dielectric layer, in such arrangement the electric potential could be preserved inside the carbon samples. The filter was used for preventing carbon particles entering the PCT Pro 2000 instrument. The thermocouple was used for measuring the temperature. Adsorption experiments were conducted at room temperature.

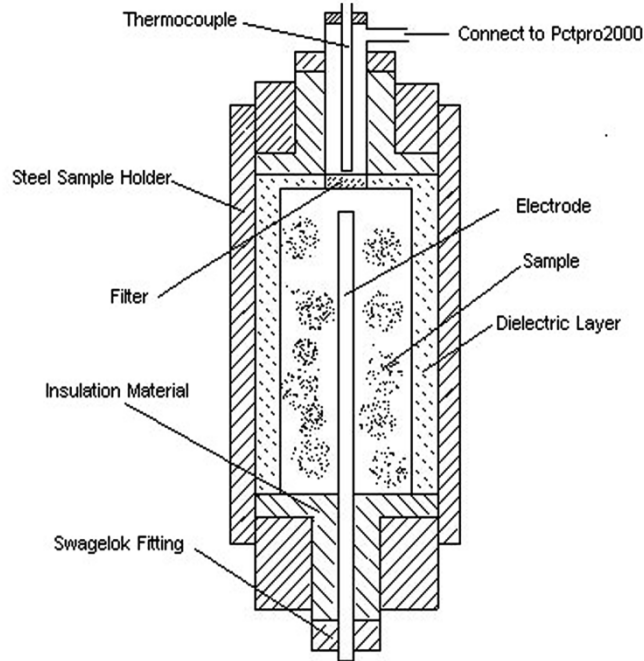


Figure 7.4. Cross-section of Sample Holder

7.3.3 Results and discussion

7.3.3.1 Hydrogen adsorption on Activated Carbon with applied electric potential

Hydrogen adsorption isotherms on NAC at different applied electric potentials are shown in Figure 7.5. The applied electric potential ranged from 0 to 3000 Volts. The pressure for each test ranged from 0 to 83 bars. The error for the measurements was between 2% and 6% (see error bars in Figure 7.5) based on three repeated experiments. The error at high pressure (6%) is higher than that at low pressure (2%). The error is also higher at high electric potential (6%) than that at zero electric potential (3%).

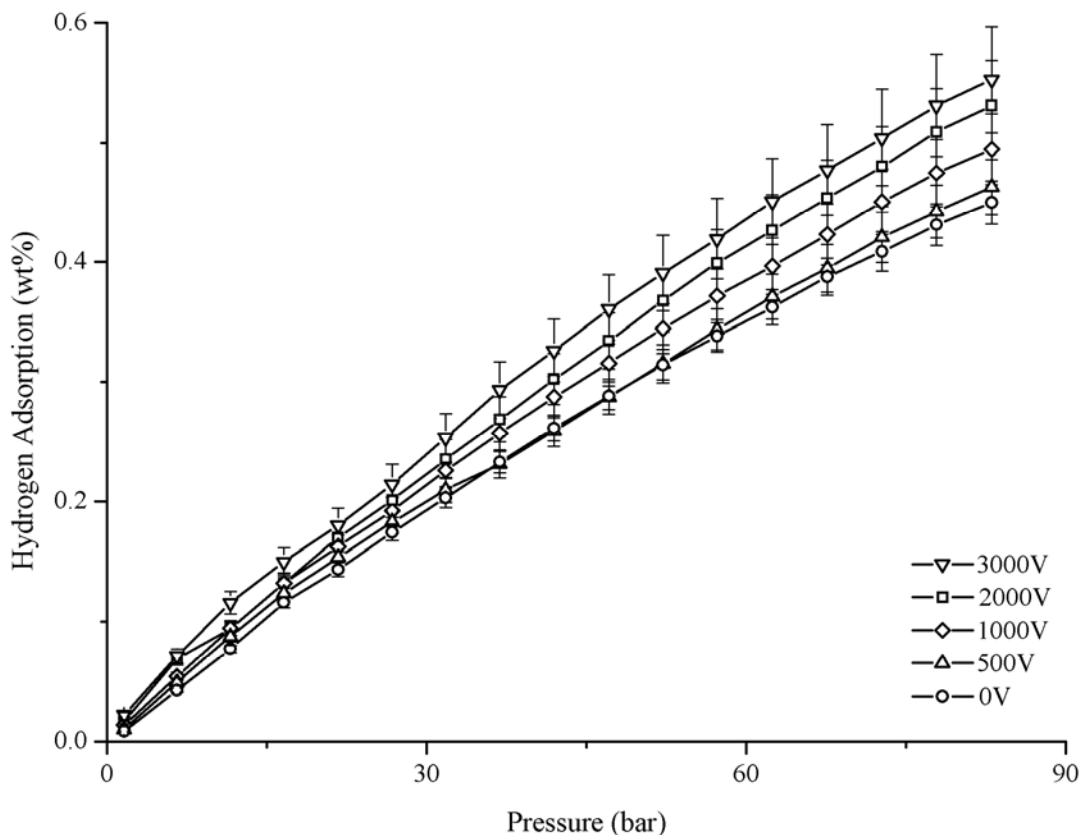


Figure 7.5. Hydrogen adsorption on activated carbon under various pressures and voltages.

Without electric potential, the hydrogen adsorption capacity is 0.008 wt% at 1.6 bars for the activated carbon sample. At 500, 1000, 2000, and 3000 volts, this adsorption capacity increases to 0.010, 0.014, 0.017 and 0.021 wt%, respectively. At 83 bars, the adsorption capacity increases from 0.45 wt% at 0 volts to 0.46, 0.49, 0.53 and 0.55 wt% at 500, 1000, 2000, and 3000 volts, respectively.

Within the range of our experiments with voltage from 0 to 3000 Volts, it is obvious that the higher the voltage of the applied electrical potential, the higher the amount of hydrogen adsorption. To better understand the effects, an adsorption enhancement index was introduced for comparison. The adsorption enhancement index was calculated based on:

$$\text{Ads. Enhancement(\%)} = \frac{\text{Ads. with E-potential} - \text{ads. w/o E-potential}}{\text{ads. w/o E-potential}} \times 100\%$$

Figure 7.6 shows the results of adsorption enhancement under various voltages. At 500 volts, the enhancement ranges from 25% at low pressure to negligible at high pressures. At 1000 volts, the

enhancement ranges from 75% at low pressure to 9% at high pressures. At 2000 volts, the range is 113% to 18% and at 3000 volts, the range is 163% to 22%.

There are several phenomena observed from the results. First, the enhancement is improved at higher voltages. The enhancement is limited at 500 volts, but it is more significant at 2000 and 3000 volts. Second, the enhancement is much more significant at low pressure than at high pressure. At 3000 volts, the adsorption enhancement can reach 163% at 1.6 bars of hydrogen pressure but it falls quickly to 20 to 30% at pressures above 20 bars.

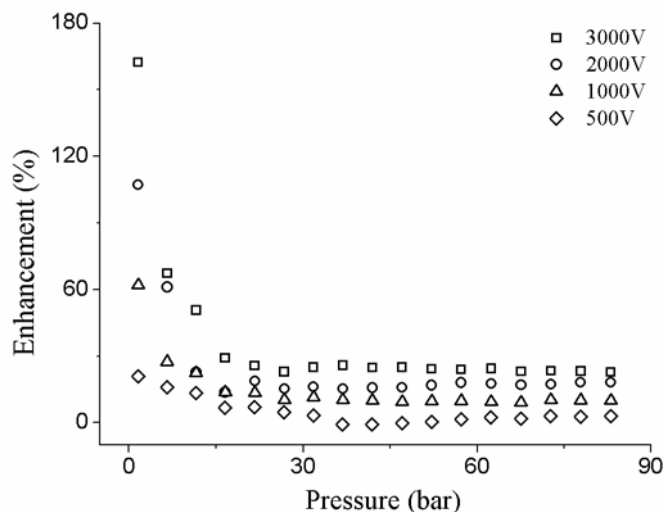


Figure 7.6. Adsorption enhancement on activated carbon at various voltages

When hydrogen molecules are adsorbed on adsorbent through physisorption, the bond length H-H of hydrogen molecule will be increased [24]. The stronger bond between hydrogen and adsorbent generate longer H-H bond length of hydrogen molecule. The longer H-H bond length indicates lower dissociation energies of hydrogen molecules. Activated carbon is a conductive material. Under an electric potential, the charge will accumulate at the surface of activated carbon. This may make the polarization of nearby hydrogen molecules or even the dissociation of hydrogen molecules easier when the applied voltage is sufficiently high. At low hydrogen pressure, the ratio of H₂ molecules that become polarized or dissociated by the charge is higher than the ratio at high hydrogen pressures. The better enhancement at low pressures can probably be explained by this.

7.3.3.2 Hydrogen adsorption on Pt Coated AC with applied electric potential

It has been demonstrated recently that platinum coated activated carbon has the capability to catalytically split hydrogen molecules, which enhances the adsorption of hydrogen through the spillover mechanism [19, 25]. Experiments have also been conducted to determine the effects of an electric potential on the mixture of the platinum coated carbon and activated carbon (Pt/NAC).

Figure 7.7 shows the adsorption capacity of hydrogen on Pt/NAC at various voltages. The error for the measurements is between 1% and 4%, much lower than that for the NAC experiments. The results have the same trends of adsorption enhancement for the voltage and pressure parameters. The higher the voltage and pressure, the higher the amount hydrogen adsorbed. Measured hydrogen adsorption capacities are 0.008, 0.01, 0.02, 0.03, 0.05, and 0.06 (0.058) wt% for 0, 500, 1000, 1500, 2000, and 2500 volts of applied electric potential at 1.6 bars of hydrogen pressure, respectively. At 83 bars, the hydrogen adsorption capacities are 0.43, 0.45, 0.46, 0.49, 0.52, and 0.56 wt% for 0, 500, 1000, 1500, 2000, and 2500 volts of applied electric potential, respectively.

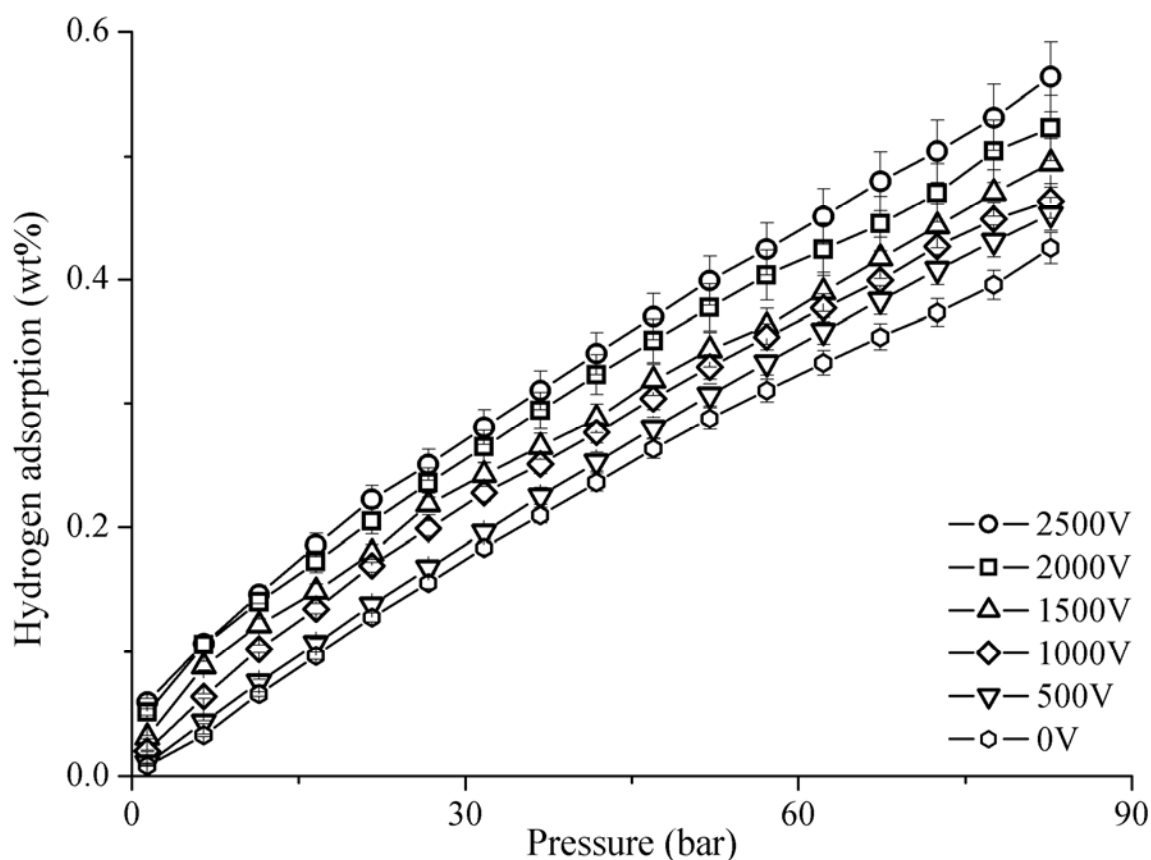


Figure 7.7. H adsorption on Pt/NAC under various pressures and voltages

The adsorption enhancement index for the Pt/NAC tests has also been calculated and the results are shown in Figure 7.8. At 1.6 bars, 625% adsorption enhancement can be obtained at 2500 volts; while the enhancement is 525% at 2000 volts, 275% at 1500 volts, 150% at 1000 volts and 25% at 500V volts. The hydrogen adsorption improvement is much higher than non-Pt containing samples. At 83 bars pressure, adsorption enhancement is 3% at 500 volts, and can reach about 30% at 2500 volts.

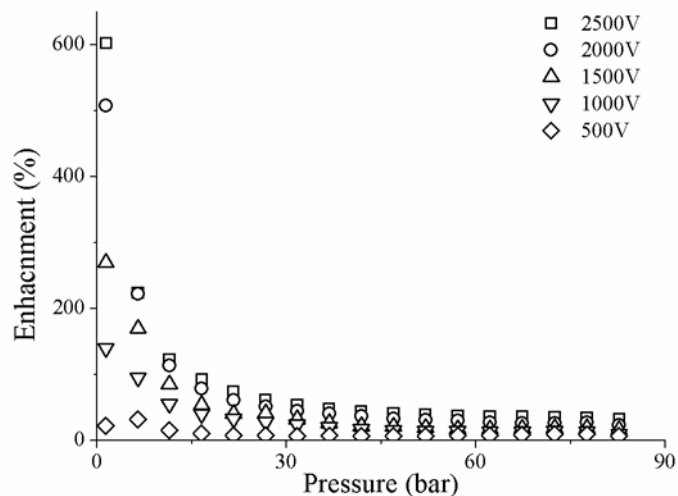


Figure 7.8. Adsorption enhancement of Pt/NAC at various voltages

The hydrogen adsorption capacity without applied electric potential is about 0.43 wt% for Pt/NAC at 293k and 83 bars and 0.45 wt% for NAC under the same conditions. The hydrogen adsorption capacity for these two materials is similar. However, the surface area of NAC is 1836m²/g, which is much larger than the 1352 m²/g surface area of Pt/NAC. It is remarkable that, normalized by BET surface area [26], Pt/NAC had higher hydrogen adsorption than NAC as shown in Figure 7.9. The Pt/NAC had hydrogen storage capacity of 0.31wt%/1000m²/g at 298 K and 83 bar, while the NAC had hydrogen storage capacity of 0.24wt%/1000m²/g under the same conditions. This is consistent with the conventional spillover theory. Pt acts as a catalyst for the dissociation of hydrogen molecules to promote the hydrogen adsorption by the following mechanisms: (1) H₂ molecules undergo dissociative chemisorption on Pt particles located on the activated carbon surface; (2) H atoms migrate onto the surface and into the bulk of activated carbon via chemisorption or physisorption; (3) H atoms diffuse from the adsorption sites at the vicinity of the Pt to sites far from the Pt [22, 25].

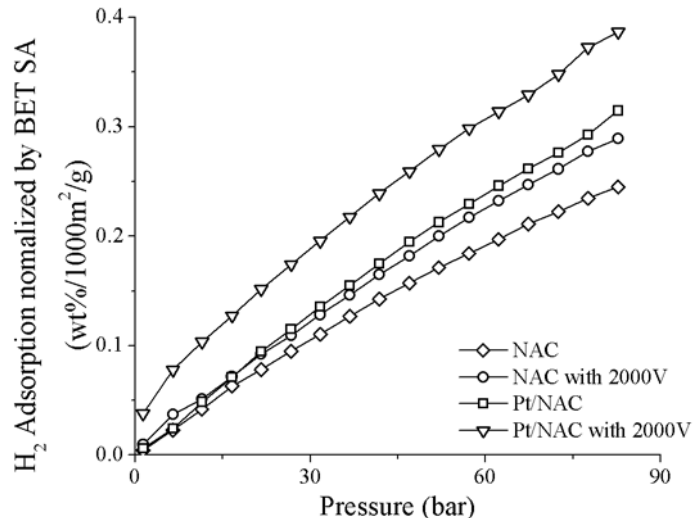


Figure 7.9. Hydrogen adsorption normalized by BET surface area

When an electric potential is applied, the adsorption enhancement of Pt/NAC is much higher than that of NAC. This may be explained by the following reasons. First, in the hydrogen dissociation process, the charge may facilitate the dissociation of hydrogen molecules on Pt particles, and H₂ molecules may also be directly dissociated by the charge. The dissociation of H₂ molecules directly by the charge would be the same for both the Pt/NAC and NAC. But the additional charge promoted H₂ molecules dissociation on platinum would enhance the adsorption. Second, the charge may accelerate the diffusion of H atoms into the bulk material.

7.4 Hydrogen Desorption

Hydrogen desorption experiments were carried out on Pt/NAC by releasing the pressure at room temperature under various voltages. The results are shown in Figure 7.10. Hydrogen adsorption capacity on Pt/NAC decreases with the release of pressure under the applied voltage. This suggests that physisorption is the adsorption type. The hydrogen adsorption on activated carbon under electric potential is reversible.

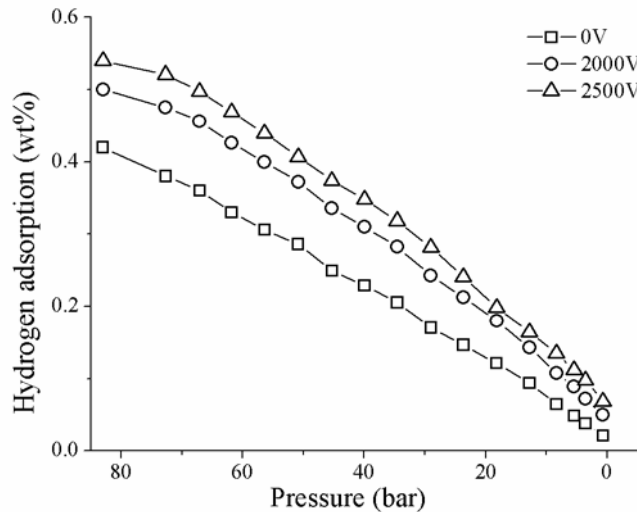


Figure 7.10. Hydrogen desorption of Pt/NAC under various pressures and voltages

7.5 Conclusions

The adsorption of hydrogen on activated carbon under the electric field generated from a piezoelectric material has been quantitatively studied at 293K and 77K. The results show that significant enhancement on hydrogen adsorption can be obtained. The amount enhancement is proportional to the amount of charges generated by the piezoelectric material. High pressure creates more charges and hence the higher amount of hydrogen adsorption. Low temperature also favors the adsorption enhancement. Electric field may affect the bonding of hydrogen molecules at larger extent when the molecules have lower kinetic energy at lower temperatures.

The hydrogen adsorption behavior of activated carbon (NAC) and its mixture with platinum coated activated carbon (Pt/NAC) under electric potential at room temperature was studied. The increase in voltage caused an increase in hydrogen adsorption. The hydrogen adsorption capacity increases from 0.008 wt% at 1.6 bars for the activated carbon sample without electric potential to 0.021 wt% at 3000 volts, which is a 163% increase. At 83 bars, the adsorption capacity increases from 0.45 wt% without electric potential to 0.55 wt% at 3000 volts, which is a 22% increase. The enhancement phenomenon is more obvious at low pressures. This is probably due to the ratio of H₂ molecules that become polarized or dissociated by the charge at low hydrogen pressure is higher than the ratio at high hydrogen pressures.

The mixture of activated carbon and platinum coated carbon has higher hydrogen adsorption capacity than the activated carbon sorbent alone. Without electric potential, the hydrogen adsorption capacity is 0.008 wt% at 1.6 bars for the mixture sample. At 2500 volts, this adsorption capacity increases to 0.058 wt%, which is a 625% increase. At 83 bars, the adsorption capacity increases from 0.43 wt% at 0 volt to 0.56 wt% at 2500 volts, which is a 30% increase.

The electric potential may have raised the catalytic activity of platinum for the dissociation of hydrogen molecules and assisted the diffusion of the dissociated species into the bulk material. Hydrogen desorption experiments reveal that physisorption is the adsorption mechanism and the adsorption is reversible.

7.6 Section 7 References

- [1] S.Z. Shi, J.Y. Hwang, Research frontier on new materials and concepts for hydrogen storage, *Int J Hydrogen Energ.* 32 (2007) 224 – 228
- [2] B. Bogdanovic, M. Felderhoff, S. Kaskel, A. Pommerin, K. Schlichte, F. Schuth, Improved hydrogen storage properties of Ti-doped sodium alanate using titanium nanoparticles doping agents, *Adv Mater.* 15 (2003) 1012–10125.
- [3] N.L. Rosi, J. Eckert, M. Eddaoudi, D.T. Vodak DT, J. Kim, M. O’Keeffe, O.M. Yaghi, Hydrogen storage in microporous metal-organic frameworks, *Science.* 300 (2003) 1127–1129.
- [4] R.Z. Ma, Y. Bando, H.W. Zhu, T. Sato, C.L. Xu, D.H. Wu, Hydrogen uptake in boron nitride nanotubes at room temperature, *J Am Chem Soc.* 124 (2002) 7672–7273.
- [5] P. Chen, Z.T. Xiong, J.Z Luo, J.Y. Lin, K.L. Tan, Interaction of hydrogen with metal nitrides and imides, *Nature.* 420 (2002) 302–304.
- [6] H.Y. Shao, H.R. Xu, Y.W. Wang, X.G. Li, Preparation and hydrogen storage properties of Mg₂Ni intermetallic nanoparticles, *Nanotechnology.* 15 (2004) 269–274.
- [7] D. Cao, P. Feng, J. Wu, Molecular simulation of novel carbonaceous materials for hydrogen storage, *Nano Lett.* 4 (2004) 1489–1492.
- [8] D.J. Browning, M.L. Gerrard, J.B. Lakeman, I.M. Mellor, R.J. Mortimer, M.C Turpin, Studies into the storage of hydrogen in carbon nanofibers: proposal of a possible reaction mechanism, *Nano Lett.* 2 (2002) 201–205.
- [9] N. Texier-Mandoki, J. Dentzer, T. Piquero, S. Saadallah, P. David, C. Vix-Guterl, Hydrogen storage in activated carbon materials: role of the nanoporous texture, *Carbon.* 42 (2004) 2744–2747.
- [10] R.H. Bauhman, A.A. Zakhidov, W.A. de Heer, Carbon nanotubes—the route toward applications, *Science.* 297 (2002) 787–792.
- [11] K. M. Thomas, Hydrogen adsorption and storage on porous materials, *Catal Today.* 120 (2007) 389–398.
- [12] X. B. Zhao, B. Xiao, A. J. Fletcher, and K. M. Thomas, Hydrogen Adsorption on Functionalized Nanoporous Activated Carbons, *J. Phys. Chem. B.* 109 (2005) 8880–8888
- [13] M. Rzepka, P. Lamp, M. A. de la Casa-Lillo, Physisorption of Hydrogen on Microporous Carbon and Carbon Nanotubes. *J. Phys. Chem. B.* 102 (1998) 10894–10898
- [14] Z.W. Yin, H.S. Luo, P.C. Wang, G.S. Xu, Growth, characterization and properties of relaxor ferroelectric PMN-PT single crystals, *Ferroelectrics.* 229 (1999) 207–216.

- [15] Z.R. Li, Z.Z. Xi, Z. Xu, X. Yao, Dielectric/ferroelectric response and phase transition of PMN0.32PT single crystal, *J. Mater. Sci. Lett.* 21 (2002) 1325–1327.
- [16] S.Z. Shi, J.Y. Hwang, X. Li, X. Sun, Enhanced hydrogen sorption on carbon and NiO in the presence of a piezoelectric element, *Energy & Fuels*. (2009) in press.
- [17] <http://www.morganelectroceramics.com/piezomaterials/singlecrystal>
- [18] Chen HL, Yang H, Briker Y, Fairbridge C, Omotoso O, Dinga LH, et al. Effect of hydrogen spillover on the hydrogenation of 1-hexene over diluted carbon molecular sieve supported Pt catalyst. *Catal Today*. 2007; 125(3-4):256-62.
- [19] Chen HL, Yang H, Omotoso O, Ding LH, Briker Y, Zheng Y, et al. Contribution of hydrogen spillover to the hydrogenation of naphthalene over diluted Pt/RHO catalysts. *Appl Catal a-Gen*. 2009; 358(2):103-9.
- [20] Chen L, Cooper AC, Pez GP, Cheng H. Mechanistic study on hydrogen spillover onto graphitic carbon materials. *J Phys Chem C*. 2007; 111(51):18995-9000.
- [21] Lueking AD, Yang RT. Hydrogen spillover to enhance hydrogen storage - study of the effect of carbon physicochemical properties. *Appl Catal a-Gen*. 2004; 265(2):259-68.
- [22] Sha XW, Knippenberg MT, Cooper AC, Pez GP, Cheng HS. Dynamics of Hydrogen Spillover on Carbon-Based Materials. *J Phys Chem C*. 2008;112(44):17465-70.
- [23] Hwang JY, Shi SZ, Li BW, Sun X. Storing Hydrogen with Perhydrides. *Adv Mater for Energ Conversion III*. 2006; 101-7
- [24] Park N, Hong S, Kim G, Jhi SH. Computational Study of Hydrogen Storage Characteristics of Covalent-Bonded Graphenes. *J. AM. CHEM. SOC*. 2007; 129: 8999-9003
- [25] Wang L, Yang RT. New sorbents for hydrogen storage by hydrogen spillover – a review. *Energy Environ. Sci*. 2008; 1:268-79
- [26] Wang L, Yang FH, Yang RT. Effect of Surface Oxygen Groups in Carbons on Hydrogen Storage by Spillover. *Ind. Eng. Chem. Res*. 2009; 48:2920-6

8. PERCOLATIVE MOF-CARBON COMPOSITES FOR HYDROGEN STORAGE

8.1 Introduction

The largest obstacle for utilizing hydrogen energy for transportation applications is the reversible storage of hydrogen gas in vehicles. With respect to the gas physisorption, various adsorbents such as activated carbon [1-6], carbon nanostructures [7-9], and zeolites [10,11] have been extensively researched in last decades. However, at ambient temperature, none of these adsorbents can be used for transportation applications. Recently, a new class of porous materials, named metal organic frameworks (MOFs) has been developed which have extremely large surface area and potential applications as adsorbents [12-19]. Although promising storage capacity has been achieved at 77K [20-22], the weak adsorption energy limits MOF's real hydrogen storage applications. Hydrogen spillover has remarkably increased the storage capacity of IRMOF-8 (isoreticular metal-organic frameworks) to 4 wt% at room temperature [23,24], however, the strong interaction energy results in problems such as slow adsorption/desorption kinetics, and questionable reversibility.

Our study has shown a novel way to increase hydrogen adsorption enthalpy in carbon [25, 26] and oxide materials [27] by using an external electric field. Promising enhancement has been achieved and our computational work [28] also supports these observations. Moreover, a recent publication [29] from another group also demonstrated the storage enhancement effect of an electric field in graphenes. To date, such approach has not been employed with MOF materials. Since most MOF materials are not electrically conductive, the charge built up on the surface cannot be distributed throughout every particle. Therefore, adding conductive agents into MOFs without significantly affecting the total porosity is critical to realize charge enhancement in MOF materials.

Percolation is a method of adding conductive materials (filler) into a non-conductive polymer or ceramics (matrix) to alter the dielectric properties [30,31] of the matrix. The percolative composites composed of carbon materials/PVDF [32], CNT/ ceramics [33,34], and CNT/BaTiO₃ [35] all showed promising improvement of their dielectric constant.

In this study, IRMOF-8 was directly deposited onto activated carbon to form a percolative MOF-activated carbon composite, following the theory of heterogeneous nucleation. The dielectric constant of the composites was evaluated and, as the carbon content increased, significant enhancement was observed. Moreover, the composites were tested for hydrogen storage with and without the presence of the charge generating material PMN-PT (single crystal lead magnesium niobate - lead titanate). Significant enhancement was achieved when the composite followed the insulator to conductor transition. Furthermore, DFT (density functional theory) computational work on the individual MOF and carbon cluster also demonstrated the considerable storage enhancement from the external electric field.

8.2 Experimental

8.2.1 Preparation of MOF-carbon composites

IRMOF-8 was synthesized on activated carbon by using the DMF approach [24, 36, 37]. $\text{Zn}(\text{NO}_3)_2 \cdot 6\text{H}_2\text{O}$ (1.19 g) was dissolved in 40 ml DMF (N,N'-dimethylformamide) with magnetic stirring. A desired amount of powdered Norit A Supra (Norit Corporation) activated carbon was added to the solution. 2,6-Naphthalene dicarboxylic acid (0.43 g) was then added and stirred until dissolved. Three drops of hydrogen peroxide (30 wt%) solution was added. Then Triethylamine (2.3 ml) was added dropwise and the solution was stirred for 1 hour. The IRMOF-8 product was recovered by repeated filtration and DMF washing for three times. It was then degassed at room temperature for 6 hours and heated to 180 °C at a heating rate of 1 °C/min, and kept overnight in a box vacuum furnace (Precision).

Depending on the amount of activated carbon used for synthesis, the samples were denoted as MOFAC1, MOFAC2, and MOFAC3.

8.2.2 Characterization

Thermogravimetric analysis (TGA) was performed under nitrogen flow at a heating rate of 10 °C/min from 25 °C to 600 °C by using a SDT Q600 V8.3 Build 101 (TA Instruments). X-ray diffraction (XRD) measurement was carried out with a Scintag XDS2000 Powder Diffractometer at a scan rate of 0.08°/s with Cu radiation at 45 kV, 35 mA. A Hitachi S-4700 field emission-scanning electron microscope (FE-SEM) was used to examine the microstructure of the samples. The surface area and pore size distribution were measured using a Micromeritics ASAP2000 instrument. The samples were evacuated by heating at 200°C under vacuum for 12 hours before testing.

The dielectric constant was measured with a HP 4192A LF impedance analyzer and a specially designed sample holder. As shown in Figure 8.1, the sample holder consists of two metal parts, each connected to the analyzer through electrical wires. The PVDF ring was placed into the bottom steel holder, leaving the center circle (one inch in diameter and 0.0625 inch in depth) open. The samples were loosely contained inside the PVDF ring and covered by the top steel holder for the measurement. This kind of arrangement is essential to have comparable analysis with the hydrogen storage measurement, where the sample powders were loosely placed inside the storage sample holder. The electrical resistivity was measured with a digital multimeter (Agilent 34405 A).

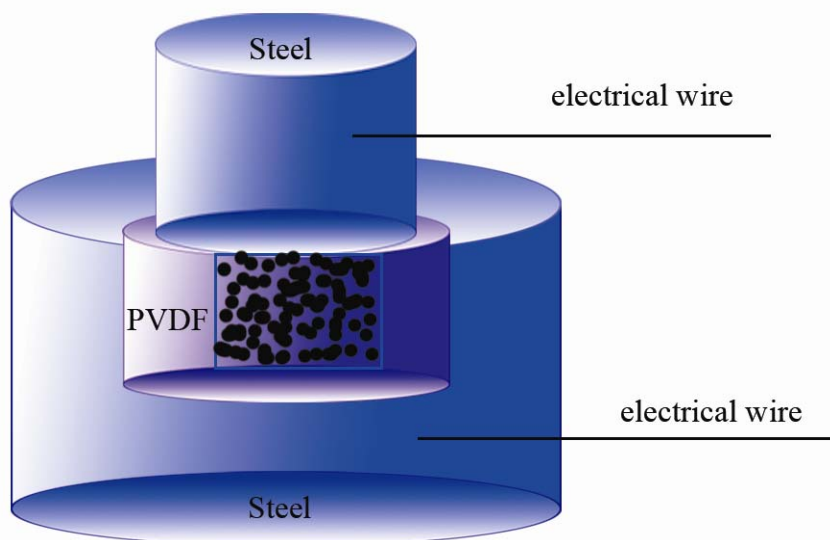


Figure 8.1. Schematic of the holder used for measurement of dielectric constant

8.2.3 Hydrogen storage measurement

Hydrogen adsorption at pressures between 0.1 bar and 140 bar was measured by using static volumetric techniques with an automatic Sieverts' apparatus (PCT-Pro 2000 from Hy-Energy LLC) at room temperature. Previous to the test, samples were degassed extensively at 200°C for 12 hours and then carefully moved into the sample holder and evacuated again at 100°C for 2 hours to ensure the removal of any contamination on the sample surface. Approximately 100-300 mg of the sample was used in each test, and ultra pure (99.999%) hydrogen and helium gases were used for all calibrations and measurements.

Single crystal PMN-PT disks were acquired from Morgan Electro Ceramics, 5 mm in length and width, and 1 mm in thickness. For the conductive samples, the positive side of the PMN-PT was covered by a non-conductive thin BaTiO₃ film made by BaTiO₃ powders and glue to prevent electron transfer from the negative side to the positive side. The coated PMN-PT was then immersed in the adsorbents for measurement. For the non-conductive samples, the plain PMN-PT was directly immersed in the samples. A glass container was used to ensure good electric insulation from the outside steel holder. In such an arrangement, the electrons from the PMN-PT were not able to transfer to the outside so that the electric field could be preserved inside the adsorbents.

8.2.4 Computational modeling

All the calculations were performed using the PBE/6-31G(d) [38,39] method in the GAUSSIAN 03 software program [40]. Our previous calculations [28] demonstrated the reliability of the basis set for this type of small cluster system. The IRMOF-8 and carbon building blocks were calculated separately under the external electric field. The field was applied along the vertical direction of the MOF building unit and perpendicularly to the carbon plane at field strengths of 0.01 and 0.015 au, as shown in Figure 8.2. The total hydrogen adsorption energy was determined by the difference between the total energy of the whole adsorption system and the total energy of the separate reactants before combination, as presented in following equation:

$$E_{ad} = E(\text{cluster} + H_2) - E(\text{cluster}) - E(H_2) \quad (1)$$

The obtained adsorption energy was further corrected by BSSE (Basis Set Superposition Error) using the full counterpoise method [41].

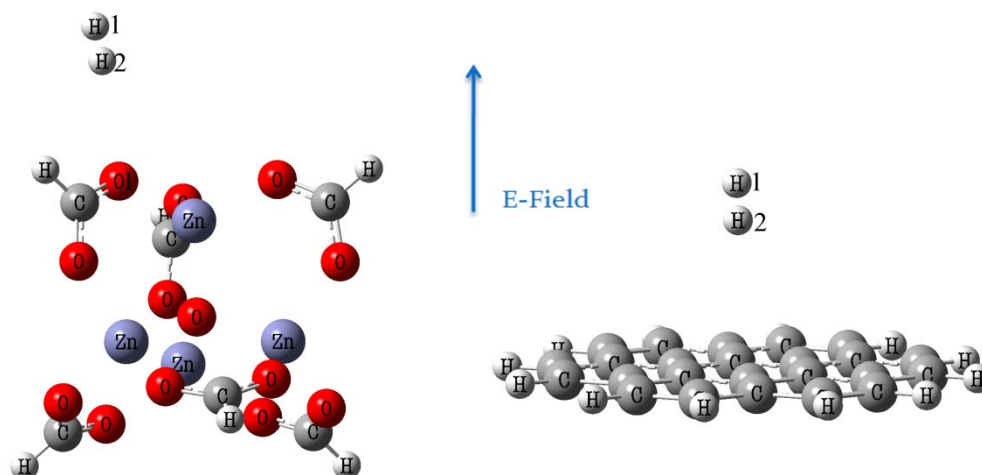


Figure 8.2. Computational modeling of hydrogen adsorption on $[Zn_4O]^{6+}$ cluster (left) and graphite surface (right)

8.3 Results and Discussion

8.3.1 Experimental results

Figure 8.3 shows the XRD spectra of as-synthesized IRMOF-8 and the activated carbon composites. The patterns for both pure IRMOF-8 and MOFAC match well with previous data on IRMOF-8 synthesized by the DMF approach²⁴, which proves that the deposition process did not alter the IRMOF-8 crystal structure. The TGA analysis (Figure 8.4) shows that pure IRMOF-8

and the MOFAC composites all exhibit similar weight loss curves upon heating. They started to lose weight due to the removal of moisture and solvent at temperatures above 100 °C. A major weight loss occurred at 400 °C, where thermal decomposition took place. Pure IRMOF-8 had a total weight loss of 52.83 wt% at 600 °C. Since activated carbon has nearly zero weight loss upon heating in nitrogen atmosphere, the weight loss of pure MOF was used to calculate the MOF content in the MOFAC composites. As shown in the embedded table in Figure 8.4, the MOF wt% in MOFAC1, MOFAC2, and MOFAC3 are 85.32%, 82.23%, and 77.80%, respectively.

Table 8.1 shows the conductivity and capacitance of the MOFAC composites. As the concentration of carbon increased, the capacitance increased. The insulator to conductor transition was observed at carbon weight fractions between 17.77 wt% to 22.2 wt%. The dielectric constant of the composites as a function of frequency and carbon content is shown in Figure 8.5. Virgin IRMOF-8 has a dielectric constant of 2. The dielectric constant of the composites rises with the increasing carbon fraction. The dielectric constants for both pure MOF and MOFAC are frequency independent at room temperature. The composites clearly show the tunable dielectric response from the addition of the activated carbon. The enhancement of the dielectric constant was attributed to the formation of minicapacitor networks [31, 35], where the carbon particles were covered by MOF materials forming localized capacitors. The frequency independent dielectric constant confirms the fact the minicapacitor is the only phenomenon [31] for these composites since the space charge polarization is frequency dependent [34]. However, in order to implant charge enhancement of hydrogen storage in MOF materials, a conductive network formed inside the composites is preferred, where space charge polarization [42] on the conductive path could effectively distribute the electrical charges. Therefore, the composites that have passed the insulator-conductor transition would be ideal for charge induced enhancement of hydrogen storage, which was verified from the storage analysis.

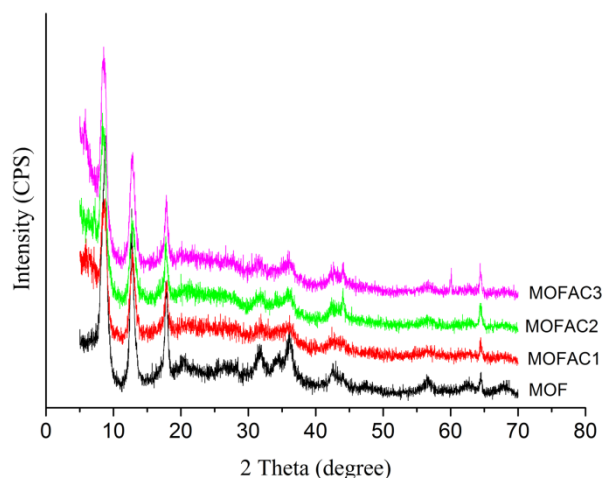


Figure 8.3. XRD of pure IRMOF-8 and carbon-IRMOF-8 composites

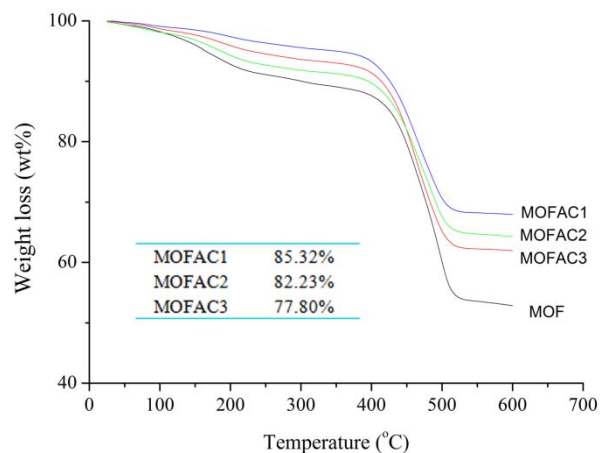


Figure 8.4. TGA curve of pure IRMOF-8 and carbon-IRMOF-8 composites

Table 8.1. DC conductivity and capacitance of IRMOF-8 and MOFAC composites

Sample	Conductivity	Capacitance
IRMOF-8	>100 M Ω	0.018 nF
MOFAC1	>100 M Ω	0.028 nF
MOFAC2	>100 M Ω	0.031 nF
MOFAC3	5.6 M Ω	—

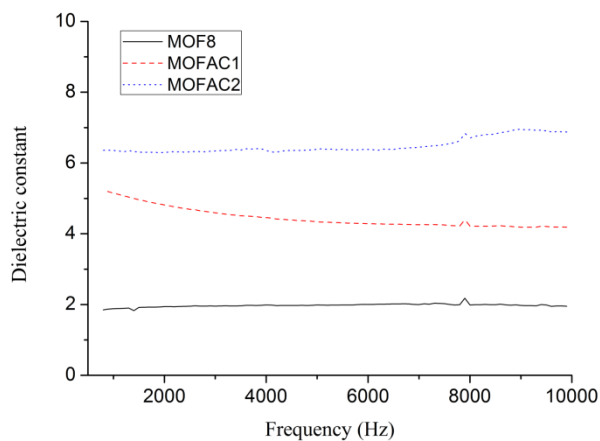


Figure 8.5. Dielectric constant of the MOFAC composites at room temperature as a function of frequency

Direct deposition of MOF materials onto carbon showed uniform distribution and good contact, as shown from the SEM analysis (Figure 8.6(a) and 6(b)). The carbon particles were covered by small spheroids of MOF, which heterogeneously nucleated on the carboxylate groups of the carbon surface, thus forming a strong inter-particle bond and good uniformity. Such deposition mechanism has also been employed in synthesis of MOF/CNT [43] and MOF thin films [44, 45]. Mechanically mixed MOF-carbon composites composed of the same weight ratio of MOFAC were also studied to compare the particle distributions. Clear particle separation was observed, where the MOF agglomerated together forming large chunks, as highlighted by the white circles in Figure 8.6 (c) and (d). The MOF particle distribution and MOF-carbon interconnection were poor. Therefore, the direct deposition method showed great advantages not only in the percolative effect, but also in the particle contacts and thus the charge distribution, where ideally every MOF particle could get charge from the nearby carbon particles.

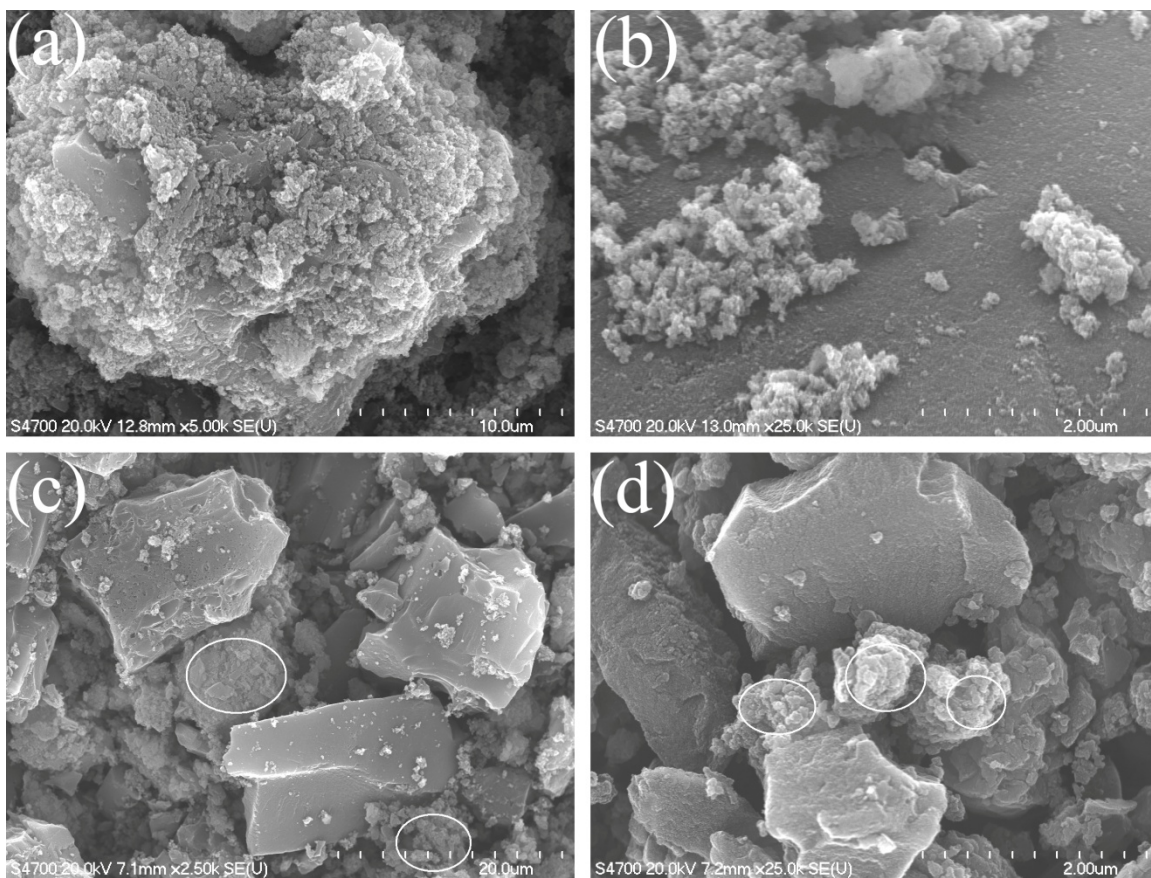


Figure 8.6. FE-SEM images of IRMOF-8 and activated carbon composites (a)(b) direct deposition, (c)(d) mechanical mixing

The important issue for synthesizing composites as adsorbents is that the total porosity should not be significantly affected. The total porosity of activated carbon, pure IRMOF-8, and MOFAC, measured by nitrogen adsorption is listed in Table 8.2. The large surface area discrepancy between IRMOF-8 and carbon ensures that the porosity of the composites increases

with increasing carbon content. The calculated BET surface area based on the weight percentage of each component in the composites is also presented in Table 8.2. For the MOFAC1 sample, there is a large difference between the measured and calculated surface area. This might be due to the over-deposited MOF, where the carbon surface was covered by multilayer MOFs and the pores were blocked to some extent. As the carbon content increases, e.g. MOFAC2 and MOFAC3, the calculated BET was in close range of the measured data. Therefore, for MOF content below 82.23 wt%, the activated carbon incorporation had negligible effects on the total porosity. The uniform deposition ensured the pores to be unblocked and open for gas adsorption.

Table 8.2. BET surface area of IRMOF-8, carbon, and MOFAC

Sample	BET Surface Area(sq m/g)	Micropore Area(sq m/g)	Calculated composite BET surface area(sq m/g)
Pure IRMOF-8	536.13	361.88	
carbon	1791.06	554.49	
MOFAC1	548.77	214.49	720.23
MOFAC2	724.46	262.91	759.01
MOFAC3	830.67	325.61	814.61

The hydrogen adsorption isotherm at 298 K is shown in Figure 8.7. Pure IRMOF-8 and MOFAC1 both have similar adsorption features and reach 0.1 wt% at 100 bar. With the presence of the charge generator PMN-PT, the enhancement of adsorption was nearly negligible. When the carbon content increased, as in MOFAC3, the storage increased to 0.197 wt% (80 bar), which was due to the contribution from the extra activated carbon. With help from the PMN-PT, the hydrogen uptake was further increased to 0.259 wt% (80 bar), which is about 31.5% enhancement over the MOFAC3. Our previous results²⁷ presented that the same activated carbon had 30% enhancement of hydrogen storage with the presence of PMN-PT at 80 bar. Based on the weight content of carbon in MOFAC3, the other significant amount of increase was due to the charged MOF materials, which accounted for 31.9 % enhancement for MOF. Moreover, the electric field enhancement was fully reversible, as indicated from the second adsorption isotherm of the MOFAC3 sample.

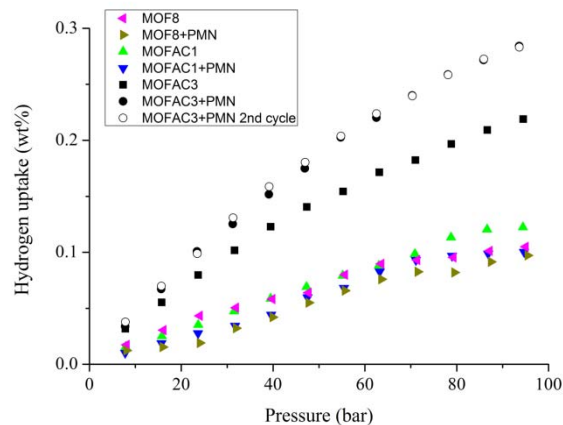


Figure 8.7. Hydrogen storage analysis of IRMOF-8 and MOFAC at 298K with and without the PMN-PT

The detailed mechanism is elucidated in Figure 8.8. When the PMN-PT was surrounded by IRMOF-8, the charges generated from the PMN-PT could not be distributed throughout the whole sample, but only concentrated on the surface. Therefore, the charge induced enhancement of hydrogen adsorption for pure IRMOF-8 was negligible. When carbon was induced and worked as a charge distributor, the electrical charges could be passed along by the contacted activated carbon particles. The IRMOF-8 particles could also receive the charges from the nearby carbon particles. The charge induced electric field implanted on both carbon and IRMOF-8 particles, thus forming a localized charge polarization. The induced strong electrostatic force could in turn polarize the incoming hydrogen molecules to form a strong bonding with the hydrogen and enhance the storage uptake. When the composite was not conductive, the charges were not distributed through the entire sample. Hence, only the conductive composite-MOFAC3 possessed significant charge induced enhancement of hydrogen storage. The optimum condition was not found in this study and future investigations are needed regarding increasing the carbon content further to study the charge effects.

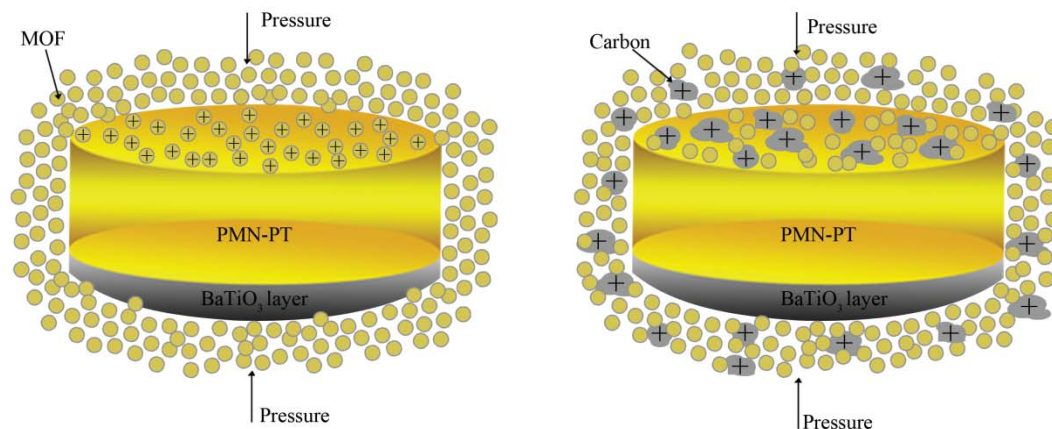


Figure 8.8. Schematic of charge distribution in pure IRMOF-8 (left) and MOFAC (right)

8.3.2 Computational results

Our calculations were focused on the hydrogen molecules adsorption on both IRMOF-8 building units and activated carbon. The optimized geometry configurations and the binding energies of the adsorption system are shown in Figure 8.2 and Table 8.3, respectively. Hydrogen could be adsorbed on the oxygen atom of the octahedral Zn_4O units following end on adsorption. With the addition of the external electric field at the strength of 0.01 a.u., the hydrogen adsorption energy increased from 2 kJ/mole to 4.92 kJ/mole. With further increased field strength to 0.015 a.u., the binding energy reached 9.09 kJ/mole, which is 4.5 times enhancement. The hydrogen molecules were more elongated at the stronger electric field, as indicated from the larger H-H bond length. Also the electrical field forced the hydrogen molecules to be attracted closer to the oxygen atom, indicating a stronger interaction. All these optimized parameters matched well with the binding energy observations. We also performed calculations of hydrogen adsorption on the NDC (2,6-naphthalene-dicarboxylate) linker in IRMOF-8. The calculation predicted that hydrogen cannot be stably adsorbed. Therefore, the primary adsorption site on IRMOF-8 would only be the oxygen atom of the Zn_4O unit. Similar calculations were carried out on $C_{24}H_{12}$ to model the carbon surface. Hydrogen is adsorbed and aligned vertically toward the center of the benzene ring. The same trend is observed, where hydrogen molecules become more perturbed with the increase of the electric field strength. The H-H bond length, H-benzene distance, and binding energies all support these observations.

The modeling results are in good agreement with the experimental observations. Under an electric field, both IRMOF-8 and carbon exhibit stronger affinity with hydrogen molecules. The overall storage capacity could be remarkably enhanced based on electric field strengthened interaction. The interaction energies from the computational results were on the order of 0.22 to 9.09 kJ/mole, which was below the required room temperature reversible adsorption enthalpy 15

kJ/mole [46], indicating that the adsorbed hydrogen could be totally released at 298 K. This again reflects the consistency with the experimental observations.

Table 8.3. Optimized geometry and binding energy of hydrogen adsorption on MOF Zn₄O unit and carbon under the external electric field

Field (a.u.)	H ₂ on Zn ₄ O unit			H ₂ on carbon		
	Binding energy (kJ/mole)	Hydrogen bond length (Å)	H ₂ -O1 distance (Å)	Binding energy (kJ/mole)	Hydrogen bond length (Å)	Distance between H ₂ and horizontal plane (Å)
0	-2	0.752	2.586	-0.22	0.751	3.117
0.01	-4.92	0.757	2.375	-2.23	0.752	3.011
0.015	-9.09	0.761	2.266	-3.94	0.753	2.951

8.4 Conclusion

IRMOF-8 has been successfully deposited on activated carbon through heterogeneous nucleation. The dielectric constant of the composites increased with increased carbon content. The charges generated by the PMN-PT were distributed through the composites and the hydrogen storage capacity was enhanced 31.5%. The computational modeling indicated that the hydrogen adsorption energies on both IRMOF and carbon could be enhanced by the external electric field.

8.5 Section 8 References

- [1] Jin, H., Lee, Y. S. and Hong, I. *Catalysis Today* **2007**, 120, 399.
- [2] Salvador-Palacios, F., Sanchez-Montero, M. J., Sanguesa-Dominguez, I. and Izquierdo-Misiego, C. *Advanced Materials Forum Iii, Pts 1 and 2* **2006**, 514-516, 427.
- [3] Nijkamp, M. G., Raaymakers, J. E. M. J., van Dillen, A. J. and de Jong, K. P. *Applied Physics a-Materials Science & Processing* **2001**, 72, 619.
- [4] Wang, H. L., Gao, Q. M. and Hu, J. *J Am Chem Soc* **2009**, 131, 7016.
- [5] Vasiliev, L. L., Kanonchik, L. E., Kulakov, A. G. and Mishkinis, D. A. *Hydrogen Materials Science and Chemistry of Carbon Nanomaterials* **2007**, 633.
- [6] Hermosilla-Lara, G., Momen, G., Marty, P. H., Le Neindre, B. and Hassouni, K. *International Journal of Hydrogen Energy* **2007**, 32, 1542.
- [7] Tibbetts, G. G., Meisner, G. P. and Olk, C. H. *Carbon* **2001**, 39, 2291.
- [8] Takagi, H., Hatori, H., Soneda, Y., Yoshizawa, N. and Yamada, Y. *Materials Science and Engineering B-Solid State Materials for Advanced Technology* **2004**, 108, 143.
- [9] Panella, B., Hirscher, M. and Roth, S. *Carbon* **2005**, 43, 2209.

- [10] Regli, L., Zecchina, A., Vitillo, J. G., Cocina, D., Spoto, G., Lamberti, C., Lillerud, K. P., Olsbye, U. and Bordiga, S. *Physical Chemistry Chemical Physics* **2005**, 7, 3197.
- [11] Griesinger, A., Spindler, K. and Hahne, E. *Hydrogen Energy Progress Xi, Vols 1-3* **1996**, 2513.
- [12] Cavenati, S., Grande, C. A. and Rodrigues, A. E. *Industrial & Engineering Chemistry Research* **2008**, 47, 6333.
- [13] Li, Q. W., Zhang, W. Y., Miljanic, O. S., Sue, C. H., Zhao, Y. L., Liu, L. H., Knobler, C. B., Stoddart, J. F. and Yaghi, O. M. *Science* **2009**, 325, 855.
- [14] Banerjee, R., Phan, A., Wang, B., Knobler, C., Furukawa, H., O'Keeffe, M. and Yaghi, O. M. *Science* **2008**, 319, 939.
- [15] Rosi, N. L., Eckert, J., Eddaoudi, M., Vodak, D. T., Kim, J., O'Keeffe, M. and Yaghi, O. M. *Science* **2003**, 300, 1127.
- [16] Long, J. R. and Yaghi, O. M. *Chemical Society Reviews* **2009**, 38, 1213.
- [17] Murray, L. J., Dinca, M. and Long, J. R. *Chemical Society Reviews* **2009**, 38, 1294.
- [18] Perry, J. J., Perman, J. A. and Zaworotko, M. J. *Chemical Society Reviews* **2009**, 38, 1400.
- [19] Li, J. R., Kuppler, R. J. and Zhou, H. C. *Chemical Society Reviews* **2009**, 38, 1477.
- [20] Furukawa, H., Miller, M. A. and Yaghi, O. M. *Journal of Materials Chemistry* **2007**, 17, 3197.
- [21] Ferey, G., Mellot-Draznieks, C., Serre, C., Millange, F., Dutour, J., Surble, S. and Margiolaki, I. *Science* **2005**, 309, 2040.
- [22] Dinca, M. and Long, J. R. *Angewandte Chemie-International Edition* **2008**, 47, 6766.
- [23] Li, Y. W. and Yang, R. T. *J Am Chem Soc* **2006**, 128, 8136.
- [24] Li, Y. W. and Yang, R. T. *J Am Chem Soc* **2006**, 128, 726.
- [25] Shi, S., Hwang, J.-Y., Li, X., Sun, X. and Lee, B. I. *International Journal of Hydrogen Energy* **2010**, 35, 629.
- [26] Li, X., Hwang, J.-Y., Shi, S., Sun, X. and Zhang, Z. *Carbon* **2010**, 48, 876.
- [27] Shi, S., Hwang, J.-Y., Li, X. and Sun, X. *Energy & Fuels* **2009**, 23, 6085.
- [28] Sun, X., in *Department of Materials Science and Engineering*, Michigan Technological University, Houghton, 2009, p. 196.
- [29] Liu, W., Zhao, Y. H., Nguyen, J., Li, Y., Jiang, Q. and Lavernia, E. J. *Carbon* **2009**, 47, 3452.
- [30] Wang, L. and Dang, Z. M. *Applied Physics Letters* **2005**, 87.
- [31] Chen, Q., Du, P. Y., Jin, L., Weng, W. J. and Han, G. R. *Applied Physics Letters* **2007**, 91.
- [32] Dang, Z. M., Wu, J. P., Xu, H. P., Yao, S. H., Jiang, M. J. and Bai, J. *Applied Physics Letters* **2007**, 91.
- [33] Ahmad, K., Pan, W. and Shi, S. L. *Applied Physics Letters* **2006**, 89.
- [34] Shi, S. L. and Liang, J. *Journal of the American Ceramic Society* **2006**, 89, 3533.
- [35] Yao, S. H., Dang, Z. M., Jiang, M. J. and Bai, J. B. *Applied Physics Letters* **2008**, 93.

- [36] Huang, L. M., Wang, H. T., Chen, J. X., Wang, Z. B., Sun, J. Y., Zhao, D. Y. and Yan, Y. *S. Micropor Mesopor Mat* **2003**, 58, 105.
- [37] Panella, B. and Hirscher, M. *Adv Mater* **2005**, 17, 538.
- [38] Becke, A. D. *J Chem Phys* **1993**, 98, 5648.
- [39] Lee, C. T., Yang, W. T. and Parr, R. G. *Phys Rev B* **1988**, 37, 785.
- [40] Frisch, M. J., et al. , Gaussian Inc. , Wallingford, CT 2004
- [41] Boys, S. F. and Bernardi, F. *Molecular Physics* **1970**, 19, 553.
- [42] Huang, J. Q., Du, P. Y., Weng, W. J. and Han, G. R. *Journal of Inorganic Materials* **2005**, 20, 1106.
- [43] Yang, S. J., Choi, J. Y., Chae, H. K., Cho, J. H., Nahm, K. S. and Park, C. R. *Chemistry of Materials* **2009**, 21, 1893.
- [44] Scherb, C., Schodel, A. and Bein, T. *Angewandte Chemie-International Edition* **2008**, 47, 5777.
- [45] Hermes, S., Schroder, F., Chelmoski, R., Woll, C. and Fischer, R. A. *J Am Chem Soc* **2005**, 127, 13744.
- [46] Schlappbach, L. and Zuttel, A. *Nature* **2001**, 414, 353.

9. OVERALL CONCLUSIONS AND ACCOMPLISHMENTS

9.1 Overall Conclusions

We have developed a method to enhance the hydrogen adsorption on sorbents through the application of electric field. The higher the electric potential, the higher the adsorption can be obtained within the experimental range of this investigation. This enhancement is due to the increase of the binding energy between hydrogen molecules and the sorbent under the electric field. This offers a potential solution for DOE on looking for a compromise between chemisorption and physisorption for hydrogen storage. Bonding of chemisorption is too strong and requires high temperature for the release of hydrogen. Bonding for the physisorption is too weak and requires very low temperature for sufficient uptake of hydrogen. Electric field potentials can enhance the physisorption and can be adjusted to yield reversibility required in a system at room temperature.

9.2 Patents

Jiann-Yang and Shangzhao Shi, "Increased Volumetric and Gravimetric Hydrogen Gas Storage Capacity", US Patent Application No. 12/657,213. Filed: 15 January, 2010.

9.3. Publications

- 2005 J.Y. Hwang and S. Shi, "Novel Perhydrides for Hydrogen Storage", in Materials for the Hydrogen Economy, edited by J.J. Petrovic et al, Materials Science and Technology 2005, pp. 43-47.
- 2006 X. Sun, J.Y. Hwang, S. Shi, B. Li, and X. Huang, "Temperature Measurement in Microwave Heating", EPD Congress 2006, edited by S.M. Howard et al, TMS Publications, pp. 1123-1132.
- 2006 J.Y. Hwang, S. Shi, B. Li and X. Sun, "Storing Hydrogen with Perhydride", Advanced Materials for Energy Conversion III, edited by D.S. Chandra, TMS Publications, pp. 101-107.
- 2006 X. Sun, J.Y. Hwang, S. Shi, and X. Huang, "Homogeneous Heating in Microwave Processing", ADVANCED PROCESSING OF METALS AND MATERIALS, VOLUME 5 - NEW, IMPROVED AND EXISTING TECHNOLOGIES: IRON AND STEEL and RECYCLING AND WASTE TREATMENT, Edited by F. Kongoli and R.G. Reddy, TMS, pp. 171-180.

- 2006 S. Shi, R.H. Scheicher, R. Pandey, and J.Y. Hwang, "Clustering of H₂ Molecules Around Alkaline Earth Metal Ions; A Systematic Density Functional Theory Study", International Symposium on Metal-Hydrogen Systems (MH2006), October 1-6, Maui, Hawaii.
- 2006 S. Shi, J.Y. Hwang, X. Sun, and B. Li, "Potentials of Metal Oxide Molecules for Binding Hydrogen into Clusters", Fuel Cells and Energy Storage Systems: Materials, Processing, Manufacturing and Power Management Technologies Symposium, MS&T 2006, Oct. 15-19, Cincinnati, OH.
- 2007 S. Shi and J.Y. Hwang, "Research Frontiers on New Materials and Concepts for Hydrogen Storage" International Journal of Hydrogen Storage, v.32, issue 2, pp.224-228.
- 2007 Z. Xu, H. Wang, and J.Y. Hwang, "Complex Carbon Nanotube Superstructures Synthesized with Natural Mineral Catalysts", CARBON, v. 45, issue 4, pp. 873-879.
- 2008 Z. Xu, J.Y. Hwang, B. Li, X. Huang and H. Wang, "The Characterization of Various ZnO Nanostructures using Field Emission SEM", JOM, v.60, no. 4, pp. 29-32.
- 2010 X. Li, J.Y. Hwang, S. Shi, X. Sun, and Z. Zhang, "Effects of Electric Potential on Hydrogen Adsorption", CARBON, Volume 48, Issue 3, pp. 876-880.
- 2010 S. Shi, J.Y. Hwang, X. Li, X. Sun, and B.I. Lee, "Enhanced Hydrogen Sorption on Carbonaceous Sorbents under Electric Field", International Journal of Hydrogen Energy, Volume 35, Issue 2, pp. 629-631.
- 2010 Jiann-Yang Hwang, Shangzhao Shi, Xiang Sun, Stephen Hackney, Xuan Li, "Hydrogen Storage Using Electric Field Enhanced Adsorption", Proceedings: Materials in Clean Power Systems V: Clean Coal-, Hydrogen Based-Technologies, Fuel Cells, and Materials for Energy Storage, Volume 2, TMS Publications, pp.413-420.
- 2010 X. Li, J.Y. Hwang, S. Shi, X. Sun, and Z. Zhang, "Effect of Piezoelectric Material on Hydrogen Adsorption", Fuel Processing Technology, Volume 91, Issue 9, pp.1087-1089..
- 2010 X. Sun, J.Y. Hwang, S. Shi, "Hydrogen Storage in Mesoporous Metal Oxides with Catalyst and External Electric Field", J. Physical Chemistry C, 114 (15), pp.7178-7184.
- 2011 J.Y. Hwang, S. Shi, X. Sun, "Electric charge and hydrogen storage", International Journal of Energy Research, accepted. ID: ER-10-1696.